
Velocity Selection of Fast Laser Ablated Metal Atoms by a Novel Nonmechanical Technique: Temporally and Spatially Specific Photoionization (TASSPI)

Mario E. Fajardo

**AFRL/PRS
10 East Saturn Blvd.
Edwards AFB CA 93524-7680**

February 1998

Final Report

19980601 049

Approved for Public Release; Distribution is Unlimited



**AIR FORCE RESEARCH LABORATORY
AIR FORCE MATERIEL COMMAND
EDWARDS AIR FORCE BASE CA 93524-7048**

DTIC QUALITY INSPECTED 1

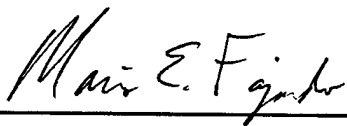
NOTICE

When U.S. Government drawings, specifications, or other data are used for any purpose other than a definitely related Government procurement operation, the fact that the Government may have formulated, furnished, or in any way supplied the said drawings, specifications, or other data, is not to be regarded by implication or otherwise, or in any way licensing the holder or any other person or corporation, or conveying any rights or permission to manufacture, use or sell any patented invention that may be related thereto.

FOREWORD

This special technical report was prepared under contract JON: 2303M2C8, for the Air Force Research Laboratory, Propulsion Directorate, Edwards AFB CA 93524-7001. The Project Manager was Dr. Mario Fajardo.

The report has been reviewed and is approved for release and distribution in accordance with the distribution statement on the cover and on the SF Form 298.



MARIO E. FAJARDO
Project Manager



PHILIP A. KESSEL
Technical Advisor
Propulsion Sciences and Advanced
Concepts Division



RANNEY G. ADAMS, III
Public Affairs Director

REPORT DOCUMENTATION PAGE			Form Approved OMB No 0704-0188	
Public reporting burden for this collection of information is estimated to average 1 hour per response, including the time for reviewing instructions searching existing data sources gathering and maintaining the data needed, and completing and reviewing the collection of information. Send comments regarding this burden estimate or any other aspect of this collection of information, including suggestions for reducing this burden to Washington Headquarters Services, Directorate for Information Operations and Reports, 1215 Jefferson Davis Highway, Suite 1204, Arlington, VA 22202-4302, and to the Office of Management and Budget, Paperwork Reduction Project (0740-0188), Washington DC 20503.				
1. AGENCY USE ONLY (LEAVE BLANK)		2. REPORT DATE February 1998		3. REPORT TYPE AND DATES COVERED Final Mar 92 to Mar 97
4. TITLE AND SUBTITLE Velocity Selection of Fast Laser Ablated Metal Atoms by a Novel Nonmechanical Technique: Temporally and Spatially Specific Photo-Ionization (TASSPI)			5. FUNDING NUMBERS C: PE: 62601F PR: 1R2N and 1R2R TA: RA51 RD52	
6. AUTHOR(S) Mario E. Fajardo				
7. PERFORMING ORGANIZATION NAME(S) AND ADDRESS(ES) Air Force Research Laboratory (AFMC) Propulsion Directorate AFRL/PRS 10 E. Saturn Blvd. Edwards AFB CA 93524-7680			8. PERFORMING ORGANIZATION REPORT NUMBER PL-TR-97-3051	
9. SPONSORING/MONITORING AGENCY NAME(S) AND ADDRESS(ES)			10. SPONSORING/MONITORING AGENCY REPORT NUMBER	
11. SUPPLEMENTARY NOTES				
12a. DISTRIBUTION/AVAILABILITY STATEMENT Approved for Public Release; Distribution is Unlimited			12b. DISTRIBUTION CODE A	
13. ABSTRACT (MAXIMUM 200 WORDS) This report documents the in-house research effort that led to the development of a novel, nonmechanical technique for performing velocity selection of fast laser ablated atoms. The technique is named "TASSPI" for Temporally and Spatially Specific Photo-Ionization as ablated metal atoms moving either too slowly or too quickly to be hidden behind an opaque mask are photoionized by a second pulsed laser and then deflected from the main atomic beam by a magnetic field. This report includes previously unpublished and supplementary materials which candidly summarize the present status of this technology. The four peer-reviewed publications and the US Patent that have resulted from this effort are included herein as appendices.				
14. SUBJECT TERMS laser ablation; velocity selection; aluminum; gallium; indium; photoionization			15. NUMBER OF PAGES 72	
			16. PRICE CODE .	
17. SECURITY CLASSIFICATION OF REPORT Unclassified	18. SECURITY CLASSIFICATION OF THIS PAGE Unclassified	19. SECURITY CLASSIFICATION OF ABSTRACT Unclassified	20. LIMITATION OF ABSTRACT SAR	

TABLE OF CONTENTS

<u>Section</u>	<u>Page</u>
GLOSSARY	vii
1.0 INTRODUCTION	1
2.0 TASSPI OVERVIEW	3
3.0 EXPERIMENTAL DETAILS	5
3.1 Apparatus	5
3.2 Ablation Target Preparation	8
3.3 Ablation Laser Intensity	9
4.0 STATUS AND UNRESOLVED ISSUES	11
4.1 Fundamental Assumption of Time-of-Flight	11
4.2 Efficient Photoionization of Neutrals	14
4.2.1 Single photon ionization	14
4.2.2 Multi-photon ionization	16
4.3 Magnetic Deflection of Ions	19
4.4 Purity of Atomic Beam	23
4.4.1 Metal molecules and clusters	23
4.4.2 Metal particles	24
4.4.3 Metastable excited species	27
4.5 Maximum Achievable Beam Fluxes	32
4.6 Matrix Depositions Using TASSPI Geometry	33
5.0 CONCLUSIONS AND RECOMMENDATIONS	35
ACKNOWLEDGMENTS	36
REFERENCES	37
APPENDIX A	42
M. Macler and M.E. Fajardo, Mater. Res. Soc. Proc. 285 , 105 (1993) "Determination of atomic velocity distributions using transient absorption measurements."	
APPENDIX B	48
M. Macler and M.E. Fajardo, Appl. Phys. Lett. 65 , 159 (1994) "Comparison of short range and asymptotic measurements of the kinetic energy distributions of laser ablated aluminum atoms."	

TABLE OF CONTENTS (continued)

<u>Section</u>	<u>Page</u>
APPENDIX C	51
M. Macler and M.E. Fajardo, Appl. Phys. Lett. 65 , 2275 (1994) “Velocity Selection of fast laser ablated aluminum atoms by temporally and spatially specific photoionization.”	
APPENDIX D	54
M.E. Fajardo and M. Macler, Mater. Res. Soc. Proc. 388 , 39 (1995) “Velocity selection of laser ablated metal atoms by a novel non-mechanical technique.”	
APPENDIX E	60
M.E. Fajardo and M. Macler, US Patent #5,567,935 (22 October 1996) “Velocity selected laser ablation metal atoms source.”	

LIST OF FIGURES

<u>Figure</u>	<u>Caption</u>	<u>Page</u>
1	Atomic velocities vs. kinetic energies	2
2	TASSPI concept schematic diagram	3
3	Experimental vs. calculated Al atom TASSPI KE resolutions	4
4	Mechanical drawings of velocity selected source (VSS) module	5
5	TASSPI elements in VSS module	6
6	Ion-deflection magnet assemblies	6
7	EEA/TOFMS vacuum chamber	7
8	SEM image of ablated groove in aluminum, viewed at 45° to surface normal	9
9	Temporal dependence of XeCl ablation laser pulse	10
10	Ablated aluminum flux vs. 308 nm laser intensity	10
11	Numerical simulations of time-of-flight experiments: vary τ	12
12	Numerical simulations of time-of-flight experiments: vary d	12
13	Optical transient absorption time-of-flight data for Li and Na atoms	13
14	ArF excimer laser and Al atom photoionization lineshapes	14
15	Photoionization cross-sections of Ga and In atoms at 193 nm	15
16	KrF laser output and B atom absorptions	17
17	Two-photon photoionization of B atoms with KrF laser	17
18	Two-photon photoionization of B atoms with tunable dye laser	18
19	Magnetic rejection of fast laser ablated Mg^+ ions	19
20	Photograph of Al^+ emissions from 7 mm gap magnetic field region	20
21	Magnetic field measurements	21
22	Effect of magnetic fields on Cu film depositions	22
23	Detection of non-Al atom Al^+ ion precursors	23
24	Detection of non-In atom In^+ ion precursors	24
25	SEM image of aluminum film deposited on a glass slide	25
26	QCM measurement showing deposition of aluminum particles	25
27	Close-up of ablated groove shown in Figure 8	26
28	Closer view of ablated aluminum target surface	26
29	Time-integrated emission spectra of laser ablated aluminum plume	28
30	Relative number densities of Al^+ , Al^+ , and Al^{++} species	28
31	Electronic temperature of laser ablated aluminum plume	29
32	Decay of electron density with distance from ablated surface	30
33	Time-resolved emissions from laser ablated aluminum plume	31
34	Directionality of laser ablated aluminum plume	32
35	Matrix deposition experimental schematic	33
36	Li/Ar matrices	34
37	Al/Ar matrices	34

LIST OF TABLES

<u>Table</u>	<u>Title</u>	<u>Page</u>
1	Atomic single photo ionization data	16
2	Parameters for electron temperature calculation	29

GLOSSARY

2PI	2-photon PhotoIonization
Al, B, C, Cu, Ga, In, Li, Na, Mg, Si	Atoms of the elements: aluminum, boron, carbon, copper, gallium, indium, lithium, sodium, magnesium, silicon.
Cl, F	Halogens: chlorine, fluorine.
EEA	Electrostatic Energy Analyzer.
FWHM	Full Width at Half Maximum.
H ₂ , D ₂	Molecular hydrogen, deuterium.
HEDM	High Energy Density Matter.
I _{abl}	Ablation Laser Intensity.
I _{sp}	Specific Impulse.
KE	Kinetic Energy.
KED	Kinetic Energy Distribution.
LTE	Local Thermodynamic Equilibrium.
MPI	Multiphoton PhotoIonization
Ne, Ar, Kr, Xe	Rare gases: neon, argon, krypton, xenon.
PI	PhotoIonization.
QCM	Quartz Crystal Microbalance.
REMPI	Resonance Enhanced Multiphoton PhotoIonization.
SEM	Scanning Electron Microscope.
TASSPI	Temporally And Spatially Specific PhotoIonization.
TOF	Time Of Flight.
TOFMS	Time Of Flight Mass Spectrometer.
UV	UltraViolet.
VS	Velocity Selection.
VSS	Velocity Selected Source.

1.0 INTRODUCTION

This project grew out of our efforts to produce cryogenic solid hydrogen samples doped with laser ablated metal atoms for evaluation as advanced chemical propellants within the US Air Force High Energy Density Matter (HEDM) program¹. Such fuels are predicted theoretically² to provide up to 20% improvements in specific impulse³, I_{sp} , over the state-of-the-art liquid oxygen/liquid hydrogen system. Because the propellant typically makes up such a large fraction of the mass of a fully loaded space launch vehicle (*e.g.*, $\approx 85\%$ for both the Titan IV and Space Shuttle)⁴ such an increase in I_{sp} can translate into dramatic systems level performance improvements.

Our preliminary matrix isolation experiments⁵⁻⁷, in which laser ablated metal atoms are codeposited with a matrix host gas (*e.g.*, H_2 , D_2 , Ne, Ar, Kr, Xe) onto a cryogenically cooled substrate, suggested that the incident kinetic energy (KE) of the metal atoms plays a key role in determining the atomic isolation efficiency of the sample deposition process, and in the formation of novel metal atom trapping site structures (see Section 4.6 for an updated interpretation of these experiments). We initially proposed⁵, and subsequently refined^{6,7}, a microscopic model of the matrix deposition process which attributes these effects to penetration into previously deposited matrix layers by the fast metal atoms⁸⁻¹² generated in the laser ablation process. Definitive testing of this hypothesis required a source of metal atoms with a narrow spread of KEs tunable throughout roughly the 1 to 20 eV range.

A survey of the available technology¹³ failed to turn up a suitable candidate for a fast metal atom source to be incorporated into our matrix isolation experiments. We required/desired a source that would be: (a) directional, so we could aim the metal atom flux onto our deposition substrate; (b) intense, a flux of at least 10^{12} atoms/cm²-s at the deposition substrate would keep sample preparation times below an hour; (c) pure, as all of the species in the source beam may become incorporated into the sample; (d) monoenergetic, the narrower the spread of KEs, the less ambiguous the results; (e) tunable, over at least the 1 to 10 eV range, preferably 1 to 20 eV; (f) compact, characteristic dimensions of order 10 cm would keep the system a tabletop affair.

We were aware that laser ablation of metal targets in a vacuum provides intense pulses of fast metal atoms with broad kinetic energy distributions (KEDs) covering the desired KE range⁸⁻¹². Thus, one approach would be to perform velocity selection (VS) on the laser ablated metal atoms, allowing only those atoms with KEs within a narrow desired range to proceed to the deposition substrate. Mechanical VS of a continuous molecular beam is typically accomplished¹³⁻¹⁸ by directing the beam through a series of rapidly rotating slotted disks mounted on a common shaft. The disks and slots are arranged so only those species with a narrow range of velocities can pass unscathed through all the openings. Despite rotational speeds in excess of 50,000 rpm, compact mechanical velocity selectors (*i.e.*, path lengths $L \approx 10$ cm) cannot transmit species with velocities much higher than 5×10^5 cm/s (although higher velocities can be achieved at the expense of longer path lengths^{17,18}, transmitted atomic flux levels fall rapidly as $1/L^2$). The pulsed nature of the laser ablation source allows a simplification of the mechanical VS approach to a single rotating slotted disk or "chopper" with the same

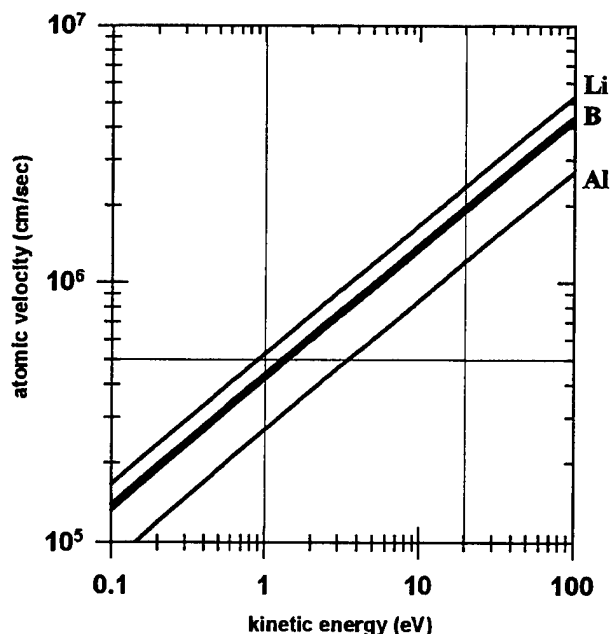


Figure 1. Atomic velocities vs. kinetic energies.

Calculated velocities are shown for ^7Li , ^{10}B , ^{11}B , and ^{27}Al isotopes. Vertical lines are shown demarking the 1 to 20 eV kinetic energy range. The horizontal line is drawn at 5×10^6 cm/s.

mechanically imposed limitations. Since the velocities of interest in our experiments exceeded this limit (e.g., a 10 eV Al atom travels at 8.5×10^5 cm/s, see also Figure 1) we decided not to pursue a mechanical VS approach.

The remainder of this manuscript documents the novel, non-mechanical approach we took to achieving VS of fast laser ablated metal atoms. The most relevant technical results have already appeared in peer-reviewed publications¹⁹⁻²², and in the US Patent for this invention that was assigned to the US Air Force²³; References 19 through 23 are included herein as Appendices A through E, respectively. In the main text, we will review the basic ideas behind our approach, and will include previously unpublished results and supplementary materials that should give the reader a clearer impression of the overall progress achieved during this project.

We will attempt to document candidly the present status of this technology. We will point out both its strengths and limitations, as an aid to anyone interested in adopting and extending our work, in the hope that this approach will survive and flourish beyond its original confines. We will conclude with a brief description of how this project has impacted our efforts to create metal atom doped cryogenic solid propellants, and how it may someday impact the production of other novel thin-film materials.

2.0 TASSPI OVERVIEW

We named our novel nonmechanical method of velocity selection "TASSPI," an acronym for "Temporally And Spatially Specific PhotoIonization" since metal atoms that are not at the right place at the right time are photoionized and rejected from the main atomic beam. Figure 2 is a schematic of the final, successful TASSPI configuration.

Briefly: a PLUME containing fast metal atoms is generated by focusing a pulse from a high-power ABLATION LASER onto a rotating metal TARGET held within a high vacuum chamber. After a delay of order 1 μ s, a second pulse from a VELOCITY SELECTION LASER is used to photoionize nearly all of the metal atoms which are traveling either too quickly or too slowly to be hidden behind a narrow opaque MASK. These photoions (and any nascent ions from the ablation event) are deflected by a MAGNETIC FIELD and so do not continue through the APERTURE as part of the velocity selected ATOMIC BEAM.

The transmitted velocity selected atoms have a mean velocity:

$$v \approx \frac{t_{vs}}{x} \quad (1)$$

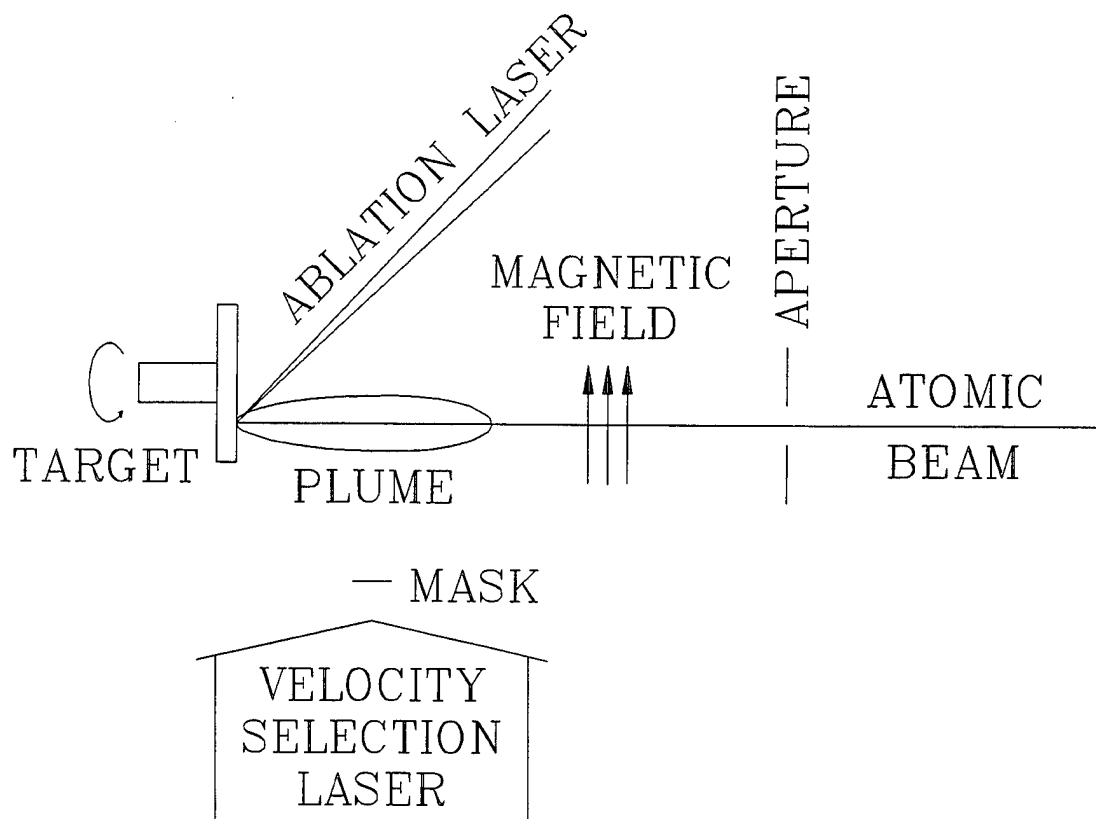


Figure 2. TASSPI concept schematic diagram.

in which: t_{VS} is the delay between ablation and velocity selection lasers, and x is the distance from the surface of the ablation target to the center of the opaque mask. The resulting atomic beam is not perfectly monoenergetic. The spread of velocities, Δv (full width at half maximum) and the corresponding spread of kinetic energies, ΔKE , are related by:

$$\frac{\Delta KE}{KE} \approx 2 \frac{\Delta v}{v} \approx 2 \left[\left(\frac{\Delta x}{x} \right)^2 + \left(\frac{\Delta t_{VS}}{t_{VS}} \right)^2 \right]^{\frac{1}{2}} \quad (2)$$

in which: KE is the mean kinetic energy, Δx is the width of the opaque mask, and Δt_{VS} is taken as the sum of the duration of the velocity selection laser pulse and the jitter between the ablation and velocity selection pulses ($\Delta t_{VS} \approx 50$ ns).

Examples of successful VS of Al, Ga, and In atoms by TASSPI, along with the actual experimental conditions used, can be found in Appendices C & D (Refs. 21, 22). The bottom line is that the TASSPI technique works remarkably well for the Al, Ga, and In systems, and our observations are well explained by the simple one-dimensional model embodied by Equations (1) and (2). Figure 3 shows the correlation between experimental and calculated kinetic energy resolutions, $\Delta KE/KE$, from a series of TASSPI VS experiments on Al atoms.

This brief description of the TASSPI approach has relied on a number of simplifying assumptions which require either verification or qualification. Section 4 is dedicated specifically to these issues, and to questions concerning the general applicability of the approach. But first, Section 3 contains details of the construction and operation of the TASSPI experimental apparatus, details that were glossed over in our previous publications and which are germane to the subsequent discussions.

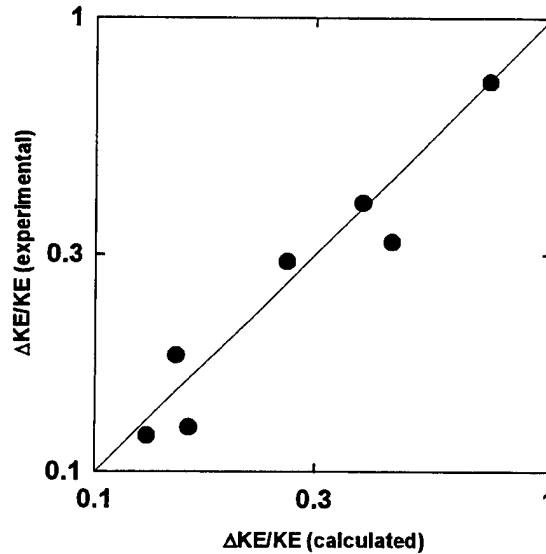


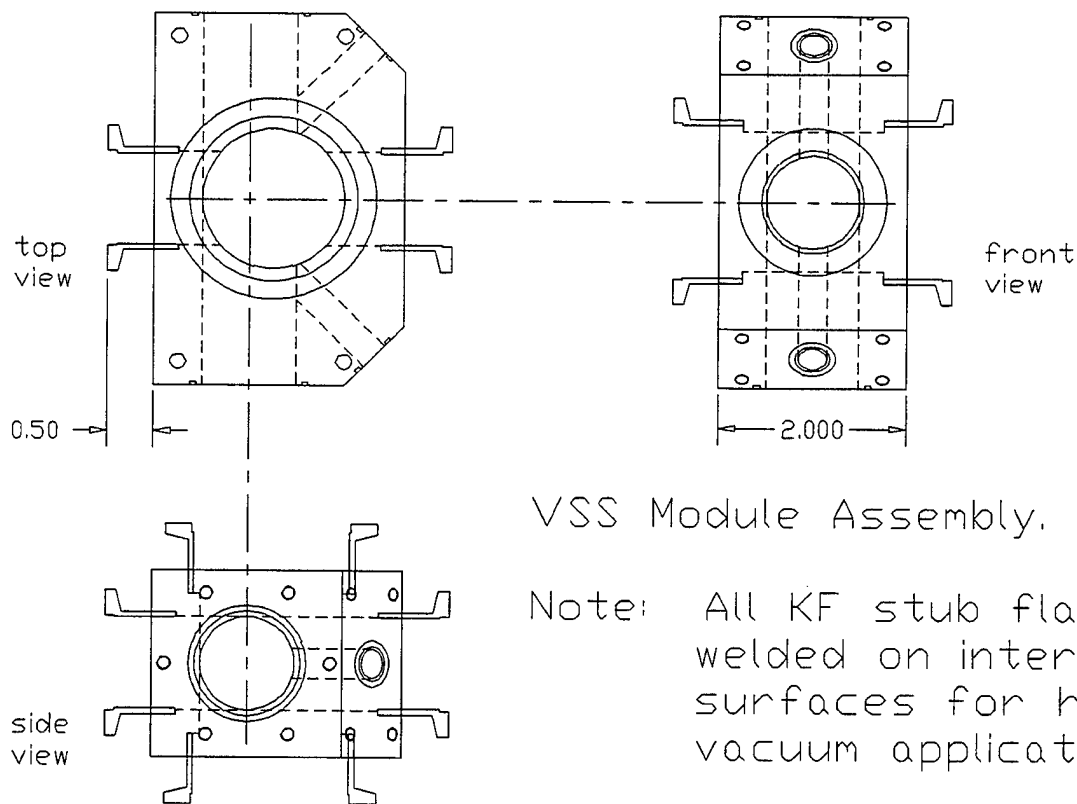
Figure 3. Experimental vs. calculated Al atom TASSPI KE resolutions.

3.0 EXPERIMENTAL DETAILS

3.1 Apparatus²⁴

Schematic diagrams of the various experimental setups used throughout this study can be found as "Fig. 1" in each of Appendices A to D. Familiarization with the generic experimental descriptions in those appendices is recommended prior to consideration of the mechanical details presented in this section.

Figure 4 shows scale drawings of the velocity selected source (VSS) module, which was constructed of stainless steel at one of the Jet Propulsion Laboratory machine shops. Figure 5 shows the various elements of the TASSPI scheme arranged within the VSS module. The 1/2 inch diameter ablation target is mounted on the shaft of a motorized rotational motion feedthrough (MDC #670021-04) which is attached to the rear KF25 port of the VSS module via a flexible metal bellows (NorCal #2FC-NW-25-1). The bellows allows the target to be moved off-center by a vertical translation stage (Newport #416) so that the ablation laser spot can cut tracks of different radii on the rotating target face.



VSS Module Assembly.

Note: All KF stub flanges welded on internal surfaces for high-vacuum application.

MEF 5/91.

Figure 4. Mechanical drawings of velocity selected source (VSS) module.

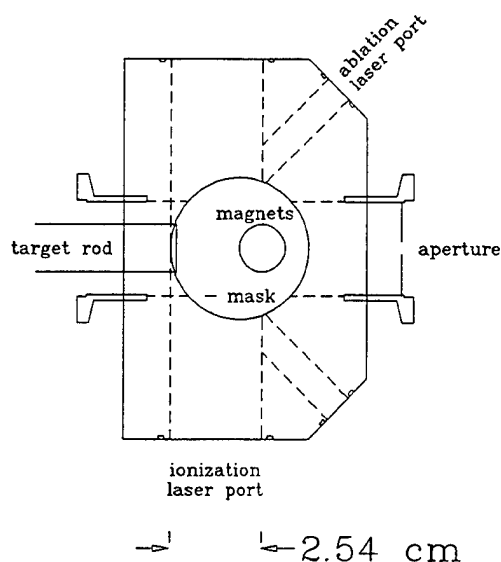


Figure 5. TASSPI elements in VSS module.

The ablation laser (Lambda-Physik, EMG202MSC, XeCl) is focused to a fixed point through one of the 5/16 inch clear diameter 45° window ports; the velocity selection laser is incident on the ablated plume through one of the 1 inch clear diameter side window ports. A small turbomolecular pump (Leybold Turbovac 50) is mounted upside down directly onto the top KF40 port. The pair of rare-earth/cobalt magnets which provide the ion-deflecting field are separated by a Delrin spacer drilled with a transverse hole; this assembly is mounted on an aluminum post glued to a KF40 blank-off flange which attaches at the bottom KF40 port. The beam defining aperture is incorporated into the o-ring centering ring for the front KF25 port.

Figure 6 shows various arrangements of the ion-deflection magnets (rare-earth/cobalt types) used throughout the course of this study. The leftmost setup employed 1/2 inch diameter magnets spaced by 5 mm providing a 2.8 kG deflection field, and was used during the experiments reported in Refs. 20 to 23 (Appendices B to E). More recently we've used 1 inch

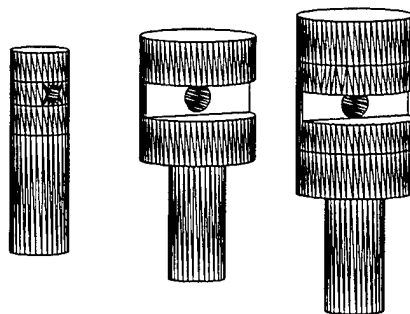


Figure 6. Ion-deflection magnet assemblies.

diameter magnets at various spacings which are more effective at deflecting the fastest ions. The transverse slot in the Delrin spacer shown in the center and right setups in Figure 6 allow access of the velocity selection laser beam over the entire 1 inch wide velocity selection region.

The main virtue of this experimental arrangement is its compact size; the distance from the ablation target surface to the front KF25 flange is less than 7 cm. In practice, it has a couple of annoying deficiencies which should be corrected in future designs. (1) Because the flexible bellows in the ablation target mounting system generates considerable variable stresses when the vacuum system is pumped down or vented back to atmosphere, optical alignment, laser spot size measurements, etc. can only be performed while under vacuum. (2) All the laser windows located only 5 to 6 cm from the ablation target become coated with ablated material, limiting the duration of an experiment. Some self-cleaning of the ablation laser window takes place if a long focal length lens is used, but only at the risk of burning the window. We have recently obtained modest relief from these effects by adopting the opposite strategy of mounting these windows on extension flanges and using shorter focal length lenses.

Figure 7 shows a perspective view of the vacuum chamber containing the Comstock electrostatic energy analyzer/time of flight mass spectrometer (EEA/TOFMS) system used to characterize the KEDs of the ablated species. The EEA is of 160° spherical sector design^{25,26}, which is claimed to optimize the ion transmission at a given energy resolution²⁵, but which requires a particularly inconvenient mounting and alignment scheme. The elaborate support stand, constructed of 1/2 inch aluminum plate at the JPL shops, was designed to support the vacuum chamber so that the input axis of the EEA is parallel to the top of the optical table at a height of 10 inches. The second rotation (around the EEA input axis) relieves a conflict between the 1 meter TOF tube and the vertically mounted liquid helium cryostat used in matrix isolation experiments. In hindsight, the minor performance loss of a 90° sector EEA would probably be easily outweighed by its mechanical mounting advantages.

Performing KED measurements on velocity selected atoms requires the synchronized

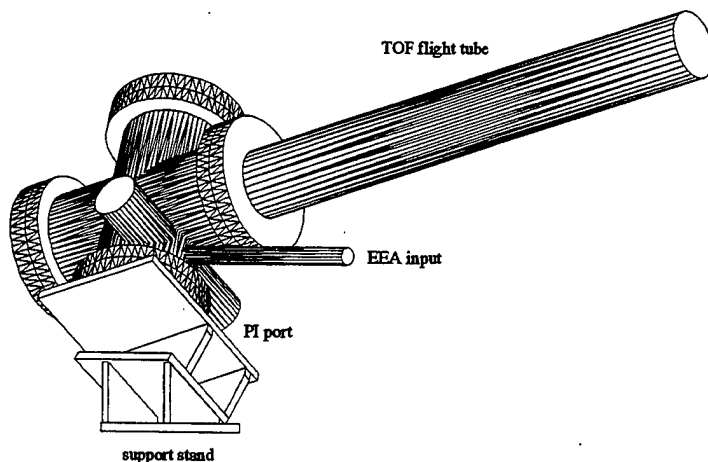


Figure 7. EEA/TOFMS vacuum chamber.

use of three pulsed lasers for: ablation, velocity selection, and PI detection of the atoms. The final PI detection laser is focused at the entrance of the EEA through a quartz window labeled "PI port" in Figure 7. Photoions of the proper KE transit the curved EEA and are then accelerated down the 1 meter TOF tube and detected by a microchannel plate. This detection scheme introduces a useful "redundancy" in that the velocity of the metal atoms (determined by the time delay between the VS and PI lasers) must match the KE setting of the EEA for metal photoions to be detected. Observation of a metal ion signal at inappropriate delays between the VS and PI lasers indicates the presence of polyatomic metal photoion precursors and is a sensitive measure of the purity of the atomic beam (see Section 4.4).

3.2 Ablation Target Preparation

Our ablation targets are typically 1/2 inch diameter by 1 to 3 mm thick disks of a pure material. Alkali metal target disks are cast in an inert gas environment, glued with a minimum amount of quick setting epoxy onto the target rod, attached to the motorized rotational motion feedthrough assembly, then transferred as quickly as possible to the VSS module. With care and practice, exposure of these targets to the atmosphere can be kept below ≈ 30 seconds. Despite these precautions, and the forgivingly low humidity of the desert air at the Phillips Lab, the resulting fresh target surface is usually badly oxidized (and nitrified in the case of lithium). Additional continuous surface oxidation also occurs due to the $\sim 10^{-7}$ Torr water vapor background in our vacuum chamber.

Boron targets are made from polycrystalline chunks of elemental boron, ground to shape using a diamond dust impregnated wheel. This process leaves a rough ablation surface, with several $\sim 1 \text{ mm}^3$ pits, which results in a very erratic ablation plume. We have also experienced contamination of the boron surface with metallic iron transferred from the borrowed diamond wheel. We have not experimented with melt casting our own boron targets because of materials compatibility issues in handling liquid boron. Aluminum targets are easily cut from high purity 2 mm thick foil pieces, and once mounted can be faced-off on a lathe with a very sharp cutting tool leaving a macroscopically smooth, trued ablation surface. Gallium targets are prepared following the alkali metal procedure mentioned above, but must be kept cool (below 30°C) to avoid remelting. Indium targets are again easily cut from foil stock.

We tolerate these crude initial ablation surface preparation procedures because of the even worse abuse inflicted by the ablation laser itself over the course of an experiment. A typical experiment begins by using the ablation laser to "clean" a circular track on the initially prepared surface. After a few thousand laser pulses, a shallow groove begins to form. Data are acquired using the subsequent 10^4 to 10^5 ablation pulses during which the ablation plume is relatively stable and quantities such as ablation laser intensity threshold for visible plasma formation are reproducible. Figure 8 shows a scanning electron microscope (SEM) image of a 0.8 mm wide, 6 mm diameter circular groove in an aluminum target after about 5×10^4 incident ablation pulses. Despite the tortured morphology of this surface, the flux of ablated aluminum as measured by a quartz crystal microbalance (QCM) remains suitably constant over tens of thousands of laser pulses.

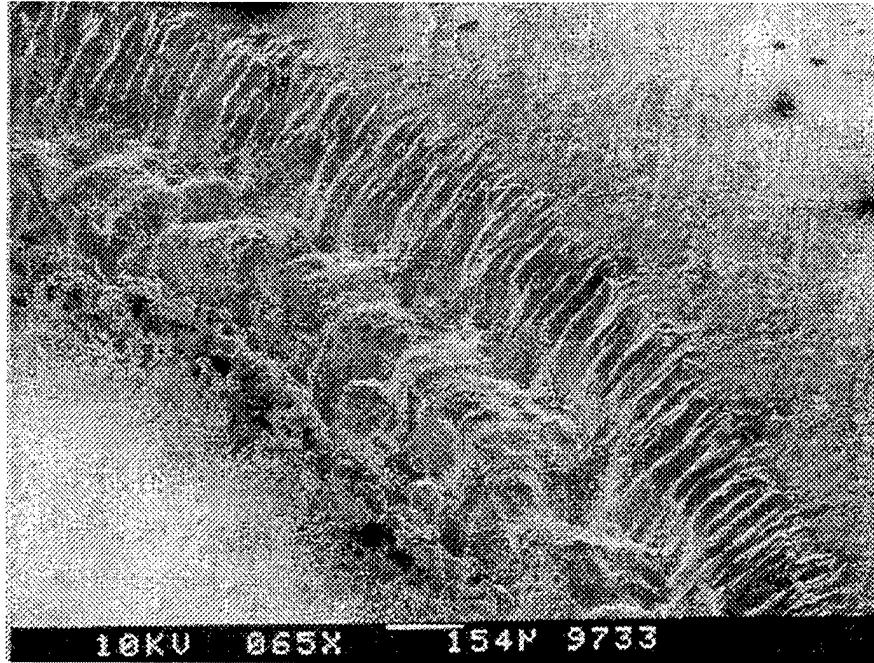


Figure 8. SEM image of ablated groove in aluminum, viewed at 45° to surface normal. Ablation laser wavelength 308 nm, 17 mJ/pulse, 5 Hz repetition rate, 2.5 hour exposure; focused to an oval spot 0.3 x 0.7 mm, $I_{abl} \sim 1 \times 10^8 \text{ W/cm}^2$.

Because of the vertical orientation of the ablation target surface in these experiments, we have not experimented with ablation of a pool of liquid gallium at say, 40° C, which would provide a self-healing ablation surface with negligible background Ga vapor pressure.

3.3 Ablation Laser Intensity

Throughout this study, we have concentrated primarily on ablation with pulses from a XeCl excimer laser. Thus, we have not explored any of the effects of varying the ablation laser wavelength ($\lambda = 308 \text{ nm}$) or pulse duration ($\tau \approx 30 \text{ ns}$). We *have* varied both the laser pulse energy (E), and the ablation spot area (A), and find that several important plume characteristics (appearance of a visible plume, atomic KEDs, ion content of ablated plume, formation of metal clusters and particulates, etc.) are correlated with the ablation laser intensity (I_{abl}) calculated as:

$$I_{abl} (\text{W/cm}^2) \approx \frac{E(\text{J})}{\tau(\text{s}) \cdot A(\text{cm}^2)} \quad (3).$$

Simplifying assumptions inherent in this formula are: (1) the time dependence of the laser pulse is a square wave of duration τ , Figure 9 shows the actual temporal shape recorded with a 2 ns rise-time photodiode; (2) the photon flux is constant over the focused spot area A then falls suddenly to zero outside, in fact the flux is most intense at the center of the beam and the edges of the spot are not well defined.

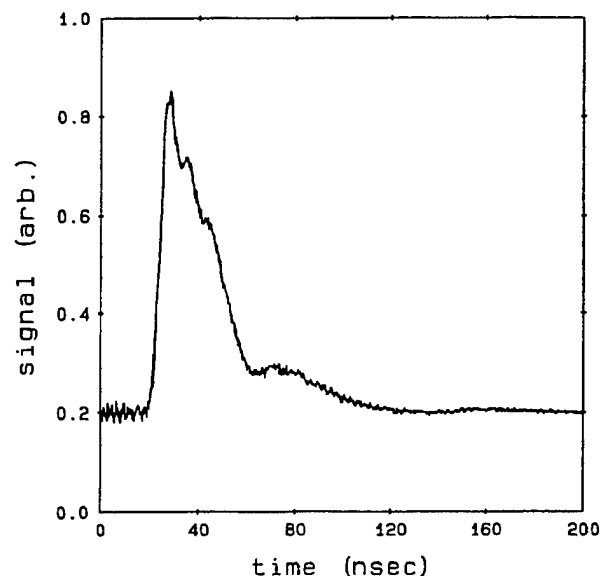


Figure 9. Temporal dependence of XeCl ablation laser pulse.

We measure the ablation spot area from the burn pattern on a small piece of photographic paper in contact with the ablation target surface. These spots have visibly sharp edges corresponding to some arbitrary and undetermined ablation laser intensity threshold level. Spot dimensions measured in this manner are typically a little larger than those estimated from SEM micrographs of ablated craters in aluminum foil. Thus, the photographic paper method is

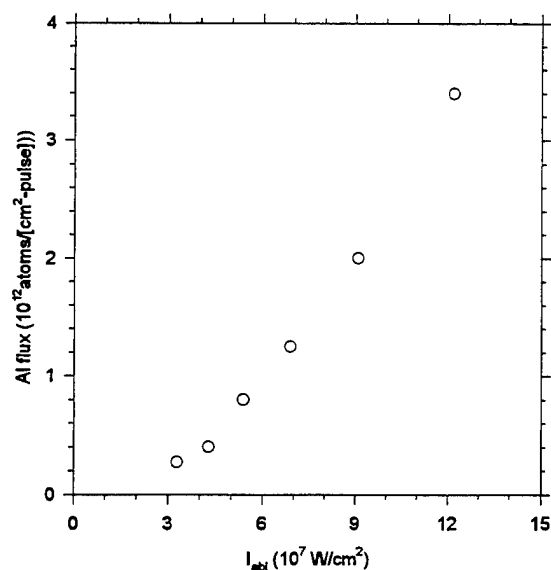


Figure 10. Ablated aluminum flux vs. 308 nm laser intensity.
Ablation spot area = 0.003 cm^2 , distance from target to QCM = 8 cm.

certainly *not* a unique determination of the area, but the measurement is easy to make and is reproducible ($\pm 20\%$ error in A). Despite all these problems, we have found these estimated ablation laser intensities to be very useful for predicting various plume properties, and in the comparison of results from different experiments.

A couple of points for calibration. We estimate the threshold intensity of a 308 nm excimer ablation laser for formation of a visible plasma above a clean track in an aluminum target to be $I_{abl} = 2.5(\pm 1.0) \times 10^7 \text{ W/cm}^2$. This value is consistent with the QCM measurements of aluminum flux vs. 308 nm ablation laser intensity presented in Figure 10, which suggests a threshold in the $2 \times 10^7 \text{ W/cm}^2$ to $3 \times 10^7 \text{ W/cm}^2$ range.

4.0 STATUS AND UNRESOLVED ISSUES

As mentioned above in Section 2, many aspects of the TASSPI approach can be successfully described by a very simple model which rests on a number of simplifying assumptions. However, progress in extending the utility and applicability of TASSPI will likely require closer examination of the limits of validity of those assumptions. In this section we report our present status, and address a number of unresolved issues in the form of (at least partially) unanswered questions.

4.1 Fundamental Assumption of Time-Of-Flight

Question: Are all the ablated metal atoms produced in a sufficiently short period that the fundamental assumption of TOF holds (i.e., is there a one-to-one mapping of velocity with distance traveled from the ablated target surface)? In a basic TOF experiment, all species are supposed to leave the source region at effectively the same instant, so that the faster species will arrive at the detection region before the slower species. Equivalently, the faster species are assumed to travel a longer distance from the source region at any given time of flight. If, instead, species production occurs over an extended time period, then it is possible for faster species produced later in the process to overlap both spatially and temporally with slower species that have been traveling for a longer period of time. In this case, TOF profiles cannot be readily transformed to yield velocity distributions, and velocity selection schemes based on a single selection element (*e.g.*, chopper wheel, TASSPI) will fail.

To illuminate this point, we performed a series of Monte Carlo numerical simulations of idealized TOF experiments. The simulated atoms are produced with random speeds distributed as a Gaussian (for computational, not physical reasons), with average velocity = $1 \times 10^6 \text{ cm/s}$ and a spread of velocities (FWHM) of $1 \times 10^6 \text{ cm/s}$. Individual start times are randomly distributed uniformly over an initial production period of variable length τ . The distance to the detection region is taken as 1 cm, the width of the detection region is 0.01 cm. The detector is assumed to be velocity independent, with a time resolution of 20 ns. The TOF profiles are generated as histograms accumulated over 10^5 events; the equations for transforming from TOF to velocity and KE distributions are given in Appendix A. The results are shown in Figure 11, which demonstrates the gross distortions of the TOF and velocity distributions that occur if the duration of the atom production period is comparable to the mean TOF.

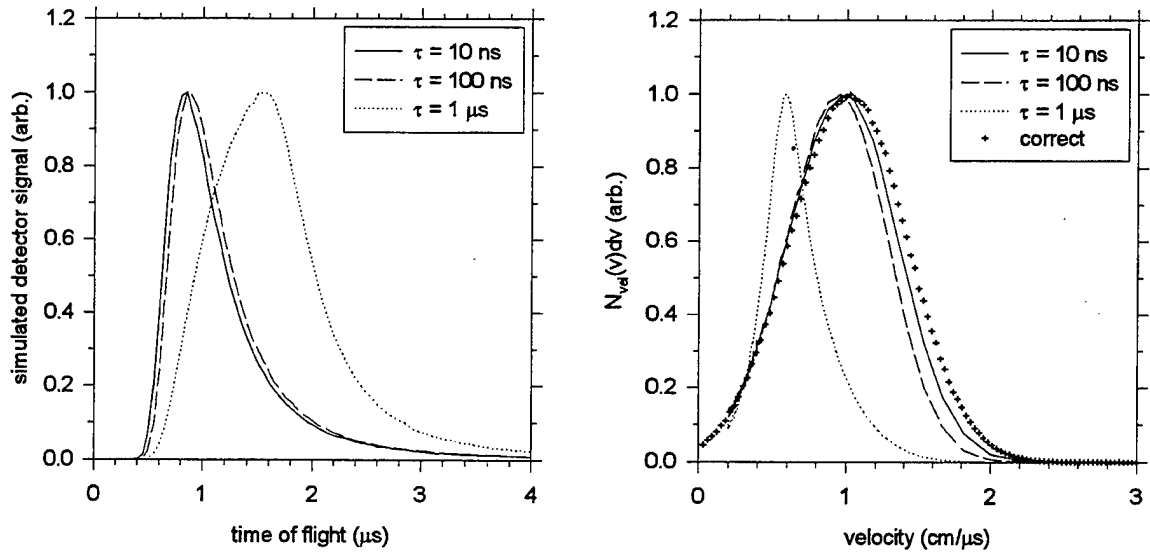


Figure 11. Numerical simulations of time-of-flight experiments: vary τ .
Distance from surface to detection region fixed at $d = 1.0$ cm.

We also performed several simulations of the TOF profiles expected for various separations, d , between the atom production and detection regions. Figure 12 shows the simulated TOF and velocity distributions obtained for $\tau = 100$ ns, as “measured” at $d = 0.5$, 1.0, and 2.0 cm. These results suggest that production period durations of ~ 100 ns could be deduced from velocity distributions obtained at various target-to-detector distances.

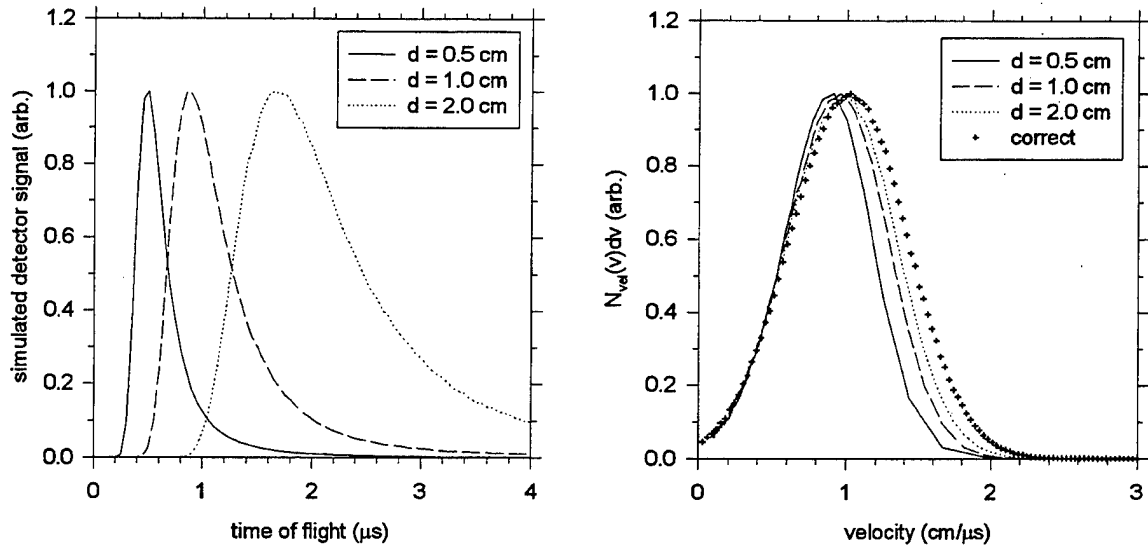


Figure 12. Numerical simulations of time-of-flight experiments: vary d .
Production period duration fixed at $\tau = 100$ ns.

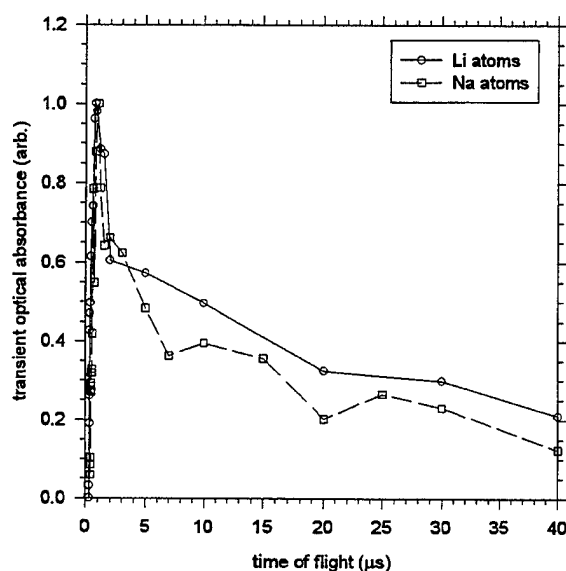


Figure 13. Optical transient absorption time of flight data for Li and Na atoms. Detection region is 1.0 cm from ablation target surface. $I_{abl} \approx 5 \times 10^7 \text{ W/cm}^2$ for Li data; $I_{abl} \approx 7 \times 10^7 \text{ W/cm}^2$ for Na data.

We checked experimentally for this possibility very early on in this project, by comparing velocity and KE distributions calculated from Al atom TOF data obtained at various distances from the ablation target surface^{19,20} (Appendices A & B). The good agreement among these data, and the lessons learned from our simulations, suggest an upper limit for the duration of the Al atom production period of $\approx 100 \text{ ns}$, under our ablation conditions. The fact that the TASSPI scheme works for Al, Ga, and In atoms is further demonstration that the duration of the atomic production period is comparable to the excimer laser pulse length, and thus at least an order of magnitude shorter than the typical $\sim 1 \mu\text{s}$ TOF.

The same cannot be said for ablation of lithium and sodium targets, where we always observe a very long time (up to \sim millisecond long) tail in the TOF data. Figure 13 shows some raw time-of-flight data from the same optical transient absorption (OTA) experiments reported in ref. 19. Previous laser ablation studies have also reported $\sim 100 \mu\text{s}$ tails in Na atom TOF data²⁷. We initially interpreted these tails as artifacts arising from our experimental geometry and a supposed difference in the divergence of the ablated plumes for the alkali vs. aluminum systems¹⁹. However, it is difficult to believe that such an effect could stretch out the TOFs into the millisecond regime. We now suspect that evaporation of slow (thermal) alkali atoms from the ablation spot itself, or from superheated ablated droplets^{28,29}, are more likely explanations. Conclusion: Ablation conditions must be found which avoid producing copious amounts of slow alkali atoms before the TASSPI method can be applied to these systems.

4.2 Efficient Photoionization of Neutrals

Question: Can the undesired ablated metal atoms to be rejected by the TASSPI scheme really be photoionized with high efficiency?

4.2.1 Single photon ionization

An important reason that TASSPI works so well for the Al, Ga, and In systems is the accidental coincidence of strong photoionizing absorptions³⁰⁻³² for these atoms with the intense 193 nm output of the ArF excimer laser. Figure 14 shows a comparison between the lineshape of our ArF laser (measured with a 0.85 m SPEX 1403 double grating monochromator, 1800 line/mm gratings, unintensified Si diode array detector) and an Al atom autoionization resonance. The dips on the ArF lineshape are due to Schumann-Runge absorptions of atmospheric O₂ over the ≈ 4 m unpurged path from the laser to the array detector³³ (we employ a dry N₂ purge of the ArF beam path in all other experiments). The 193.2 and 193.6 nm lines in the Al spectrum correspond to the spin-orbit split components of the $3s3p(^2S) \leftarrow 3s^23p(^2P^o)$ atomic transition; these absorptions are extremely strong, with published peak cross-sections of 1.2×10^{-16} and 1.7×10^{-16} cm², respectively³¹. These values compare well with our value of $\sigma_{PI}(\text{Al}, 193\text{nm}) = 1.8(\pm 0.4) \times 10^{-16}$ cm² derived from ArF laser Al atom photoionization saturation measurements²⁰.

We assume that the PI process can be represented by:

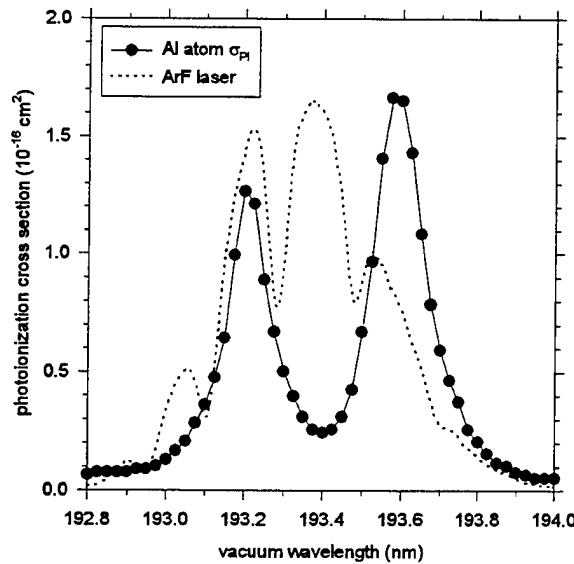


Figure 14. ArF excimer laser and Al atom photoionization lineshapes.
Al data from Ref. 30; the ArF lineshape is modified by transmission through ≈ 4 meters of air.

in which: M is a neutral metal atom, $h\nu_{PI}$ is the PI photon, M^+ is the photoion, and e^- is the ejected electron. The fraction of surviving neutral metal atoms following a photoionization laser pulse is then given by:

$$\frac{[M]}{[M]_0} = \exp[-\sigma_{PI} \Phi_{PI}] \quad (5)$$

in which Φ_{PI} is the total flux ($\#/cm^2$) of laser photons. The fractional yield of metal photoions is correspondingly:

$$\frac{[M^+]}{[M]_0} = 1 - \exp[-\sigma_{PI} \Phi_{PI}] \quad (6)$$

The ArF 193.3 nm wavelength corresponds to a photon energy of 1.03×10^{-18} J; thus a laser fluence of $F_{PI} = 1 \text{ mJ/cm}^2$ corresponds to a 193 nm photon flux of $\Phi_{PI} = 1.0 \times 10^{15} \text{ cm}^{-2}$. Therefore, achieving 99% rejection of Al atoms requires a readily available ArF laser fluence of only $\approx 30 \text{ mJ/cm}^2$.

For Ga and In, the corresponding autoionization resonances are very short lived ($\tau \approx 10^{-15} \text{ s}$) and are embedded in the photoionization continuum just beyond the ionization limit, resulting in broad ($\Delta\lambda \approx 30 \text{ nm}$) absorptions overlapping the 193 nm ArF emission³². Thus, the peak photoionization cross sections are about an order of magnitude smaller than for Al. Figure 15 shows the saturation behavior of the Ga^+ and In^+ ($KE = 2 \text{ eV}$) metal ion signals as a function of increasing photoionization laser fluence; the σ_{PI} 's are calculated by fitting these data to the functional form of Eqn[6], and agree well with the literature values^{30,32} of $\sigma_{PI}(Ga, 193\text{nm}) = 2.8 \times 10^{-17} \text{ cm}^2$, and $\sigma_{PI}(In, 193\text{nm}) = 2.2 \times 10^{-17} \text{ cm}^2$. Thus, rejection of Ga or

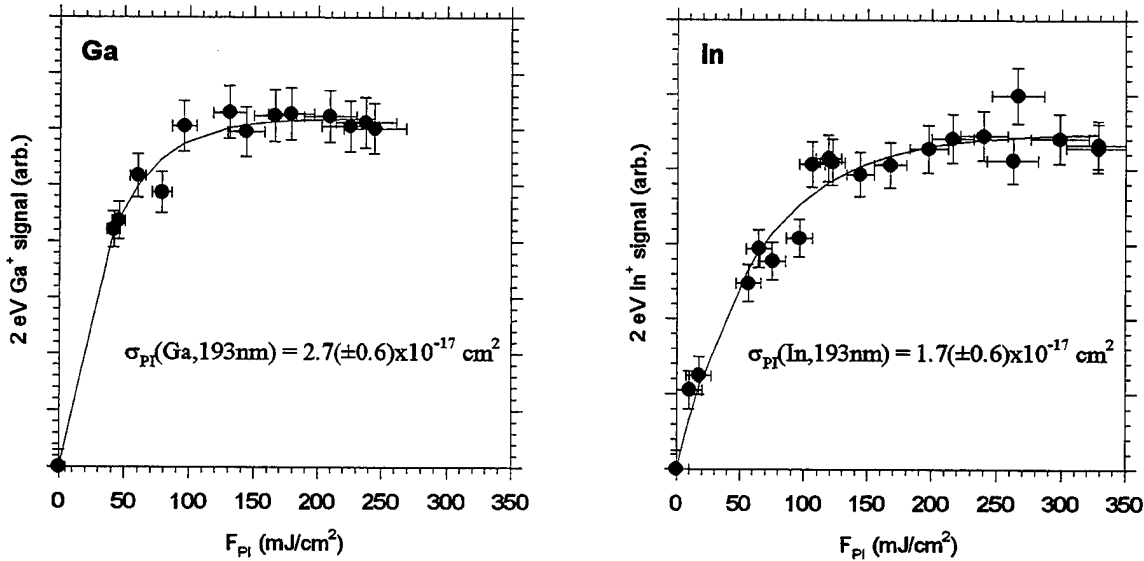


Figure 15. Photoionization cross-sections of Ga and In atoms at 193 nm.
For both experiments: ablation wavelength = 308 nm, $I_{abl} = 3.4 \times 10^7 \text{ W/cm}^2$.

Table I. Atomic single photon ionization data.*Ionization potentials (I.P.) from Ref. 34, σ_{PI} data from Ref. 30.*

<u>Atom</u>	<u>I.P.(eV)</u>	<u>$\lambda_{thr}(\text{nm})$</u>	<u>$\sigma_{PI}(\text{cm}^2)$</u>	<u>comments</u>
Li	5.392	229.9	$1.5\text{-}2.0 \times 10^{-18}$	140-230 nm range
B	8.298	149.9		
C	11.260	110.1		
Na	5.139	241.3	$< 1.5 \times 10^{-19}$	140-240 nm range
Mg	7.646	162.1	$< 1.2 \times 10^{-18}$	140-162 nm range
Al	5.986	207.1	1.0×10^{-16}	peak @ 206 nm
Si	8.151	152.1	$3.6\text{-}3.8 \times 10^{-17}$	140-152 nm range

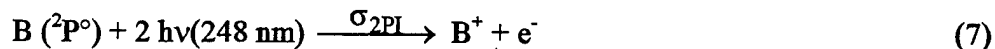
In atoms at the 99% level requires photoionization fluences of $\approx 300 \text{ mJ/cm}^2$, which are achievable, but entail focusing conditions that may damage some optical window materials.

Unfortunately, as shown in Table I, the prospects for single photon TASSPI of other atoms of HEDM interest (*e.g.*, Li, B, C, Na, Mg, Si) are not promising, because the photoionization cross sections are too small, and/or the ionization threshold wavelengths, λ_{thr} , are too short for presently available lasers. Conclusion: the utility of a single photon ionization TASSPI scheme is limited to systems exhibiting a fortunate coincidence between strong atomic photoionization absorptions and radiation from high powered pulsed lasers. Technological progress in the form of new commercially available vacuum ultraviolet lasers may extend the utility of the TASSPI scheme to other systems.

4.2.2 Multi-photon ionization

In order to overcome the limitations of the single photon PI approach described above, we turned to Multi-Photon Ionization (MPI) schemes, in which two or more photons are absorbed (simultaneously or sequentially) in the ionization process. Matching one or more photon energies to atomic transition energies greatly increases the probability of ionization, leading to the phenomenon of Resonance Enhanced Multi-Photon Ionization (REMPI)³⁵⁻³⁸. Our experiments along these lines have been limited to a few attempts at MPI of laser ablated boron atoms. The results of these preliminary experiments are ambiguous, and are presented here mainly to document our status and describe the issues to be clarified.

Figure 16 shows the positions of the B atom $2s2p^2(^2S) \leftarrow 2s^22p(^2P^o)$ transitions at 40040 and 40025 cm^{-1} and the output of our KrF excimer laser which has a main peak near 40220 cm^{-1} and a weaker satellite peak³⁹ near 40140 cm^{-1} . We hoped that this "near coincidence" might enhance the two-photon photoionization (2PI) yield of the process:



in which σ_{2PI} is a two-photon photoionization cross section with units of $\text{cm}^4\text{-s}$.

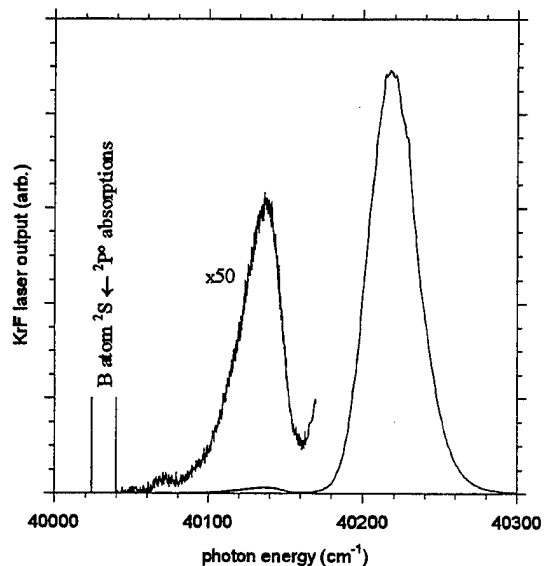


Figure 16. KrF laser output and B atom absorptions.

Figure 17 shows the results of two attempts to saturate the B^+ ion signal in a 2PI experiment; the 4 eV and 10 eV data are scaled to the same asymptote. We fit these data to the simplest kinetic model consistent with Eqn[7]:

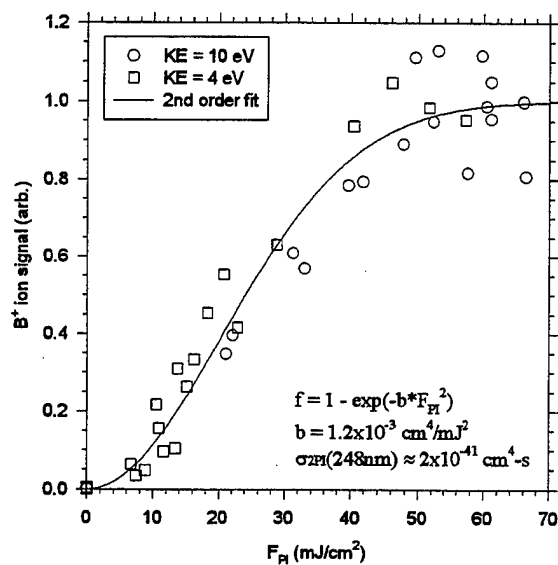


Figure 17. Two photon photoionization of B atoms with KrF laser.
 308 nm ablation laser intensity = $7.5 \times 10^7 \text{ W/cm}^2$. See text for discussion of confidence limits on the extracted 2PI cross-section.

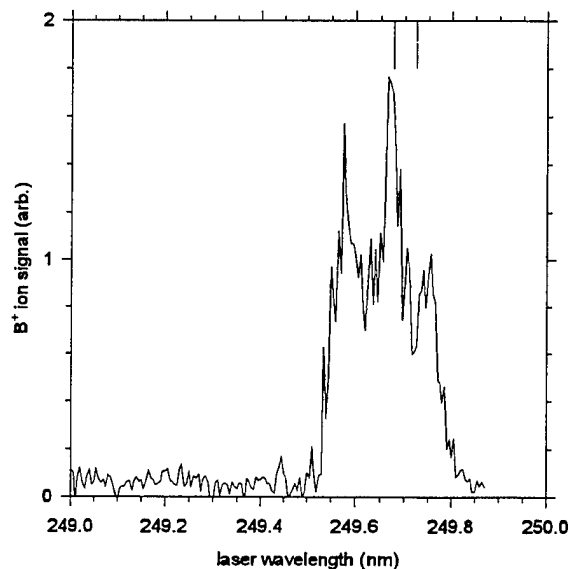


Figure 18. Two photon photoionization of B atoms with tunable dye laser. *The positions of the B atom absorptions are shown at the top of the figure. Ablation laser wavelength = 248 nm; $F_{PI} \approx 2 \text{ J/cm}^2$, $I_{PI} \approx 10^8 \text{ W/cm}^2$.*

$$\frac{[B^+]}{[B]_0} = 1 - \exp[-\sigma_{2PI} I_{PI}^2 \Delta t] \quad (8)$$

in which I_{PI} is the PI laser photon intensity ($\#/cm^2 \cdot s$), and Δt is the laser pulse duration (22 ns). While the quality of the fit would indicate an uncertainty in σ_{2PI} of about a factor of two, we have had difficulty in reproducing these results, and suggest that a more appropriate error estimate is one or two orders of magnitude. We have still to determine if the saturation behavior shown in Figure 17 is real or an artifact of our detection scheme; we also are concerned about the spectral stability of the KrF laser output (*i.e.* intensities of main vs. satellite peaks), and about the possibility of having burnt the quartz PI laser input windows.

Figure 18 shows the results of our single experiment using the UV frequency doubled output of a tunable dye laser which demonstrates true REMPI of laser ablated B atoms. Unfortunately, the total delivered energy in each UV laser pulse was only $\sim 1 \text{ mJ}$, too low by at least a factor of 10 for a TASSPI velocity selection experiment. This approach deserves further consideration if higher tunable UV laser pulse energies become available.

Finally, we point out here that TASSPI via REMPI techniques is likely not conveniently applicable to fast molecular species, unless they can be produced in only a few rovibronic states, all of which can be photoionized by the same laser.

Conclusion: the possible roles of MPI schemes in velocity selection by TASSPI remains largely unexplored.

4.3 Magnetic Deflection of Ions

Question: Can a static magnetic field really be used to deflect all the unwanted photoions without affecting the flux of neutrals? The original TASSPI scheme (c. 1990) called for the use of a static transverse *electric* field, \vec{E} , to deflect the unwanted ions via the Coulomb force⁴⁰:

$$\vec{F}_{\text{Coul}} = q \vec{E} \quad (\text{cgs units}) \quad (9)$$

in which q is the charge on an ion. However, in our experiments, weak electrostatic fields did not have a significant effect on the flux of ions (as measured using a Faraday cup), and fields in excess of ≈ 0.3 statvolt/cm (~ 10 kV/m, SI units) resulted in arcing and activation of the high voltage power supply's circuit breaker.

Discussions between Dr Michel Macler and Dr Franklin Mead (OLAC PL/RKFE) in 1993 lead to the ultimately successful idea of using a static transverse *magnetic* field, \vec{B} , for ion rejection via the Lorentz force⁴⁰:

$$\vec{F}_{\text{Lor}} = \frac{q}{c} (\vec{v} \times \vec{B}) = q \vec{E}_{\text{eff}} \quad (10)$$

in which: \vec{v} is the ion velocity, and c is the speed of light. For typical values of: $\vec{v} = |\vec{v}| \hat{x}$, $\vec{B} = |\vec{B}| \hat{z}$, $|\vec{v}| = 10^6$ cm/s, $|\vec{B}| = 3$ kG, and $|q| = e$ (electron charge), the resulting Lorentz force, $\vec{F}_{\text{Lor}} = |\vec{F}_{\text{Lor}}| \hat{y}$, has a magnitude of $|\vec{F}_{\text{Lor}}| = 4.8 \times 10^{-11}$ dyne, and is equivalent to an

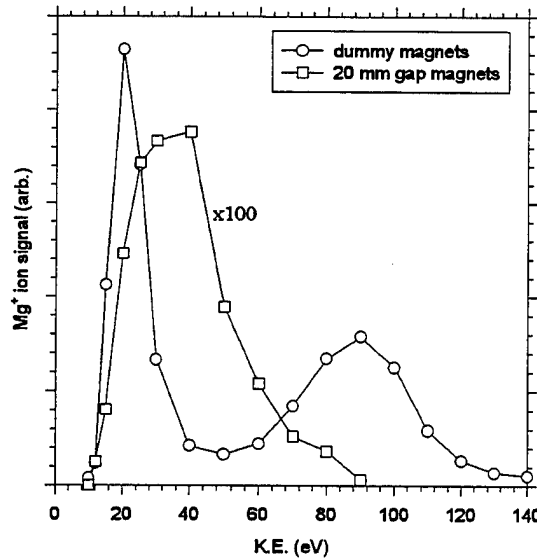


Figure 19. Magnetic rejection of fast laser ablated Mg^+ ions.

The KED obtained through the 20 mm gap magnets has been scaled by a factor of $\times 100$ for ease of presentation. The ablation laser wavelength = 308 nm, $I_{\text{abl}} \approx 4 \times 10^7$ W/cm².

effective electric field of magnitude $|\vec{E}_{\text{eff}}| = 0.1$ statvolt/cm (3300 V/m). A force of 4.8×10^{-11} dyne implies a transverse acceleration on an Al^+ ion of $a_y = 1.1 \times 10^{12}$ cm/s². Integrating this acceleration along a 1 cm interaction distance ($\Delta t \approx 10^{-6}$ s) yields an estimated deflection of $\Delta y = \frac{1}{2} a_y \Delta t^2 = 0.6$ cm which is sufficient to deflect the ion out of a beam of Al atoms in our TASSPI experiments.

The data in Figure 19 demonstrate the effectiveness of this method at rejecting nascent laser ablated Mg^+ ions. Even using the relatively weak field provided by the 20 mm gap magnet assembly (*vide infra*), rejection is good to the 99+% level for Mg^+ ion KE's below ≈ 25 eV. We do not understand why the shape of the KED for the transmitted Mg^+ ions is so different from that for the nascent ions, perhaps long-range interactions with electrons or ions trapped in the magnetic field region are somehow responsible.

The simple estimate of ion deflection presented above is strictly appropriate only in the limit that the resulting deflection (Δy) is small compared to the length of the interaction region, which is not the case. In fact, the radius of gyration⁴¹:

$$r_{\text{gyr}} = \frac{c p_{\perp}}{e B} \quad (11)$$

of an Al^+ ion with $|v| = 10^6$ cm/s ($p_{\perp} = 4.5 \times 10^{-17}$ g-cm/s) in a 3 kG magnetic field is only 0.9 cm, raising the possibility that some of the slower Al^+ ions (as well as electrons for which $r_{\text{gyr}} \sim 10^{-5}$ cm) may become temporarily trapped⁴² in the magnetic field region. Figure 20 shows how the spatial pattern of emissions from excited Al^* atoms appears to map out the regions of highest magnetic field intensity. No such patterns were observed when the magnets were

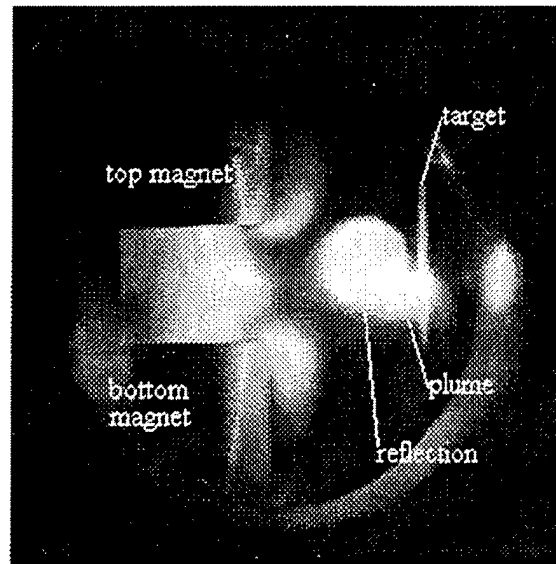


Figure 20. Photograph of Al^* emissions from 7 mm gap magnetic field region. The ablation laser wavelength = 308 nm, spot size ≈ 0.05 cm², $I_{\text{abl}} \approx 7 \times 10^7$ W/cm².

replaced by an aluminum metal replica. We speculate that the high field regions contain the largest concentrations of trapped electrons, which produce Al^* atoms either by recombination with Al^+ ions, or by collisions with fast Al atoms.

This view of our magnetic field raises the possibility that inhomogeneities in the field may affect the flux of neutrals via an inadvertent version of the Stern-Gerlach experiment^{43,44}. The force, F_z , on a magnetic dipole, $\vec{\mu}$, in an inhomogeneous magnetic field with nonzero field gradient $\partial B_z/\partial z$, is given by⁴³:

$$F_z = \mu_z \frac{\partial B_z}{\partial z} \quad (12)$$

in which μ_z is the component of $\vec{\mu}$ along the \hat{z} direction. Atomic magnetic dipole moments are of the same order of magnitude as the Bohr magneton:

$$\mu_B = \frac{e\hbar}{2m_e c} \approx 9.27 \times 10^{-21} \text{ erg/G} \quad (13)$$

in which: \hbar is Planck's constant divided by 2π , and m_e is the electron mass. Thus, a magnetic field gradient of $\sim 10 \text{ kG/cm}$ yields a force of $\sim 10^{-16}$ dyne, with resulting acceleration of an Al

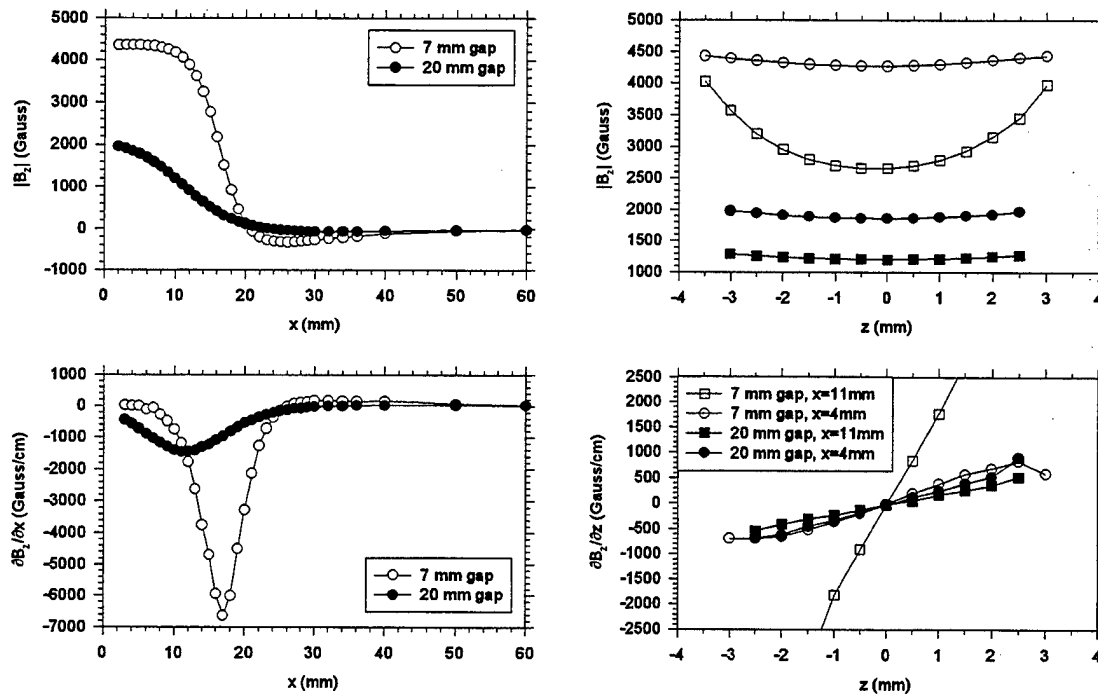


Figure 21. Magnetic field measurements.

The two left panels show $|B_z|$ and $\partial B_z/\partial x$ along the direction of the atomic beam, \hat{x} . The two right panels show $|B_z|$ and $\partial B_z/\partial z$ along vertical cuts perpendicular to the atomic beam, near the center of the magnets ($x=4\text{mm}$) and near the edge of the magnet assembly ($x=11\text{mm}$).

atom of $\sim 10^6$ cm/s², and a transverse displacement after 10^{-6} s of only $\sim 10^{-6}$ cm.

Despite these indications that the Stern-Gerlach effect should be completely negligible, we sought experimental verification that the magnetic deflection scheme was not affecting the neutral atomic flux. We were also concerned about other possible unanticipated effects, such as complex interactions with magnetically trapped charged species. We spent some time characterizing the magnetic deflection fields, and conducted various ablation experiments with different magnet configurations.

Our magnet arrangements are shown in Figure 6. Ignoring the Delrin spacer, they all have cylindrical symmetry about the \hat{z} axis (actually $D_{\infty h}$ point group symmetry). Figure 21 shows the main B_z field component and some of its derivatives for two different magnet configurations (middle and rightmost drawings in Figure 6). The largest gradients occur near the edges of the magnet assembly, with $\partial B_z/\partial z$ actually reaching the 2000 G/cm level for paths only 1 mm off of the \hat{x} axis centerline (see lower right panel of Figure 21). The large values of $\partial B_z/\partial x$ have no effect on fast neutral species traveling in the \hat{x} direction. Neither the B_x or B_y field components exceeded the 100 G level anywhere.

Figure 22 shows the lack of difference between the effects of the 7 mm and 20 mm gap magnet assemblies on the deposition rate of a copper film on a quartz crystal microbalance. A dummy magnet assembly constructed of aluminum metal was used to check the reproducibility of the no-field growth rate. The similarity between the deposition rates obtained with the two magnet assemblies indicates that the differences in field inhomogeneities are not important. The magnets *do* have a profound effect on the overall rate of deposition of the copper film, and it is

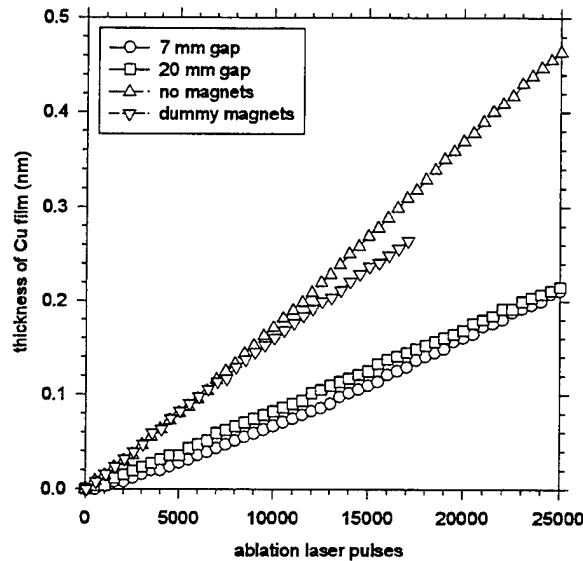


Figure 22. Effect of magnetic fields on Cu film depositions.

QCM to copper ablation target surface distance = 18 cm. Ablation laser wavelength = 308 nm, 75 mJ/pulse focused to 0.03 cm² area spot, $I_{abl} = 8 \times 10^7$ W/cm².

tempting to assign this difference to the "ion content" of the ablated Cu plume. However, other issues concerning the relative deposition efficiencies of ions vs. neutrals, and about the composition of ablated plumes, must be settled before this technique can be said to measure the ion/neutral content directly.

Conclusion: the strong, compact magnetic fields provided by state of the art permanent magnets are well suited to the rejection of ions from neutral beams.

4.4 Purity of Atomic Beam

Questions: What else is in the atomic beam following TASSPI besides velocity selected ground state metal atoms, and what can be done to minimize any impurities? Candidate species include: residual ions, residual very fast or very slow metal atoms, metal molecules and clusters, particulates, and metastable electronically excited metal atoms. We have discussed the issue of residual ions in the previous section. Likewise, we have discussed how very fast or very slow metal atoms may avoid photoionization in the velocity selection region, depending on the delay between the ablation and PI lasers²¹ (Appendix C). We also discussed above the problems with laser ablation of alkali metals apparently producing very slow metal atoms. We now discuss the other listed possibilities, in turn.

4.4.1 Metal molecules and clusters

We mentioned in Refs. 20-22 (Appendices B, C, and D) that a redundancy in our EEA-TOFMS with laser PI detection scheme allows us to detect certain other species besides metal atoms in our laser ablated beams. The redundancy is that the TOF for a neutral from the

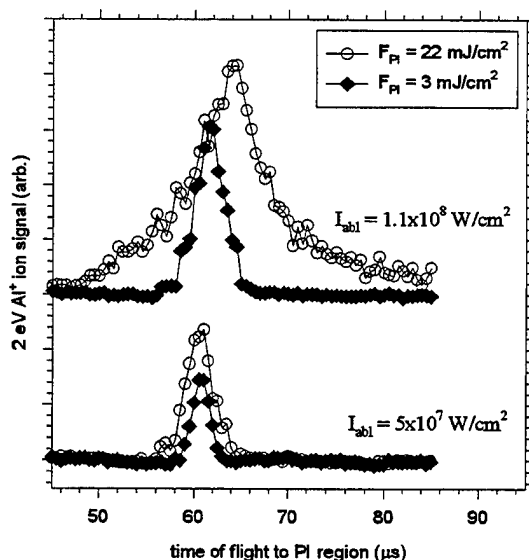


Figure 23. Detection of non-Al atom Al^+ ion precursors.
Ablation laser wavelength = 308 nm, PI laser wavelength = 193 nm.

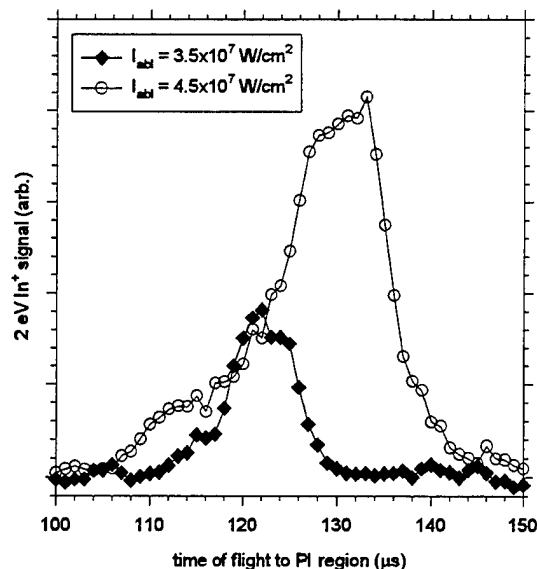


Figure 24. Detection of non-In atom In^+ ion precursors.

Ablation laser wavelength = 308 nm, PI laser wavelength = 193 nm, $F_{\text{PI}} = 270 \text{ mJ/cm}^2$.

ablation target surface to the PI region yields a velocity which must match the photoion pass KE set for the EEA; the TOFMS confirms the identities of the photoions by their arrival times at the MCP detector. Figure 23 shows the effect of ablation laser intensity on the production of non-Al atom Al^+ ion precursors. For $\lambda_{\text{abl}} = 308 \text{ nm}$ and $I_{\text{abl}} < 7 \times 10^7 \text{ W/cm}^2$ (lower panel) the delays between the ablation and PI lasers which yield $\text{KE} = 2 \text{ eV}$ Al^+ photoions correspond to the correct ablation-to-PI region TOF for $\text{KE} = 2 \text{ eV}$ Al atoms. At higher ablation laser intensities (upper panel), 2 eV Al^+ ions are observed for ablation/PI laser delays incommensurate with the photoionization of 2 eV Al atoms. Furthermore, under these conditions, the Al^+ ion yield is a strongly non-linear function of the PI laser fluence (Figure 2 in Appendix C shows an F_{PI}^4 dependence) suggesting photofragmentation and photoionization of metal clusters or particulates. Figure 24 shows similar data for 308 nm ablation of indium metal for which $I_{\text{abl}} > 4 \times 10^7 \text{ W/cm}^2$ yields abnormally broad ablation/PI TOF profiles.

We favor metal clusters and particles over other metal species (such as oxides or hydroxides) as the mistimed precursors for the metal photoions because these signals do not decrease in intensity once the ablation groove is present. [However, a similar effect *does* occur during the initial ablation “cleaning” of a freshly prepared target surface; in this case the mistimed precursors are likely metal oxides and hydroxides, as we observe nascent ions of such species in mass spectra recorded with fresh targets.] Additionally, the appearance of these robust abnormal TOFs is correlated with the presence of large numbers of 100 nm to 10 μm diameter metal particles on metal films deposited at higher ablation intensities.

4.4.2 Metal particles

Figure 25 shows an SEM image of spheroidal particles found on an aluminum film

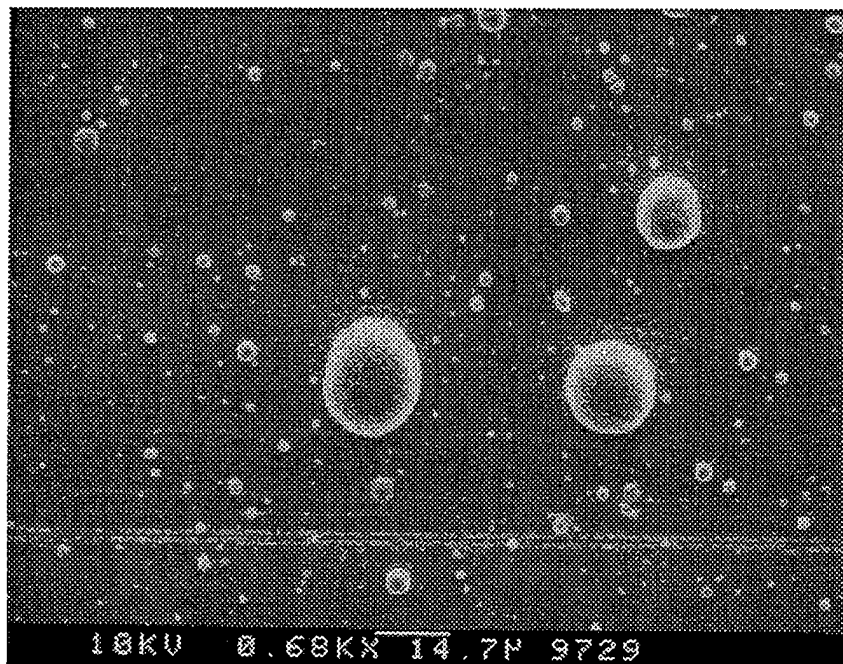


Figure 25. SEM image of aluminum film deposited on a glass slide.
Film deposited at 1 cm from Al target. $\lambda_{abl} = 308 \text{ nm}$, $I_{abl} \approx 1 \times 10^8 \text{ W/cm}^2$, 18000 pulses.

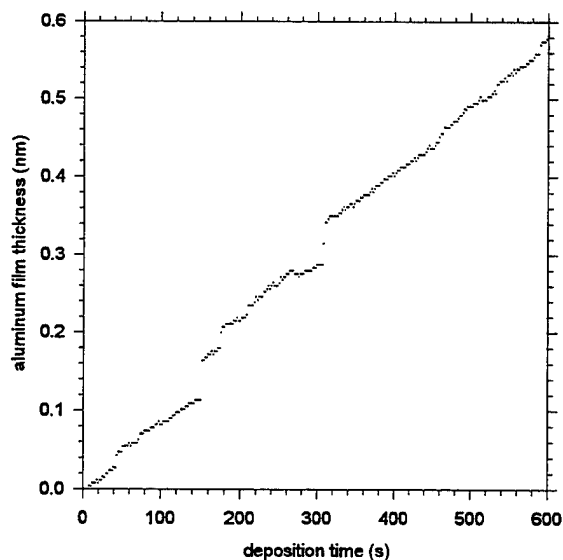


Figure 26. QCM measurement showing deposition of aluminum particles.
 *$\lambda_{abl} = 308 \text{ nm}$, 90 mJ/pulse focused to 0.03 cm^2 area spot, 10 Hz rep. rate, $I_{abl} \approx 9 \times 10^7 \text{ W/cm}^2$.
 Quartz crystal microbalance located 20 cm from ablation target surface.*

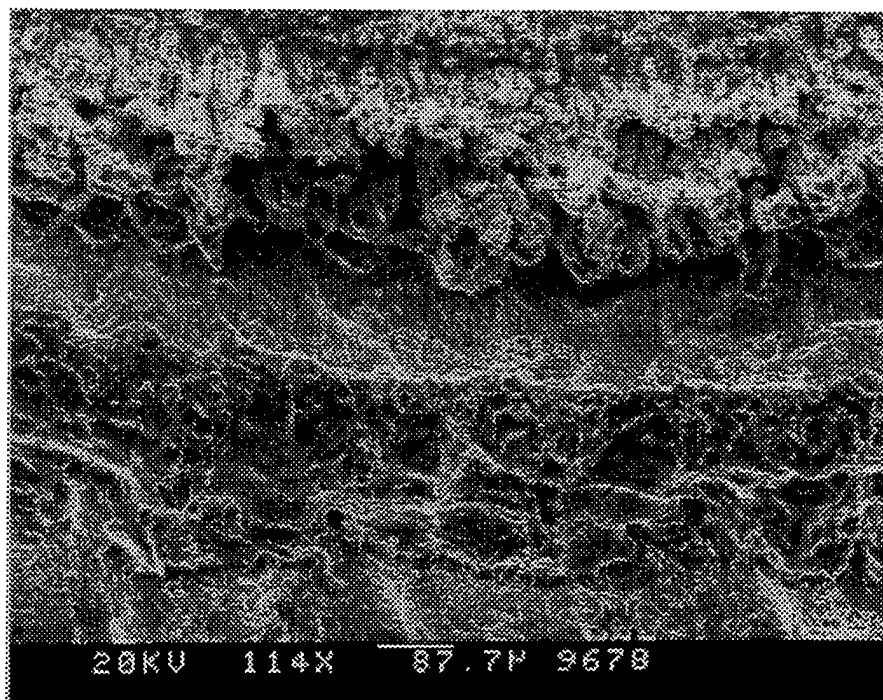


Figure 27. Close-up of ablated groove shown in Figure 8.

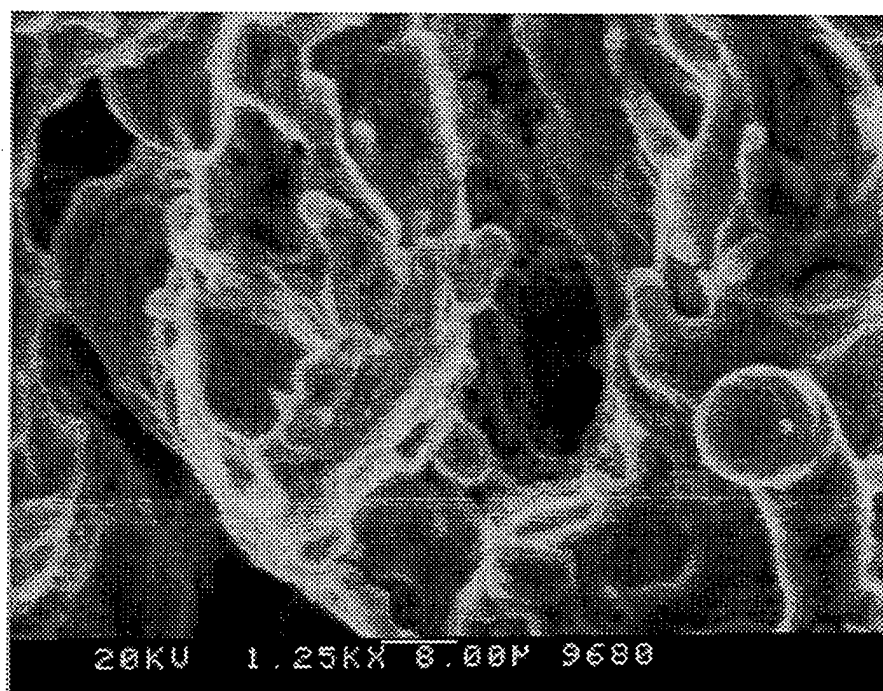


Figure 28. Closer view of ablated aluminum target surface.

deposited on a glass microscope slide located 1 cm from the ablation target surface. The ablation target surface history is similar to that of the target depicted in Figure 8, and is typical of metal ablation targets that have been exposed to tens of thousands of ablation pulses. The largest of the particles in Figure 25 have masses of ~ 1 ng, and Figure 26 shows that they can also be easily detected in QCM deposition experiments by the abrupt jumps they induce in the measured film thickness. Figures 27 and 28 are SEM images of the groove in the ablation target shown at increasing magnifications.

The origin and formation mechanism(s) of such particulates is still a topic of current research^{28,29,45-51}. However, our QCM observations suggest that the particles arrive suddenly and individually at the deposition surface, and our SEM images confirm the presence of likely particle precursor structures at the ablation target surface. Thus, our data support the contention that the particulates are transferred from the ablation target surface to the deposition surface directly, rather than forming by condensation in the gas phase or at the deposition surface. The rate of particle transfer is apparently strongly dependent on I_{abl} , and "threshold" intensities can be found below which the particles are not easily detected using our methods.

4.4.3 Metastable excited species

We have not performed any experiments to determine the extent to which metastable electronically excited species persist in our TASSPI beams. We present here our rationale for their probable importance, and for performing further studies along these lines.

The presence of electronically excited neutral and ionic species in laser ablated plumes is obvious from even the simplest analysis of plume emission spectra. Examples of such studies are too numerous to list exhaustively here, however we note that our approach, analysis, and results closely follow the pioneering work of Knudtson, *et al.* reported in Ref. [52]. Our data were collected in preparation for the transient absorption studies we reported in Refs. [19] and [20] (Appendices A & B).

Figure 29 shows the typical dependence of these emissions on distance from the ablation target surface. The peak at 396.4 nm is assigned to the Al atom $3s^23p(^2P^o) \leftarrow 3s^24s(^2S)$ transition, while the peaks at 358.6, 466.9, 560.9, and 625.0 nm are due to Al^+ ions, and those at 453.2 and 569.5 nm to Al^{++} ions⁵³ (see also Table II). Detailed analysis of such spectra can yield valuable information about conditions within the ablated plume. For instance, the observed integrated emission intensity from state i to state f , $I_{f \leftarrow i}$, is proportional to the number density of species in state i , N_i :

$$I_{f \leftarrow i} \propto N_i g_i A_{fi} \quad (14)$$

in which: A_{fi} is the transition probability between states i and f , and g_i is the degeneracy of state i . Figure 30 shows the results of such an analysis which reveals the rapid decay of emissions from charged species as the distance from the ablation target surface increases.

These spectra can also yield local plume properties such as the electronic temperature, T_e . Assuming local thermodynamic equilibrium (LTE), the relative intensities of the emission

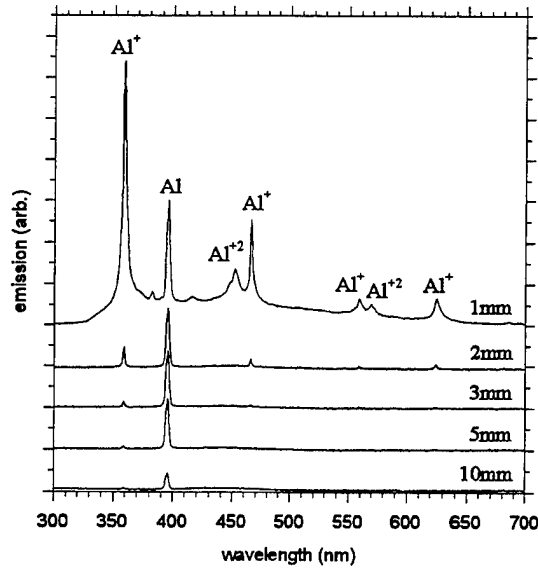


Figure 29. Time-integrated emission spectra of laser ablated aluminum plume.
Spectra recorded at various distances from the ablation target surface using a 10 μ s gate, $\lambda_{abl} = 308$ nm, $I_{abl} \approx 1 \times 10^8$ W/cm².

lines are related by⁵²:

$$\ln\left(\frac{I_{f \leftarrow i}}{g_i A_{fi}}\right) = \ln\left(\frac{N_0}{Z}\right) - \left(\frac{E_i}{k_B T_e}\right) \quad (15)$$

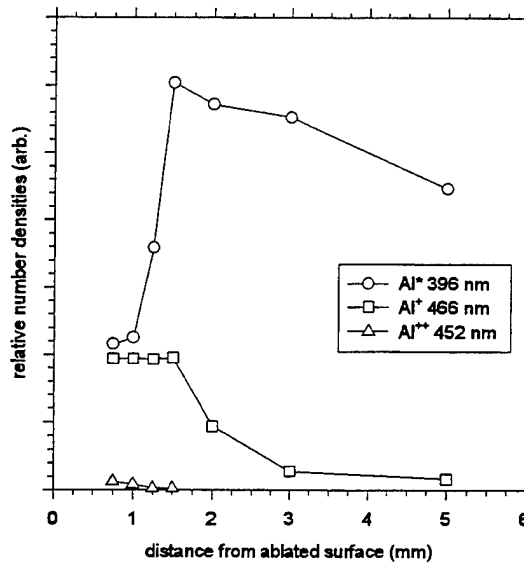


Figure 30. Relative number densities of Al*, Al⁺, and Al⁺⁺ species.
Integrated emission intensities from same experiment as shown in Figure 29.

Table II. Parameters for electron temperature calculation.

From Ref. 53, see text for definitions.

Transition	λ (nm)	E_i (cm ⁻¹)	g_i	A_{fi} (10 ⁸ s ⁻¹)	I_{fi-i} (arb.)
¹ D - ¹ P ^o	466.3	106921	3	0.53	0.659
¹ P ^o - ¹ D	559.3	133914	5	1.1	0.309
³ P ^o - ³ D	623.7	121481	15	1.10	1.768
³ P ^o - ³ S	683.0	120090	3	1.0	0.310
³ S - ³ P ^o	704.9	105453	9	0.58	1.609

in which: N_0 is the ground state population, Z is a partition function, E_i is the energy of state i , and k_B is Boltzmann's constant. A plot of the left hand side of Eqn[15] vs. E_i yields a straight line with slope $-1/k_B T_e$, so T_e can be determined without any knowledge of N_0 or Z . Figure 31 shows such a plot for emission data taken 1.25 mm from an ablated aluminum surface; the resulting T_e is ≈ 22000 K (1.8 eV); Table II includes the other parameters used in the calculation. Similar attempts to extract T_e for distances greater than ≈ 2 mm from the ablation surface give poor straight line plots, indicating that the assumption of LTE is failing as the plume expands and freezes in nonequilibrium excited state distributions.

The disparity between the characteristic electronic energy embodied in T_e , and the much larger KEs of the atomic and ionic species is striking. One might expect that the incident laser energy should couple most strongly to the electronic degrees of freedom⁵⁴, and that subsequent trickle-down energy transfer processes would set the magnitude of the KEs of the heavier

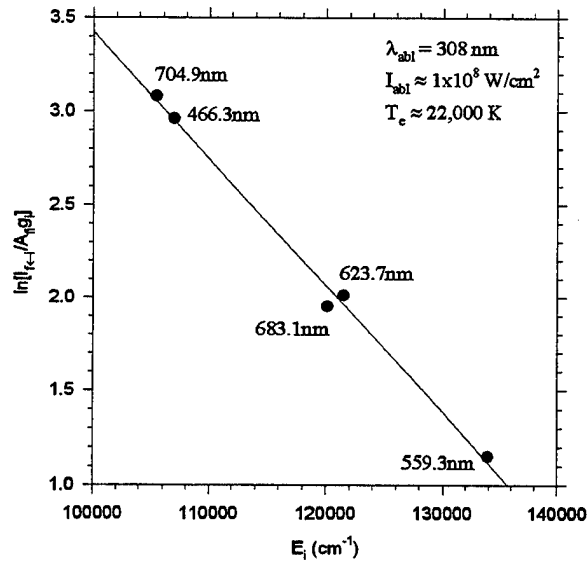


Figure 31. Electronic temperature of laser ablated aluminum plume.

Spectrum recorded at 1.25 mm from the ablation target surface; same experimental conditions as for Figure 29. See Table II for parameters used in T_e calculation.

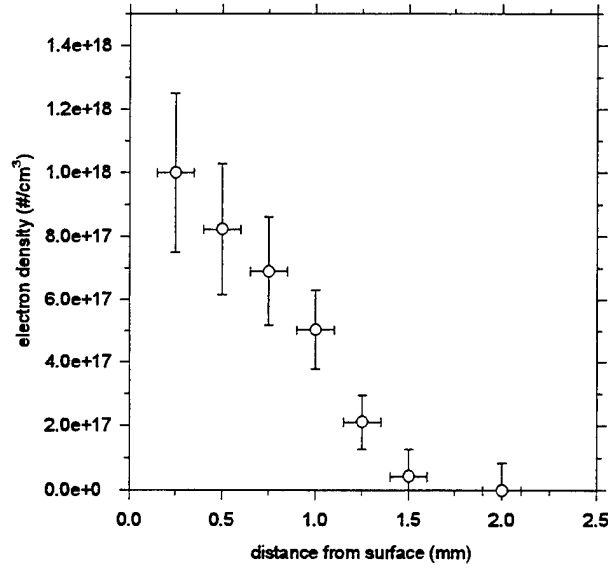


Figure 32. Decay of electron density with distance from ablated surface.
Experimental conditions as in Figure 29.

species⁵⁵. However, the observation of atoms and ions with KEs of 10 to 100 eV issuing from plasmas with $T_e \approx 2$ eV points to the highly nonequilibrium nature of the heavy particle acceleration process, and evokes hydrodynamic^{56,57} and electrostatic^{58,59} explanations.

Another local property available from the experiment depicted in Figure 29 is the number density of free electrons, N_e , which can be estimated from the Stark effect broadening of the emission lines. Under our experimental conditions the linewidth relationship simplifies to⁵²:

$$\Delta\lambda_{\text{true}} (\text{nm}) \approx \frac{N_e (\text{cm}^{-3})}{10^{18}} \quad (16)$$

in which: $\Delta\lambda_{\text{true}}$ is the portion of the observed linewidth due to Stark broadening:

$$\Delta\lambda_{\text{true}} = \Delta\lambda_{\text{observed}} - \Delta\lambda_{\text{instrument}} \quad (17).$$

Figure 32 shows the results of this analysis, using the width of the $\text{Al}^+ 3p^2(^1D) \leftarrow 3s4p(^1P^\circ)$ line at 466.3 nm; the observed linewidth reaches the instrument limit for distances over 2 mm from the surface.

Finally, Figure 33 shows time-resolved emission measurements of the Al atom line at 396.4 nm, and the weaker Al^+ line at 358.6 nm. The rise and fall of the Al atom emission occurs on a timescale much longer than the 7 ns radiative lifetime of the upper 2S state, direct evidence that the population is being continually replenished, probably by the relaxation cascade following electron/ion recombination, and/or by excitation of ground state Al atoms by collisions with electrons.

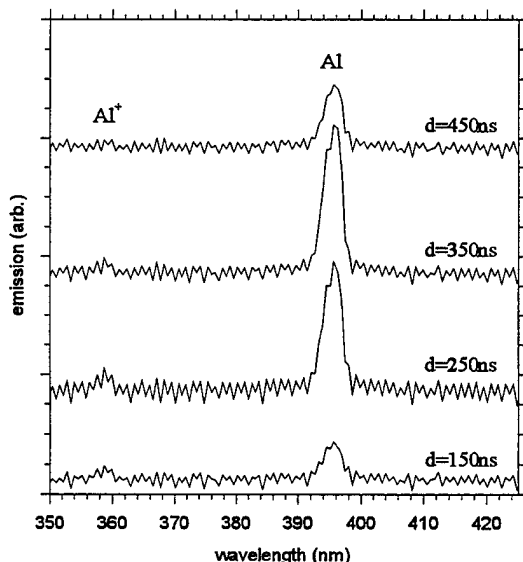


Figure 33. Time-resolved emissions from laser ablated aluminum plume.

Spectra recorded at 3 mm from surface using a 150 ns gate; $\lambda_{abl} = 308$ nm, $I_{abl} \approx 1 \times 10^8$ W/cm².

All the emission data presented in this section point to a picture of the laser ablated plume as a rapidly expanding, cooling plasma, for which LTE of the electronic degrees of freedom holds only in the densest regions within a few millimeters of the target surface. As the plume expands and rarefies, the many-body interactions which promote recombination and equilibration become less frequent, and several energy relaxation mechanisms effectively shut down. Some fraction of the electrons and ions fail to recombine and can be detected at large distances from the ablation target surface (e.g., the Mg⁺ ions in Figure 19). Other electronically excited species, although isolated, can still lose energy by radiative decay. However, spontaneous emission is dramatically less effective in relaxing species in highly excited ‘‘Rydberg states,’’ for which the average radiative lifetime increases as $\tau \sim n^{4.5}$ where n is the principal quantum number⁶⁰. Such species may be able to survive the ~ 10 μ s flight time from the ablation target surface to the detection or deposition region in our experiments.

We have not attempted to detect Rydberg atoms in our atomic beams using, for example, electric field induced ionization^{61,62} with fields of 10^3 to 10^6 V/m. Such an apparatus could be readily attached to our modular TASSPI source, and it seems likely that such an experiment would be successful⁶². Quantifying the content of metastable excited species in our beams would fill in a large hole in our characterization of their purity.

Conclusions: the purity of the atomic beam produced in a TASSPI experiment depends critically on the ablation conditions. For several systems, restricting ablation laser intensities is an effective approach for minimizing the yields of metal clusters and particulates. The presence of metastable electronically excited species is suspected, but remains unproved.

4.5 Maximum Achievable Beam Fluxes

Question: what is the maximum flux of velocity selected atoms obtainable from a laser ablation TASSPI source, and how can present flux levels be improved? In our initial publications, we reported velocity selected Al, Ga, and In atom fluxes of $\Phi \sim 10^{11}$ atoms/cm²-eV-pulse at a working distance of 10 cm from the ablation target surface^{21,22} (Appendices C & D). As shown above in Figure 10, we have also achieved unselected Al atom fluxes of $\Phi \sim 10^{12}$ atoms/cm²-pulse at a working distance of 8 cm.

We have considered a number of approaches towards higher atomic fluxes. Figure 10 also shows how higher atomic fluxes can be obtained by increasing I_{abl} , however this results in the simultaneous production of a profusion of particulates, as discussed above.

The technique of “two-stage” laser ablation^{63,64}, in which ablation occurs from a concave surface, has been demonstrated to produce atomic beams *focused to a spot at the center of curvature of the ablation target surface!* We have noted a related effect in that the divergence of our laser ablated beams appears to decrease as the groove (see Figure 8) is dug into the ablation target surface. Figure 34 shows the angular distribution of aluminum metal deposited onto a glass slide 1 cm from the target surface into which a 0.8 mm wide by 0.3 mm deep groove had been cut by the action of the ablation laser. The distribution is sharply forward peaked; the fit shown is to a $\cos^9(\theta - 5^\circ)$ distribution. We briefly attempted ablation from a precut machined groove, but found no advantage over the naturally occurring groove.

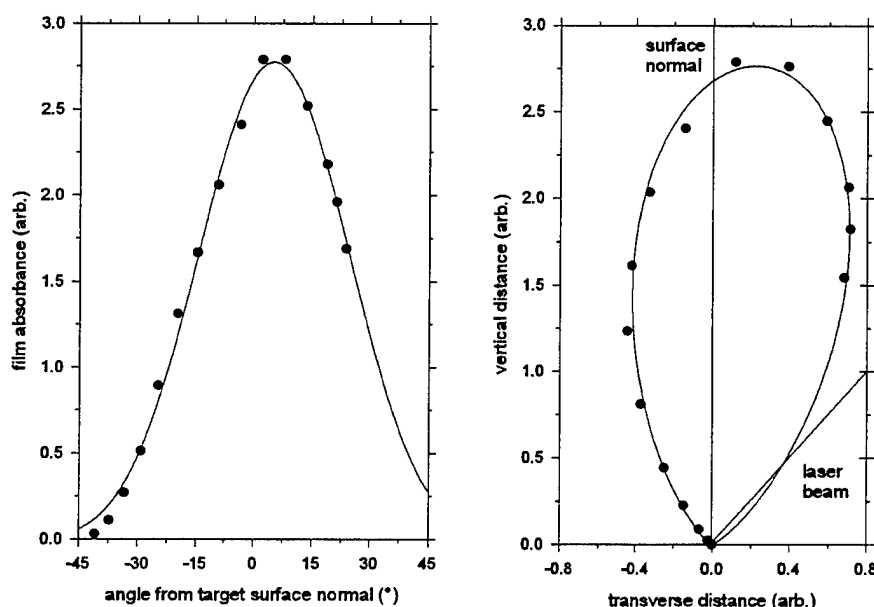


Figure 34. Directionality of laser ablated aluminum plume.

Left panel shows absorbance of an aluminum film deposited on a glass slide 1 cm from target surface; $\lambda_{abl} = 308$ nm, $I_{abl} \approx 1 \times 10^8$ W/cm². Right panel shows a polar plot of the same data.

Our most productive approach to increasing the delivered atomic flux has been to increase the area of the ablation laser focus spot, while maintaining I_{abl} just below the threshold for copious particulate production. The larger ablation spot, combined with a larger (4 mm diameter) beam defining aperture, results in a measurably larger atomic flux along the beam centerline. An example was shown above in Figure 22 for laser ablation of copper metal; the highest film growth rates translate to a Cu atom flux of $\Phi \approx 5 \times 10^{12}$ atoms/cm²-pulse at a working distance of 10 cm. In other experiments, we have managed to deliver up to 100 mJ per pulse to the ablation surface, resulting in fluxes of order 10^{13} atoms/cm²-pulse at 10 cm. The downside to this approach is that as the atomic beam diameter increases, the PI laser pulse energy required to maintain F_{PI} at an appropriate level for TASSPI velocity selection also increases. This would not pose a problem for the Al system, but would require very frugal stewardship of every PI laser photon for the Ga and In systems.

Conclusion: atomic fluxes of $\Phi \sim 10^{13}$ atoms/cm²-pulse have been demonstrated at a distance of 10 cm from the ablation target surface. Higher fluxes might be realized at the expense of higher ablation and PI laser pulse energies, focused to produce larger diameter atomic beams, while keeping I_{abl} low enough to avoid particulate production.

4.6 Matrix Depositions Using TASSPI Geometry

We discussed in the Introduction how this project was originally motivated by our efforts to understand the trapping of metal atoms in cryogenic solids. We had conjectured that the novel effects of new trapping site formation and efficient atomic isolation were caused by "implantation" of fast laser ablated metal atoms into these soft van der Waals solids. Ironically, when we consolidated our TASSPI and matrix deposition apparatus (Figure 35), we

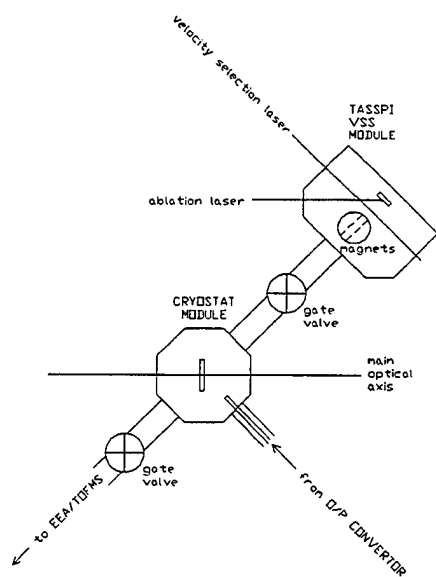


Figure 35. Matrix deposition experimental schematic.

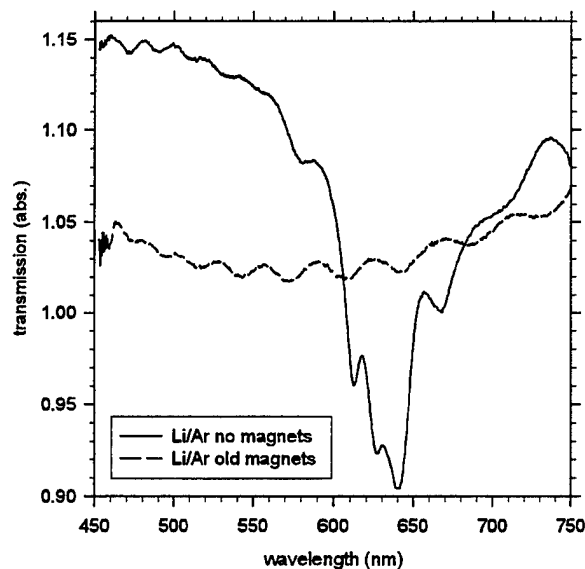


Figure 36. Li/Ar matrices.

As-deposited Li/Ar matrices with $T = 20$ K, $I_{abl} \approx 4 \times 10^7$ W/cm², 30 mJ/pulse, 10 Hz repetition rate, 15 minute Li deposition time, Ar inlet flow rate = 1.1 mmol/hr. The legend "old magnets" refers to the 0.74 cm spacing used in the original deflection magnet assembly which provides a field of 4.4 kGauss at its center.

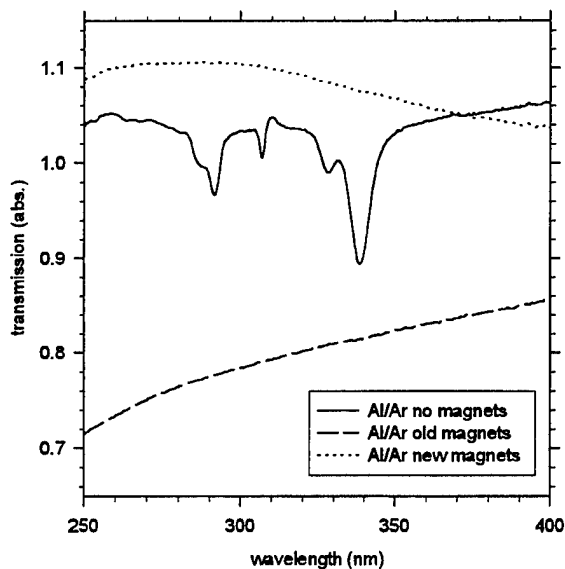


Figure 37. Al/Ar matrices.

As-deposited Al/Ar matrices with $T = 20$ K, $I_{abl} \approx 1.1 \times 10^8$ W/cm², 160 mJ/pulse, 10 Hz repetition rate, 15 min. Al deposition time, Ar inlet flow rate = 1.0 mmol/hr. The legend "new magnets" refers to the 2.0 cm spacing magnet assembly which provides a field of 1.9 kGauss at its center.

demonstrated conclusively that these novel effects are due to deposition and subsequent neutralization of laser ablated nascent metal *ions*, not fast atoms^{65,66}. As Figures 36 and 37 show, we found that simply inserting the ion-rejection magnets into the ablated atomic beam results in the nearly complete loss of the Li and Al atom Ar matrix absorptions. Perversely, the ion-rejection magnets seem to have little effect on the depositions of Li or Al atoms in hydrogen matrices, leaving us without a unified explanation with which to correct our previous misinterpretations.

To date we have not attempted any matrix depositions of velocity selected atoms. Depositions in Ar and other rare gas matrices seem pointless without the spectroscopic diagnostic which accompanies novel trapping site formation. We may eventually pursue TASSPI depositions of Al atoms into hydrogen matrices to determine the KE dependence of the Al atom isolation efficiency, and in particular to investigate the existence of energetic thresholds for any Al-H₂ reactions accompanying the deposition.

5.0 CONCLUSIONS AND RECOMMENDATIONS

We have demonstrated velocity selection of fast laser ablated metal atoms by a novel, non-mechanical technique which we named TASSPI for "Temporally And Spatially Specific PhotoIonization." This approach has a number of advantages over mechanical velocity selection schemes, including compact size, and suitability for use with atomic velocities in excess of 10^6 cm/s. Our successful TASSPI observations are well explained by a simple one-dimensional model invoking prompt production of all species on a timescale comparable to the duration of the ablation laser pulse.

The TASSPI method works remarkably well for Al, Ga, and In atoms, all of which can be efficiently photoionized by commercially available ArF excimer lasers. Photoionization of other atomic and molecular species remains problematic. Future attempts at using REMPI schemes for photoionization might extend the utility of the TASSPI approach to other systems.

The use of static magnetic fields produced by rare-earth/cobalt permanent magnets to deflect unwanted ions from the velocity selected atomic beam is a particularly successful aspect of the TASSPI approach.

Several minor impurities have been identified in atomic beams produced by TASSPI. Less than 1% of the ionic species survive the magnetic deflection field. Residual very fast or very slow metal atoms which avoid illumination by the velocity selection laser can be a major problem for poor choices of ablation/PI laser delays. Metal oxides and hydroxides are produced during the initial "cleaning" of the ablation target surface by the ablation laser. Metal clusters and particulates are produced in large quantities for ablation laser intensities above well defined "threshold" levels, and can be largely avoided by using milder ablation conditions. The presence of metastable electronically excited "Rydberg" atoms seems likely, but remains unquantified.

The atomic fluxes achieved in our experiments are more than adequate for our intended application of matrix isolation spectroscopy, but they remain a little too low to be attractive for other materials sciences applications. We have demonstrated fluxes of 10^{13} atoms/cm²-pulse at a distance of 10 cm from the ablation target surface. Using kilohertz repetition rate excimer lasers would yield average fluxes of 10^{16} atoms/cm²-s, which are just beginning to get interesting for thin-film depositions. Future efforts to increase the atomic flux without sacrificing the purity of the atomic beam should be encouraged.

The production of new materials via deposition of laser ablated species remains an active area of research in applied physics and materials science. We hope that some of the techniques developed in this effort will be useful to future researchers working to improve our understanding of the physical processes occurring during deposition and within the ablated plume itself. We encourage personal inquiries by interested parties with unanswered questions about our work.

ACKNOWLEDGMENTS

The majority of the experimental results presented in this report were obtained at the Propulsion Directorate of the Phillips Laboratory by Dr Michel Macler during his 1992 to 1994 tenure as a National Research Council Postdoctoral Fellow, and during his 1996 to 1997 employment by Hughes STX. Mr Simon Tam collaborated with Dr Macler and Dr Fajardo on the TASSPI matrix isolation experiments.

The authors would like to acknowledge the direct assistance of Dr Franklin B. Mead. Discussions with Dr Mead led to the replacement of the original electrostatic-ion deflection field with a magnetic field. This design modification was crucial to the success of the TASSPI approach.

We thank Mr Jim King for the SEM micrographs, the JPL machine shop for constructing the VSS vacuum module and other hardware, and Dr Eric Kerley of Comstock, Inc. for his assistance in adapting their EEA-TOFMS system to our experiment.

We are also grateful for many valuable discussions with numerous other members of the HEDM community.

The materials comprising Appendices A through D have appeared in previous publications (References 19 through 22), and are reproduced herein with the permission of the American Institute of Physics and the Materials Research Society.

REFERENCES

1. HEDM program progress is documented in a series of technical reports prepared after each annual contractors' conference; the first conference was held in 1987, the most recent example is: Proceedings of the High Energy Density Matter (HEDM) Contractors' Conference Held 5-7 June 1996 in Boulder CO, edited by P.G. Carrick and N.T. Williams, PL-TR-96-3037 (USAF Phillips Laboratory, Edwards AFB, CA, 1997).
2. P.G. Carrick, Specific Impulse Calculations of High Energy Density Solid Cryogenic Rocket Propellants. I. Atoms in Solid H₂, PL-TR-93-3014 (USAF Phillips Laboratory, Edwards AFB, CA 93524-7680, 1993).
3. G.P. Sutton, Rocket Propulsion Elements, 6th edition (Wiley, New York, 1992).
4. S.J. Isakowitz, International Reference Guide to Space Launch Systems, (American Institute of Aeronautics and Astronautics, Washington, DC, 1991).
5. M.E. Fajardo, P.G. Carrick, and J.W. Kenney III, "Matrix isolation spectroscopy of metal atoms generated by laser ablation. I. The Li/Ar, Li/Kr, and Li/Xe systems," J. Chem. Phys. **94**, 5812 (1991).
6. M.E. Fajardo, "Matrix isolation spectroscopy of metal atoms generated by laser ablation. II. The Li/Ne, Li/D₂, and Li/H₂ systems," J. Chem. Phys. **98**, 110 (1993).
7. S. Tam and M.E. Fajardo, "Matrix isolation spectroscopy of metal atoms generated by laser ablation. III. The Na/Ar, Na/Kr, and Na/Xe systems," J. Chem. Phys. **99**, 854 (1993).
8. J.F. Friichtenicht, "Laser-generated pulsed atomic beams," Rev. Sci. Instrum. **45**, 51 (1974).
9. H. Kang and J.L. Beauchamp, "Pulsed laser evaporation and ionization of solid metal targets. Implications for studying the gas-phase reactions of laser-generated atoms and ions," J. Phys. Chem. **89**, 3364 (1975).
10. R. Koppmann, S.M. Refaei, and A. Pospieszczyk, "Spectroscopic study of atomic beams generated by laser ablation of multicomponent targets," J. Vac. Sci. Tech. **A4**, 79 (1986).
11. M. Harnafi and B. Dubreuil, "Some properties of atomic beam produced by laser induced ablation of Li target," J. de Physique **C7**, 677 (1987).
12. K.M. Chen, C.N. Kuo, C.D. Lin, T.F. Tseng, C.C. Pan, M.J. Lin, G.P. Wang, and C.C. Pei, "Characteristics of excimer laser-generated pulsed Na beams," Chem. Phys. Lett. **187**, 198 (1991).

13. Atomic and Molecular Beam Methods, Volume 1, edited by G. Scoles, D. Bassi, U. Buck, and D. Laine (Oxford, New York, 1988).
14. H.U. Hostettler and R.B. Bernstein, "Improved slotted disk type velocity selector for molecular beams," *Rev. Sci. Instrum.* **31**, 872 (1960).
15. L.T. Crowley, M.A.D. Fluendy, and K.P. Lawley, "A radial disk velocity selector for molecular beams," *Rev. Sci. Instrum.* **41**, 666 (1970).
16. G.O. Este, B. Hilko, D. Sawyer, and G. Scoles, "New compact molecular beam velocity selector," *Rev. Sci. Instrum.* **46**, 223 (1975).
17. S.M. Trujillo, P.K. Rol, and E.W. Rothe, "Slotted-disk velocity selector for extended range," *Rev. Sci. Instrum.* **33**, 841 (1962).
18. J. Politiek, P.K. Rol, J. Los, and P.G. Ikelaar, "Atomic beam source for the energy range of 0.2-45 eV," *Rev. Sci. Instrum.* **39**, 1147 (1968).
19. M. Macler and M.E. Fajardo, "Determination of atomic velocity distributions using transient absorption measurements," *Mater. Res. Soc. Proc.* **285**, 105 (1993).
20. M. Macler and M.E. Fajardo, "Comparison of short range and asymptotic measurements of the kinetic energy distributions of laser ablated aluminum atoms," *Appl. Phys. Lett.* **65**, 159 (1994).
21. M. Macler and M.E. Fajardo, "Velocity selection of fast laser ablated aluminum atoms by temporally and spatially specific photoionization," *Appl. Phys. Lett.* **65**, 2275 (1994).
22. M. Macler and M.E. Fajardo, "Velocity selection of laser ablated metal atoms by a novel non-mechanical technique," *Mater. Res. Soc. Proc.* **388**, 39 (1995).
23. M.E. Fajardo and M. Macler, "Velocity selected laser ablation metal atom source," US Patent #5,567,935 (22 October 1996).
24. Note: certain commercial instruments and materials are identified in this manuscript in order to specify adequately the experimental procedure. This does not imply recommendation or endorsement of these products by the US Air Force, nor does it imply that these products are necessarily the best available for the purpose.
25. J.H. Moore, C.C. Davis, M.A. Coplan, Building Scientific Apparatus, (Addison-Wesley, London, 1983).
26. M.J. Shea, R.N. Compton, R.L. Hettich, "Laser ablation studies of palladium electrolytically loaded with hydrogen and deuterium," *Phys. Rev. A* **42**, 3579 (1990).

27. Not stated explicitly, but implicit in the data from Ref. 12, see their Figure 2.
28. D.B. Geohegan and D.N. Mashburn, "Characterization of ground state neutral and ion transport during laser ablation of $Y_1Ba_2Cu_3O_{7-x}$ using transient optical absorption spectroscopy," *Appl. Phys. Lett.* **55**, 2345 (1989).
29. D.B. Geohegan, "Imaging and blackbody emission spectra of particulates generated in the KrF-laser ablation of BN and $YBa_2Cu_3O_{7-x}$," *Appl. Phys. Lett.* **62**, 1463 (1993).
30. R.D. Hudson and L.J. Kieffer, "Compilation of atomic ultraviolet photoabsorption cross sections for wavelengths between 3000 and 10 Å," *Atomic Data* **2**, 205 (1971).
31. M.G. Kozlov, E.I. Nikonova, and G.P. Startsev, "Vacuum absorption spectra of the vapors of metals of the aluminum group. I. thallium and aluminum," *Opt. Spectrosc.* **21**, 298 (1966).
32. M.G. Kozlov and G.P. Startsev, "Vacuum-ultraviolet absorption spectra of the vapors of metals of the aluminum group. II. gallium and indium," *Opt. Spectrosc.* **24**, 3 (1968).
33. M. Vershuis and G. Meijer, "Intracavity C atom absorption in the tuning range of the ArF excimer laser," *J. Chem. Phys.* **96**, 3350 (1992).
34. W.L. Wiese and G.A. Martin, "Atomic Spectroscopy," in A Physicist's Desk Reference, edited by H.L. Anderson, (American Institute of Physics, New York, 1989).
35. V.S. Letokhov, V.I. Mishin, and A.A. Puretzky, "Selective photoionization of atoms by laser radiation and its applications," *Prog. Quant. Electr.* **5**, 139 (1977).
36. G.S. Hurst, M.G. Payne, S.D. Kramer, and J.P. Young, "Resonance ionization spectroscopy and one-atom detection," *Rev. Mod. Phys.* **51**, 767 (1979).
37. V.S. Letokhov, Laser Photoionization Spectroscopy, (Academic, Orlando, FL, 1987).
38. M.G. Payne, L. Deng, N. Thonnard, "Applications of resonance ionization mass spectrometry," *Rev. Sci. Instrum.* **65**, 2433 (1994).
39. M. Shimauchi, T. Miura, and S. Karasawa, "Absorption lines in the ArF and KrF laser spectra," *J. Chem. Phys.* **71**, 3538 (1979).
40. E.M. Purcell, Electricity and Magnetism, (McGraw-Hill, New York, 1965).
41. J.D. Jackson, Classical Electrodynamics, (Wiley, New York, 1975).

42. F. Kokai, Y. Koga, and R.B. Heimann, "Magnetic field enhanced growth of carbon cluster ions in the laser ablation plume of graphite," *Appl. Surf. Sci.* **96**, 261 (1996).
43. A.P. French and E.F. Taylor, An Introduction to Quantum Physics, (W.W. Norton, New York, 1978).
44. D.M. Cox, D.J. Trevor, R.L. Whetten, E.A. Rohlfing, and A. Kaldor, "Aluminum clusters: magnetic properties," *J. Chem. Phys.* **84**, 4651 (1986).
45. G. Koren, A. Gupta, R.J. Baseman, M.I. Lutwyche and R.B. Laibowitz, "Laser wavelength dependent properties of $\text{YBa}_2\text{Cu}_3\text{O}_{7.8}$ thin films deposited by laser ablation," *Appl. Phys. Lett.* **55**, 2450 (1989).
46. G. Koren, R.J. Baseman, A. Gupta, M.I. Lutwyche and R.B. Laibowitz, "Particulates reduction in laser ablated $\text{YBa}_2\text{Cu}_3\text{O}_{7.8}$ thin films by laser-induced plume heating," *Appl. Phys. Lett.* **56**, 2144 (1990).
47. R.K. Singh, D. Bhattacharya, and J. Narayan, "Subsurface heating effects during pulsed laser evaporation of materials," *Appl. Phys. Lett.* **57**, 2022 (1990).
48. D. Bhattacharya, R.K. Singh, and P.H. Holloway, "Laser-target interactions during pulsed laser deposition of superconducting thin films," *J. Appl. Phys.* **70**, 5433 (1991).
49. H. Izumi, K. Ohata, T. Sawada, T. Morishita, and S. Tanaka, "Cumulative laser irradiation effects on ions in the plume of $\text{YBa}_2\text{Cu}_3\text{O}_{7.8}$ and particulates at the film surface," *Appl. Phys. Lett.* **59**, 2950 (1991).
50. E. van de Riet, C.J.C.M. Nillesen, and J. Dieleman, "Reduction of droplet emission and target roughening in laser ablation and deposition of metals," *J. Appl. Phys.* **74**, 2008 (1993).
51. Y. Watanabe, M. Tanamura, S. Matsumoto, and Y. Seki, "Laser power dependence of particulate formation on pulse laser deposited films," *J. Appl. Phys.* **78**, 2029 (1995).
52. J.T. Knudtson, W.B. Green, and D.G. Sutton, "The UV-visible spectroscopy of laser-produced aluminum plasmas," *J. Appl. Phys.* **61**, 4771 (1987).
53. W.L. Wiese, M.W. Smith, and B.M. Miles, Atomic Transition Probabilities Vol II Sodium Through Calcium, (NSRDS-NBS 22, US Gov. Printing Office, 1969).
54. R.F. Haglund, Jr. and R. Kelly, "Electronic Processes in Sputtering by Laser Beams," in Fundamental Processes in Sputtering of Atoms and Molecules (SPUT92), edited by P. Sigmund (Royal Danish Academy of Sciences and Letters, Copenhagen, 1993).

55. F.X. Campos, C.J. Waltman, and S.R. Leone, "Laser vaporization time-of-flight studies of cryogenic Cl₂/Xe films," *Chem. Phys. Lett.* **201**, 399 (1993).
56. R. Kelley, "Gas dynamics of the pulsed emission of a perfect gas with applications to laser sputtering and to nozzle expansion," *Phys. Rev. A* **46**, 860 (1992).
57. J.C.S. Kools, T.S. Baller, S.T. DeZwart, and J. Dieleman, "Gas flow dynamics in laser ablation deposition," *J. Appl. Phys.* **71**, 4547 (1992).
58. Y.A. Bykovskii, N.N. Degtyarenko, V.F. Elesin, Y.P. Kozyrev, and S.M. Sil'nov, "Mass spectrometer study of laser plasma," *Soviet Phys. JETP* **33**, 706 (1971).
59. J.C.S. Kools, S.H. Brongersma, E. van de Riet, and J. Dieleman, "Concentrations and velocity distributions of positive ions in laser ablation of copper," *Appl. Phys. B* **53**, 125 (1991).
60. H.A. Bethe and E.E. Salpeter, Quantum Mechanics of One- and Two-Electron Systems, (Plenum, New York, 1957).
61. W. Demtroder, Laser Spectroscopy, (Springer-Verlag, Berlin, 1982).
62. R.P. van Ingen, "Detection of electric-field-ionized Rydberg atoms originating from laser ablation of Si," *J. Appl. Phys.* **79**, 467 (1996).
63. M.A. Kadar-Kallen and K.D. Bonin, "Focusing of particle beams using two-stage laser ablation," *Appl. Phys. Lett.* **54**, 2296 (1989).
64. M.A. Kadar-Kallen and K.D. Bonin, "Generation of dense, pulsed beams of refractory metal atoms using two-stage laser ablation," *Appl. Phys. Lett.* **64**, 1436 (1994).
65. M.E. Fajardo, M. Macler, and S. Tam, "Progress Towards Deposition of Velocity Selected Aluminum Atoms into Cryogenic para-Hydrogen Matrices," in Ref. 1.
66. D.C. Silverman and M.E. Fajardo, "Matrix isolation spectroscopy of Na atoms deposited as Na⁺ ions," *J. Chem. Phys.* **106**, 8964 (1997).

APPENDIX A

105

DETERMINATION OF ATOMIC VELOCITY DISTRIBUTIONS USING TRANSIENT ABSORPTION MEASUREMENTS

MICHEL MACLER* AND MARIO E. FAJARDO

Emerging Technologies Branch, Propulsion Directorate, Phillips Laboratory,
OLAC PL/RKFE, 9 Antares Road, Edwards Air Force Base, CA 93524-7680.

*AFMC PL/NRC Post-doctoral Research Associate.

ABSTRACT

Results of experiments on Al, Li, and Na atomic beams produced by laser ablation using XeCl excimer laser pulses ($1 \sim 10^7$ to 10^8 W/cm²) are presented. Plume emission spectra showed that further than ~ 5 mm from the targets most of the excited ablated species are in neutral, atomic form. Transient absorption measurements permitted the detection of ground state atoms with different flight times, at fixed distances from the target. The resulting time of flight (TOF) distributions were converted into velocity and kinetic energy (KE) distributions. The measured fluxes of fast atoms always increased with ablation laser intensity. The velocity distributions could not be fitted to Maxwell-Boltzmann (MB), or MB plus stream velocity type distributions.

For Al plumes, comparison of velocity distributions measured at various distances from the target surface indicates that Al atoms are produced within ~ 100 nsec following the leading edge of the ablation laser pulse, implying that there is a one-to-one mapping of the initial velocities to the distances traveled by the atoms after ~ 1 μ sec. This result should encourage efforts to develop a method of velocity selection of laser ablated metal atoms based on the spatial separation of the various velocity components along the direction of travel.

INTRODUCTION

Recent successful efforts at isolating light metal atoms in cryogenic solid hydrogen have utilized a combination of pulsed laser ablation of the metal, and traditional matrix isolation spectroscopy (MIS) techniques [1,2]. These experiments suggest that the incident KE of the metal atoms plays a key role in determining the atomic isolation efficiency of the matrix deposition process, and in the formation of novel metal atom trapping site structures. Unfortunately, little work has been done to measure the KE distributions of laser ablated species prior to matrix isolation. Thus, the immediate goals of this research effort are: (1) to characterize the chemical identity and KE distributions of laser ablated species under *our* specific experimental conditions, and (2) to examine the possibility of modifying the nascent metal atom KE distributions through a modification of the traditional laser ablation process.

EXPERIMENTAL

Fig. 1 depicts the experimental setup, configured for transient absorption measurements. The metal ablation targets are mounted on a rotatable rod within a vacuum chamber pumped directly by a small turbomolecular pump to $\sim 10^{-6}$ Torr. The ablated plumes are formed by focusing a XeCl excimer laser beam on the targets at an incident angle of 45° from the surface normal. The incident laser pulse energies were varied between 3 and

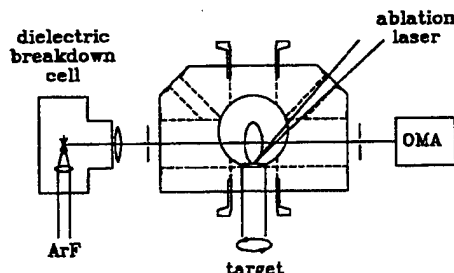


Fig. 1: Schematic of the apparatus used for the transient absorption experiments. The ellipse extending from the target represents the ablated plume.

14 mJ; the pulse duration was measured as 30 nsec FWHM, and the pulses were focused onto a $\sim 0.25 \text{ mm}^2$ area, resulting in incident intensities (I) of 2×10^7 to $1 \times 10^8 \text{ W/cm}^2$.

To examine the directionality of the plume expansion, glass microscope slides were placed 10 mm from the target in order to collect the products of ablation. The thickness of the Al films deposited in this manner were assumed to be proportional to their optical density (O.D.) measured as a function of angle from the ablation target surface normal.

Emissions from the metal plumes were filtered to remove laser scatter, and recorded with an intensified, gated, optical multichannel analyzer (OMA) mounted on a 275 mm f.l. polychromator. The detection system was both wavelength and intensity calibrated using standard techniques. The observation region, a $\sim 200 \text{ }\mu\text{m}$ wide transverse slice of the plumes, was defined by a $100 \text{ }\mu\text{m}$ wide aperture adjacent to the vacuum chamber and the $25 \text{ }\mu\text{m}$ wide entrance slit of the polychromator. The entire mask/filter/polychromator assembly was mounted on a precision translator which was controlled manually by a micrometer positioner. Emission spectra were recorded at various distances, Z , from the target with a $10 \text{ }\mu\text{sec}$ detector gate.

Transient absorption spectra were obtained as shown in Fig. 1. Short, polychromatic pulses were produced by using a second excimer laser (ArF) to pump a dielectric breakdown cell filled with ~ 1000 Torr of Xe gas, or a Xe:Ne mixture. A 50 mm f.l. quartz lens collimated this emission through the metal atom plumes and onto the polychromator entrance slit. A digital delay generator was used to coordinate the arrival of the ablation and breakdown laser pulses, and the start of the 20 nsec wide OMA detector gate. The delays between ablation and detection were varied between 0.2 and $3.0 \text{ }\mu\text{sec}$. As no metal atom emissions were detected with this experimental configuration, transmission spectra were calculated as the ratio between the OMA signals obtained with both ablation and breakdown laser pulses present (S), and that obtained with breakdown pulses only (S_0). Both S and S_0 signals were averaged over 100 pulses. As with emission spectra, the transient absorption spectra were obtained at various distances from the ablation target surface.

RESULTS

The Al deposit optical density data was fitted to $\text{O.D.} = k \cos^n(\theta - \theta_0)$, where θ is the angle with the surface normal, and θ_0 is the tilt of the axis of the plume. The fit yielded $n \approx 9$, and the tilt angle $\theta_0 \approx 5^\circ$, indicative of a highly directional, near normal plume which justifies the simple, one-dimensional analysis of the TOF measurements on Al plumes. No such measurements were attempted for Li or Na plumes (*vide infra*).

The Al atomic and ionic emission spectra were used to characterize the properties of the plasma formed adjacent to the ablated aluminum surface. The use of a long detection gate (10 μ sec) yielded fully time integrated spectra, as all emissions were finished on this time scale. Ionic emission peaks dominated near the target surface, but became barely noticeable for distances $Z > 3$ mm. Integrated emission intensities were extracted for a number of transitions for which the term values, E , degeneracy factors, g , and radiation rates, A , of the upper states were readily available [3]. Electron temperatures (T_e) were extracted by assuming local thermodynamic equilibrium (LTE) [4,5]. Typically, for $0.8 < Z < 2.0$ mm, the plasmas were dense enough for LTE to hold, and T_e was of order 20000 K (~ 2 eV). Electron densities (N_e) were also derived from emission spectra by measuring the Stark broadening of ionic lines [4]. For $0.8 < Z < 1.3$ mm, N_e decreased rapidly from 7×10^{17} to $< 8 \times 10^{16}$ cm^{-3} , correlating strongly with the disappearance of the Bremsstrahlung continuum, and the decrease in Al(III) emissions.

Typical transient absorption spectra of Al plumes displayed the atomic doublet at 394.5 and 396.2 nm with a signal-to-noise (S:N) ratio of better than 20:1. For Al and Na, no attempt to observe either excited or ionic state absorptions were made. However, for Li, the $3d \leftarrow 2p$ absorption was observed at $Z = 20$ mm for delay times in the 0.6-1.6 μ sec range. From this observation, the relative population of the Li 2p state was estimated to be $\sim 10\%$ of that of the ground state. The time evolution of the absorption intensity following the ablation laser pulses gives the TOF distribution of the ground state atoms. For Al, TOF distributions were measured at $Z = 5$ and 10 mm; the raw data are displayed in Fig. 2. An important correction to the raw TOF data was required since metal atoms traveling faster than $v^* = (\text{width of observation region})/(\text{detection time}) = (200 \mu\text{m}/20 \text{ nsec}) = 1 \times 10^6$ cm/sec spent less than 20 nsec in the observation region, and thus had a lower detection probability than slower atoms. Thus, we corrected all TOF data for the following detection probabilities, $P(v)$:

$$\begin{aligned} P(v) &= 1 & \text{for } v \leq v^*, \\ P(v) &= v^* / v = v^* t / Z & \text{for } v > v^*. \end{aligned} \quad (1)$$

The transformation of the TOF distributions into velocity and KE distributions also deserves special attention, as the differential element, dt , in the TOF distribution is not equal to the dv or dE appearing in the velocity and KE distributions, respectively. Consequently, when converting TOF distributions into velocity distributions, we used the following equation:

$$N_{\text{vel}}(v)dv = \frac{(t^2/Z)N_{\text{TOF}}(Z/v)dt}{P(v^*t/Z)} \quad (2)$$

Al velocity distributions are presented in Fig. 3. Similarly, for converting TOF distributions into KE distributions, we used:

$$N_E dE = \frac{(2t^3/mZ^2)N_{\text{TOF}}(Z/(2E)^{1/2})dt}{P(v^*t/Z)} \quad (3)$$

Al KE distributions are presented in Fig. 4.

Laser ablation transient absorption measurements of Li and Na yielded TOF distributions with a sharp, intense peak occurring for short delays, followed by a persistent "tail" at long delays (> 10 msec). This behavior was seen for the entire range of laser intensities used in these experiments. We suspect that these long delay tails are artifacts of

our experimental geometry: the plume expansions for Li and Na may be less directional than for Al, so Li and Na atoms may enter the observation region at large angles from the surface normal. Because of this difficulty, only the short arrival time portions of the Li and Na KE distributions are presented in Figs. 5 and 6, respectively.

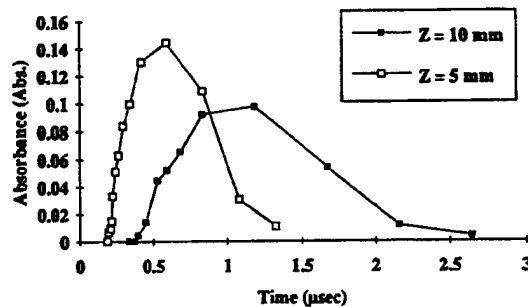


Fig. 2: TOF spectrum of ground state Al atoms, recorded by monitoring the $4s \leftarrow 3p$ absorption doublet for ablation intensities $\sim 10^8 \text{ W/cm}^2$.

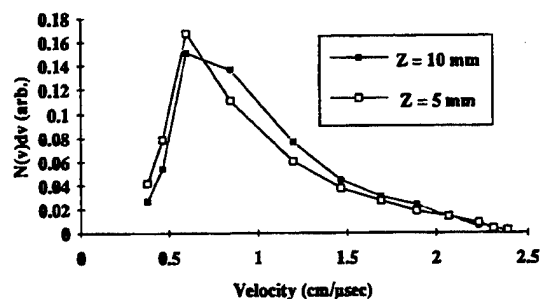


Fig. 3: Velocity distribution for ground state Al atoms obtained after using eqn. (1) and eqn. (2).

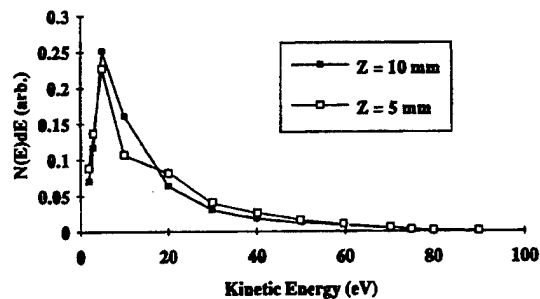


Fig. 4: Kinetic energy distribution for ground state Al atoms obtained after using eqn. (3).

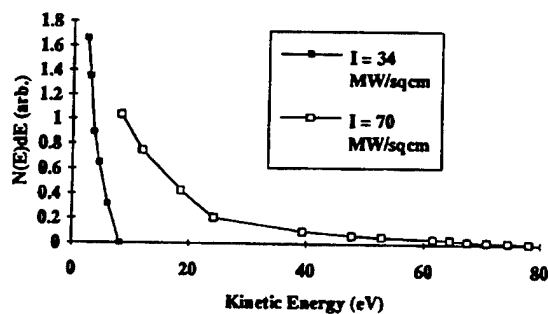


Fig. 5: Kinetic energy distributions for ground state Na atoms obtained from measurements made for $Z = 10$ mm, at laser intensities in the 3.4×10^7 to 7.0×10^7 W/cm² range.

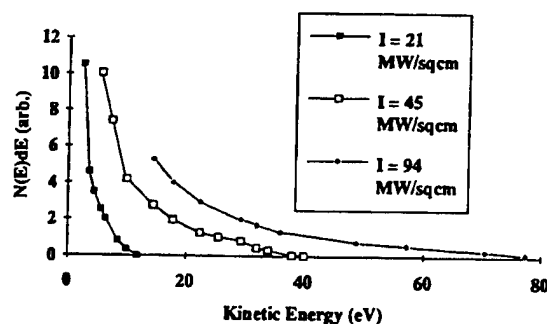


Fig. 6: Kinetic energy distributions for ground state Li atoms obtained from measurements made for $Z = 10$ mm, at laser intensities in the 2.1×10^7 to 9.4×10^7 W/cm² range.

DISCUSSION AND CONCLUSIONS

The emission and transient absorption measurements indicate that at distances greater than $Z \approx 5$ mm from the metal surface the major constituent of the laser ablated plumes are ground state metal atoms. The Al atom velocity distributions obtained from the transient absorption measurements were similar to those measured by other means for similar laser intensities [6-8]. We attempted to fit the observed Al atom velocity distributions to the MB form without much success; such difficulties have been reported before [6,8]. Similarly, fits were attempted to a modified MB form [9] that included a stream velocity; the extra parameter resulted in only a slightly better fit. The high typical KE's of the atoms (~ 10 eV for $I = 1.0 \times 10^8$ W/cm² for Al atoms) are especially puzzling in view of the much lower electronic temperatures (~ 2 eV) measured under the same conditions. In all the cases studied, the high KE tails of the distributions (which can stretch out to 80 eV) remain unexplained. These results all point to the highly non-equilibrium nature of the process which imparts these velocities to the metal atoms. The Al atom velocity distributions observed at $Z = 5$ and $Z = 10$ mm were not identical, as shown in Fig. 3. We attribute the

small difference to a finite production time for the Al atoms following the arrival of the ablation laser pulse. Simple stochastic computer simulations of our experiment suggest a ~ 100 nsec wide "window" for the establishment of an initial velocity distribution, followed by an essentially free expansion thereafter. This interpretation implies that there is a good one-to-one mapping of the initial velocities to distances traveled from the target after a delay of ~ 1 μ sec. We will continue to pursue efforts to develop a velocity selected laser ablation metal atom source based on this spatial separation of the different velocity components.

REFERENCES

1. M.E. Fajardo, P.G. Carrick, J.W. Kenney III, J. Chem. Phys. **94**, 5812 (1991).
2. M.E. Fajardo, J. Chem. Phys. (accepted 1993).
3. C.E. Moore, Atomic Energy Levels, Vol. I (Nat. Bur. Stand., Washington, D.C., 1971), pp. 47-50.
4. J.T. Knudtson, W.B. Green, D.G. Sutton, J. Appl. Phys. **61**, 4771 (1987), and references therein.
5. R. Tambay, R. Singh, R. Thareja, J. Appl. Phys. **72**, 1197 (1992).
6. H. Wang, A.P. Salzberg, B.R. Weiner, Appl. Phys. Lett. **59**, 935 (1991).
7. R.M. Gilgenbach and P.L.G. Ventzek, Appl. Phys. Lett. **58**, 1597 (1991).
8. R.W. Dreyfus, R. Kelly, R.E. Walkup, Appl. Phys. Lett. **49**, 1478 (1986).
9. J.C.S. Kools, T.S. Baller, S.T. De Zwart, J. Dieleman, J. Appl. Phys. **71**, 4547 (1992).

APPENDIX B

Comparison of short range and asymptotic measurements of the kinetic energy distributions of laser ablated aluminum atoms

Michel Macler^{a)} and Mario E. Fajardo

Propulsion Directorate/RKFE, Phillips Laboratory, Edwards AFB, California 93524-7680

(Received 17 February 1994; accepted for publication 30 April 1994)

We compare the kinetic energy distributions of ultraviolet excimer laser ablated Al atoms measured within 1 cm of the metal surface by optical transient absorption, to those measured over 20 cm from the surface by pulsed photoionization time-of-flight mass spectrometry. For the mild ablation conditions used the distributions are the same. This result demands the existence of a good one-to-one correspondence of atomic velocity to distance traveled from the ablated surface on the $\sim 1 \mu\text{s}$ timescale of the short range measurement, suggesting that the duration of the Al atom production period is $\leq 100 \text{ ns}$. This study establishes the viability of a novel concept for a compact velocity selection scheme for faster laser ablated neutral species.

We have been investigating the production of cryogenic solid hydrogen samples doped with laser ablated metal atoms for use as prototypical high energy density matter (HEDM) systems.¹⁻⁴ Our experiments suggest that the incident kinetics energy (KE) of the metal atoms plays a key role in determining the atomic isolation efficiency of the sample deposition process,¹ and in the formation of novel metal atom trapping site structures.² We have recently published⁵ the results of our efforts to characterize the KE distributions (KEDs) of laser ablated species via optical transient absorption⁶ (OTA) methods; in this manuscript we include new OTA data and a comparison to results obtained with an electrostatic energy analyzer time of flight mass spectrometer (EEA/TOFMS) system⁷ employing pulsed laser photoionization (PI) of neutrals.

Figure 1 is a schematic diagram of the experimental apparatus. The aluminum ablation target is mounted on a rotatable rod within a high vacuum chamber pumped directly by a small turbomolecular pump to $\sim 10^{-6}$ Torr. The ablated plumes are formed by focusing a XeCl excimer laser beam ($\lambda=308 \text{ nm}$) on the target at an incident angle of $\theta \sim 45^\circ$ from the surface normal. The incident laser pulse energies vary between 3 and 15 mJ and are focused to incident intensities (I_{ab}) of 2×10^7 – $1 \times 10^8 \text{ W/cm}^2$; typical pulse repetition rates are $\sim 5 \text{ Hz}$. We estimate the threshold for visible plasma formation as $I_{\text{ab}} \sim 2.5 \times 10^7 \text{ W/cm}^2$. Our previous studies have shown that after a few minutes of operation, a circular track is cut into the metal target surface which serves to direct the ablation products into a narrow plume; we have measured total aluminum mass fluxes with angular dependences of $\sim \cos^3(\theta)$. This geometry and these ablation conditions provide for stable operation and continuous data acquisition for well over an hour.

We probe the ablated plumes via OTA by using a second excimer laser (ArF, 193 nm) to pump a dielectric breakdown cell filled with $\sim 1000 \text{ Torr}$ of Xe gas. The resulting short polychromatic pulses are collimated by a 5 cm focal length (f.l.) quartz lens and pass through a pair of narrow slits which define the $\Delta x \sim 0.02\text{-cm}$ -wide observation region. The

raw optical data are recorded with an intensified, gated, optical multichannel analyzer (OMA) mounted on a 275 mm f.l. polychromator. A digital delay generator is used to coordinate the arrival of the ablation and breakdown laser pulses and the start of the $\Delta t \sim 20\text{-ns}$ -wide OMA detector gate. Typically, no metal atom emissions are detected with this geometry, thus OTA spectra are calculated as $A = -\log_e(I/I_0)$ in which I is the OMA signal obtained with both ablation and breakdown laser pulses present, and I_0 that obtained with breakdown pulses only. Both I and I_0 signals are averaged over 100 pulses; an Al atom OTA spectrum is depicted in Fig. 2. We integrate these OTA spectra obtained at various delays after the ablation laser pulse, and correct for the velocity dependent detection probability (for Al atom velocities greater than $\Delta x/\Delta t \sim 10^6 \text{ cm/s}$) to yield the TOF distributions, $N(t)dt$, for the Al atoms.⁵ We have previously presented the equations required for properly transforming these data to yield the velocity, $N(v)dv$, and KE, $N(\text{KE})d\text{KE}$, distributions.⁵ The entire breakdown cell/mask/polychromator assembly is mounted on a precision translator which allows the OTA spectra, and velocity and KE distri-

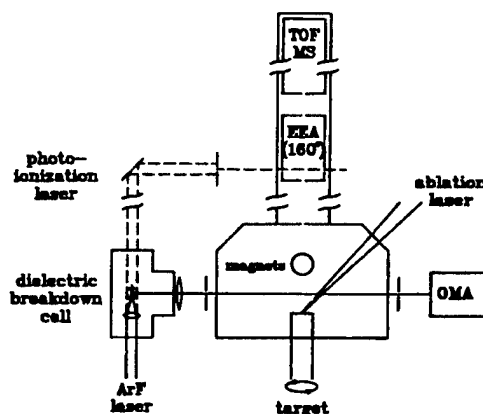


FIG. 1. Experimental diagram.

^{a)}National Research Council Postdoctoral Research Associate.

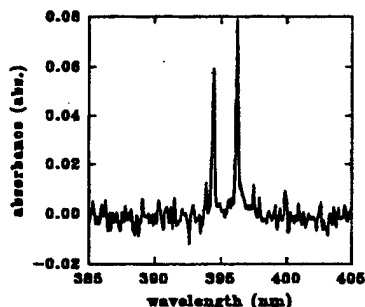


FIG. 2. Optical transient absorption spectrum of laser ablated Al atoms ($3s^24s-3s^23p$ spin-orbit doublet) measured 0.5 cm from the ablated surface at a delay of 0.90 μ s following the ablation laser pulse ($I_{abl} \sim 8 \times 10^7$ W/cm 2).

butions, to be obtained as a function of distance from the ablation target surface.

Our arrangement for measuring the Al atom KEDs with a commercially available EEA/TOFMS system⁷ is also shown in Fig. 1. The EEA/TOFMS components are housed in an ultrahigh vacuum enclosure separated from the ablation source region by a 0.2-cm-diam aperture, and differentially pumped to $\sim 10^{-8}$ Torr. We operate the EEA at a constant internal pass energy of $E_{pass} = 10.0$ eV, and with a mechanical configuration which yields a constant energy resolution of $\Delta E_{EEA} \sim 0.27$ eV. The incident KE of the ions transmitted by the EEA is controlled by biasing the entire EEA relative to the vacuum enclosure.

The atomic beam is defined by the ablation laser impact spot and the 0.2-cm-diam isolation aperture which is located ~ 6 cm from the aluminum metal surface. For making measurements of the Al atom KEDs, we use a permanent magnetic field to deflect the nascent Al^+ ions out of the atomic beam. We sandwiched two 1.2-cm-diam permanent magnets on a 0.5-cm-thick polymer spacer in which we had drilled a 0.3-cm-diam clear hole at 90° to the magnetic field. This arrangement provides a 2.8 kG deflection field which, when located 2.5 cm from the ablation target surface, efficiently rejects Al^+ ions with KEs below about 30 eV. This downstream magnetic field has no apparent effect on the Al atom KEDs measured by OTA at distances of 1.0 and 0.5 cm from the metal surface.

We take advantage of an extremely strong ($\sigma \sim 10^{-16}$ cm 2) autoionization resonance⁸ of the Al atoms coincident with the 193 nm ArF excimer laser output to ionize the Al atoms with over 98% efficiency by a single photon process. This PI scheme makes the measurements most sensitive to ground state Al atoms. The PI beam is ~ 0.5 cm wide and intersects the atomic beam in the ionization region of the EEA, $x_{PI} \sim 22.5$ cm from the ablation target surface. The finite width of the ionization region, Δx_{PI} , contributes an additional uncertainty, ΔE_{PI} , to the KE measurements, since $\Delta E_{PI}/KE = 2\Delta x_{PI}/x_{PI} \sim 0.44$; ΔE_{PI} becomes greater than ΔE_{EEA} for $KE > 6$ eV. The ions that are transmitted by the EEA are accelerated to ~ 2.0 keV, pass through the 1 m TOF

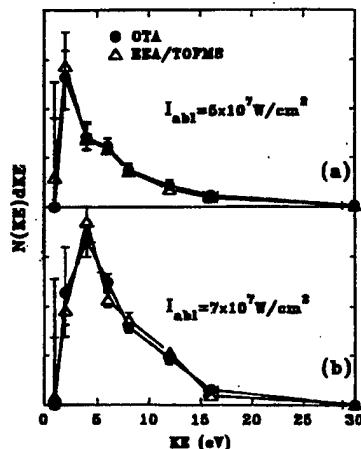


FIG. 3. Comparison of KEDs of Al atoms measured by OTA at $x \sim 0.5$ cm and by EEA/TOFMS at $x \sim 22.5$ cm. The error bars represent the $\pm 1\sigma$ limits. The KEDs in each panel are normalized to same total integrated areas. Both panels are plotted using the same scaling; the ratio of the total fluxes of Al atoms for the two KEDs is $\Phi(b)/\Phi(a) \sim 1.6$.

tube, and are detected by a low gain ($\times 10^3$) microchannel plate (MCP) detector.

This combination of pulsed laser PI and electrostatic energy analysis, along with the time dependence of the MCP signal, gives ostensibly redundant TOF information which is in fact crucial to identifying any non-Al atom Al^+ precursors present in the PI region. Aluminum clusters and particles are produced in abundance for $I_{abl} \geq 7 \times 10^7$ W/cm 2 ; they, along with the ablation products of surface oxides and other contaminants, can contribute to the MCP detector signal if photofragmented and photoionized⁹ by the ArF laser to produce ions of the proper KE to transit the EEA. These photofragment ions can be distinguished from the Al^+ formed by PI of Al atoms by their arrival times at the MCP: the former appear at fixed delays from the PI laser while the latter appear at a fixed delay from the ablation laser. This effect can serve as a very sensitive diagnostic for the presence of nonatomic species in the ablated plume,¹⁰ however, if unrecognized, it can lead to a gross overestimation of the low KE ablated Al atom flux. In this study we concentrate on the ablated Al atoms by integrating the MCP signal over just the narrow range of appropriate Al^+ arrival times, as determined in low ablation intensity PI experiments, and in measurements of nascent ablated Al^+ ions made without the rejection magnets. By varying the delay between the ablation and PI lasers and integrating the MCP signals as discussed above, we obtain the TOF distributions of the Al atoms arriving at the PI region with a given KE. These TOF distributions for each KE are in turn integrated to yield directly the contributions to the KEDs.

Figure 3 shows a comparison of the Al atom KEDs obtained by the OTA method at $x \sim 0.5$ cm, and by the EEA/TOFMS technique, obtained at two different ablation laser intensities. Data from the two techniques were obtained in

consecutive experiments and should represent directly comparable ablation conditions. In both cases the agreement is remarkably good, even considering the large error bars on the low KE OTA data. These data are also typical of Al atom KEDs obtained at moderate ablation laser intensities by other techniques.¹¹⁻¹⁴

The observed agreement between the "short range" OTA and "long range" EEA/TOFMS data requires the existence of a good one-to-one correspondence between atomic velocity and distance traveled from the ablated surface at the time of the OTA measurement. This, in turn, suggests that, for our experimental conditions, the temporal and spatial scales of the processes that determine the KEDs of the laser ablated Al atoms are much smaller than the $\sim 1 \mu\text{s}$ time and 0.5 cm length scales of the OTA measurements. Lower limits for these KED preparation time and length scales can be estimated from the ablation conditions: For our ablation laser temporal profile, over 90% of the energy is delivered within ~ 50 ns; typical ablation products velocities of $\sim 10^6$ cm/s imply expansion of the plume to ~ 0.05 cm dimensions. Processes such as Knudsen layer formation,¹⁵ or other gasdynamic and plasma hydrodynamic considerations may stretch out the establishment of the KEDs, particularly at higher ablation laser intensities which provide for higher mass and energy densities. However, our results limit such processes to a timescale of ≤ 100 ns, under the present experimental conditions.

In fact, we have recently exploited this spatial separation of the various velocity components along the direction of travel to demonstrate velocity selection of the Al atoms by a novel, compact, nonmechanical technique. These experiments are still in a preliminary stage; we will report our results upon their completion.¹⁶

¹M. E. Fajardo, *J. Chem. Phys.* **98**, 110 (1993).

²S. Tam and M. E. Fajardo, *J. Chem. Phys.* **99**, 854 (1993).

³*Proceedings of the High Energy Density Matter (HEDM) Contractors' Conference, held 6-8 June 1993 in Woods Hole, MA*, edited by T. L. Thompson (USAF Phillips Laboratory, Edwards AFB, CA, 1993).

⁴A. T. Pitt, Jr., N. Presser, and R. R. Horn, *AIAA J. Propulsion Power* **9**, 714 (1993).

⁵M. MacIver and M. E. Fajardo, *Mater. Res. Soc. Symp. Proc.* **285**, 105 (1993).

⁶D. B. Geohegan and D. N. Mashburn, *Appl. Phys. Lett.* **55**, 2345 (1989).

⁷M. J. Shea, R. N. Compton, and R. L. Hottel, *Phys. Rev. A* **42**, 3579 (1990).

⁸R. D. Hudson and L. J. Kieffer, *Atomic Data* **2**, 205 (1971).

⁹G. Koren, R. J. Beaman, A. Gupta, M. I. Lutwyche, and R. B. Laibowitz, *Appl. Phys. Lett.* **56**, 2144 (1990).

¹⁰P. A. Roland and J. J. Wynne, *J. Chem. Phys.* **99**, 8599 (1993).

¹¹J. F. Prichtenicht, *Rev. Sci. Instrum.* **45**, 51 (1974).

¹²H. Kang and J. L. Beauchamp, *J. Phys. Chem.* **89**, 3364 (1985).

¹³J. T. Knudsen, W. B. Gross, D. G. Sutton, *J. Appl. Phys.* **61**, 4771 (1987).

¹⁴H. Wang, A. P. Salberg, B. R. Weiner, *Appl. Phys. Lett.* **59**, 935 (1991).

¹⁵R. Kelly and R. W. Dreyfus, *Surf. Sci.* **198**, 263 (1988).

¹⁶M. MacIver and M. E. Fajardo (unpublished).

APPENDIX C

Velocity selection of fast laser ablated aluminum atoms by temporally and spatially specific photoionization

Michel Macler^{a)} and Mario E. Fajardo
Propulsion Directorate/RKFE, Phillips Laboratory, Edwards AFB, California 93524-7680

(Received 31 May 1994; accepted for publication 23 August 1994)

The successful demonstration of velocity selection of fast aluminum atoms by a novel, nonmechanical technique is reported. Pulses of atoms with broad velocity distributions are produced by laser ablation of aluminum metal. A second pulsed laser, delayed by $\sim 1 \mu\text{s}$ and crossed at a right angle to the atomic beam, is used to photoionize only those atoms with unwanted velocities, i.e., atoms moving too fast or too slow to be hidden behind an opaque mask placed $\sim 1 \text{ cm}$ from the ablated surface. The photoions are subsequently deflected from the beam by a static magnetic field. Velocity selected Al atom fluxes equivalent to $\Phi \sim 10^{11} \text{ atoms}/(\text{cm}^2 \text{ eV pulse})$ at a working distance of 10 cm are demonstrated. © 1994 American Institute of Physics.

Our research has recently focused on the mechanisms of vapor deposition of impurity atom doped cryogenic van der Waals solids.^{1,2} We have conjectured that the incident kinetic energies (KEs) of the codeposited impurity metal atoms is a key factor influencing the reactive and nonreactive microscopic dynamics of these processes. Resolution of these issues would be facilitated by the availability of a compact source for producing an intense, directed beam of nearly monoenergetic metal atoms with KEs tunable throughout the chemically important $1\text{--}20 \text{ eV}$ range. Unfortunately, existing sources³ based on neutralized ion beams are of limited utility due to low space-charge limited fluxes at the lower KEs.^{4,5} An alternative compact ion acceleration/neutralization scheme⁶ cannot be used in corrosive environments (e.g., B or Al vapor) due to materials incompatibilities. Also, for the lightest atoms of interest (e.g., Li, B), KEs $> 10 \text{ eV}$ require atomic velocities well over 10^6 cm/s —above the capabilities of compact mechanical velocity selectors.^{7–9}

However, laser ablation of metals provides a copious source of neutral and ionic, atomic and molecular metallic species with broad kinetic-energy distributions (KEDs) overlapping the desired range.^{10,11} We recently reported on measurements of KEDs of laser ablated Al atoms made close to ($x=0.5 \text{ cm}$) and far from ($x=22.5 \text{ cm}$) the ablated metal surfaces.¹² The good agreement between these measurements demonstrates the existence of a strong one-to-one correlation between atomic velocity and distance traveled from the surface on the $\sim 1 \mu\text{s}$ time scale of the short-range measurement. In this letter, we describe experiments which take advantage of this spatial separation of the various velocity components within the ablated plume to provide the proof-of-concept demonstration of a novel, velocity selected, laser ablation based metal-atom source.

Figure 1 shows a schematic diagram of the experiment. The ablation source region configuration is described in greater detail in Ref. 12. Briefly, the ablated plumes are generated by a focused ablation laser ($\lambda=308 \text{ nm}$, incident in-

tensities I_{abl} of $4 \times 10^7\text{--}1.1 \times 10^8 \text{ W/cm}^2$); the plume products pass through a magnetic-field region ($|B|=2.8 \text{ kG}$) which deflects and rejects the ionic species (e.g., Al^+ ions with $\text{KE} \leq 30 \text{ eV}$); the undeflected neutrals pass through a 0.2 cm diameter aperture at $x=6.0 \text{ cm}$ from the ablated surface.

We characterize the resulting neutral beam with a commercially available electrostatic energy analyzer/time-of-flight mass spectrometer (EEA/TOFMS) system¹³ employing pulsed laser photoionization (PI) of neutrals. We use an ArF excimer laser for the PI step, since the output at $\lambda=193 \text{ nm}$ is coincident with an extremely strong ($\sigma=2 \times 10^{-16} \text{ cm}^2$) Al atom autoionization resonance.¹⁴ Easily attainable PI laser fluences of $F_{\text{PI}}=15 \text{ mJ/cm}^2$ result in calculated and observed Al atom PI efficiencies of over 95%. The photoions of the proper KE that transit the EEA are accelerated to 2.0 keV , pass through the 1 m TOF tube, and are detected by a low gain ($\times 10^3$) microchannel-plate (MCP) detector. By scanning the delay between the ablation and PI lasers, and integrating the MCP signals over the range of arrival times cor-

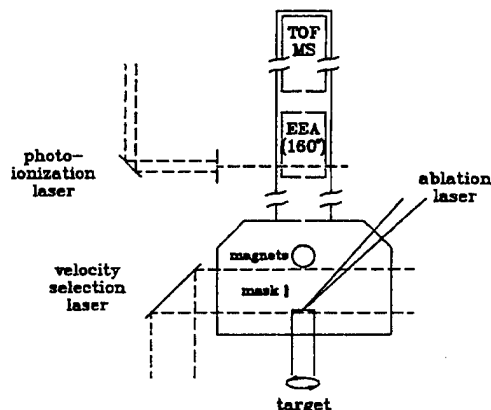


FIG. 1. Experimental diagram.

^{a)}National Research Council Postdoctoral Research Associate.

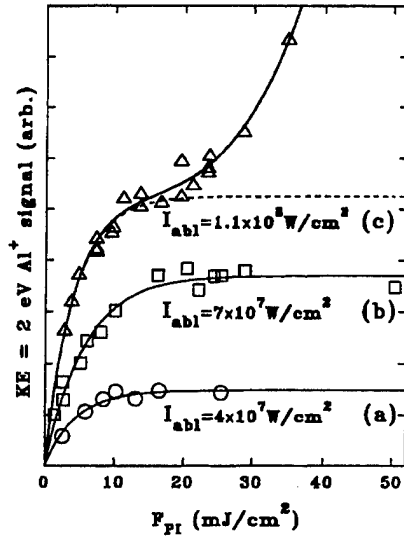


FIG. 2. Photoionization laser fluence dependence of KE=2 eV Al⁺ signal at various ablation laser intensities.

responding to Al⁺ ions, we obtain the TOF distributions of the Al atom precursor species arriving at the PI region which can produce Al⁺ photoions with a given KE.

At low ablation intensities, i.e., $I_{abl} \leq 7 \times 10^7 \text{ W/cm}^2$, the Al atom precursor TOF distributions peak at the correct arrival times for ablated Al atoms, and show a width corresponding to the energy resolution of the EEA (e.g., for KE=2 eV, $\Delta KE = 0.27 \text{ eV}$, $x_{PI} = 22.5 \text{ cm}$, $t_{peak} = 60 \mu\text{s}$, $\Delta t = 4 \mu\text{s}$.) However, at higher ablation and PI laser intensities, and only for Al⁺ photoion KEs below 4 eV, we observe a gross broadening of these TOF distributions measured at the PI region. For example, with $I_{abl} = 1.1 \times 10^8 \text{ W/cm}^2$ and $F_{PI} = 30 \text{ mJ/cm}^2$, 2 eV Al⁺ photoions are produced from species arriving at the PI region at delays from 50 to 80 μs after the ablation laser pulse. Scanning electron micrographs of aluminum films deposited using this source show a dramatic increase in the number of 100 nm–10 μm diameter aluminum particles as the ablation laser intensity is increased to $I_{abl} \geq 7 \times 10^7 \text{ W/cm}^2$. We suggest that the non-Al atom Al⁺ photoion precursors observed in the present experiments are in fact aluminum clusters and/or particles that are photofragmented and photoionized in the PI region to produce low KE Al⁺ ions.

Figure 2 shows the dependence of the KE=2 eV Al⁺ signal on the fluence of the PI laser, for three different ablation laser intensities. The ordinate of each point is calculated by integrating the complete TOF distributions of the Al⁺ photoion precursors. Figures 2(a) and 2(b) show the low ablation laser intensity data; the solid curves are least-squares fits to the simple first-order saturation equation:

$$S = \alpha[1 - \exp(-\beta F_{PI})]. \quad (1)$$

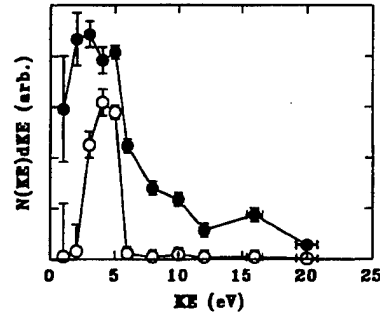


FIG. 3. Velocity selection using a thick wire mask placed close to the ablation target surface. The closed circles show the nascent Al atom KED; the open circles show the result of the VS laser. The experimental conditions were $I_{abl} = 7 \times 10^7 \text{ W/cm}^2$, $F_{VS} = 15 \text{ mJ/cm}^2$, $\Delta x = 0.16 \text{ cm}$, $x = 0.45 \text{ cm}$, $t_{VS} = 0.94 \mu\text{s}$. The error bars represent the estimated $\pm 1 \sigma$ limits.

Figure 2(c) shows data obtained for $I_{abl} = 1.1 \times 10^8 \text{ W/cm}^2$; in this case the solid curve fit includes an additional term representing a nonlinear, multiphoton process:

$$S = \alpha[1 - \exp(-\beta F_{PI})] + \gamma(F_{PI})^4. \quad (2)$$

The PI cross section extracted from the fitted β constant (using the measured ArF pulse full width at half maximum of 25 ns) is $\sigma_{PI} = 1.8(\pm 0.4) \times 10^{-16} \text{ cm}^2$, in good agreement with the previously mentioned Al atom literature value.¹⁴ These results support our assertion that restricting the ablation source operation to $I_{abl} \leq 7 \times 10^7 \text{ W/cm}^2$ yields a beam composed primarily of fast Al atoms.

We accomplish velocity selection (VS) of the Al atoms by temporally and spatially specific photoionization (TASSPI) of the unwanted velocity components using a third excimer laser (ArF), labeled "velocity selection laser" in Fig. 1, and rejection of the resulting Al⁺ ions by the magnetic deflection field. We use a simple opaque mask consisting of a metal wire of thickness Δx centered at a distance x from the ablation target surface, and offset about 1 cm from the atomic beam axis. The mask serves to protect the Al atoms hidden behind it at the arrival time of the VS laser pulse t_{VS} followed the ablation pulse. The surviving Al atoms have a spread of velocities Δv (full width at half-maximum), centered around a mean velocity v , and a corresponding spread of kinetic energies ΔKE , all related by:

$$\frac{\Delta KE}{KE} \sim 2 \frac{\Delta v}{v} \sim 2 \left[\left(\frac{\Delta x}{x} \right)^2 + \left(\frac{\Delta t_{VS}}{t_{VS}} \right)^2 \right]^{1/2}, \quad (3)$$

in which Δt_{VS} is taken as the sum of the duration of the VS laser pulse and the jitter between the ablation and VS pulses ($\Delta t_{VS} \sim 50 \text{ ns}$).

Figure 3 shows the results of our first attempt at VS by TASSPI in which we used a rather thick wire mask placed close to the ablation target surface. The KED of the transmitted Al atoms has a peak near 4 eV, and a width of $\Delta KE \sim 3 \text{ eV}$, as predicted by Eq. (3). These data also demonstrate good peak transmission $T_{Al}(KE)$ of the selected Al

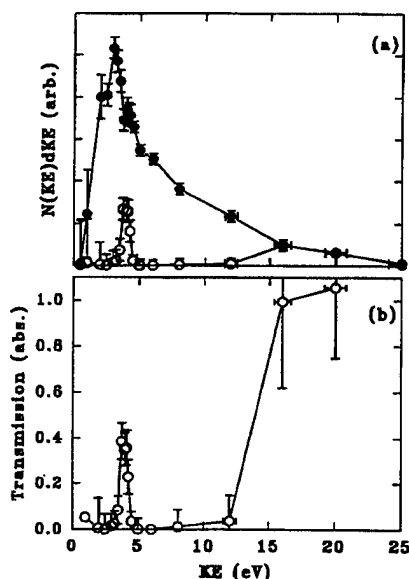


FIG. 4. Velocity selection using a thinner wire mask placed near the middle of the velocity selection port window. In (a) the closed circles show the nascent Al atom KED, the open circles show the result of the VS laser. The experimental conditions were $I_{abl}=7\times 10^7$ W/cm², $F_{VS}=15$ mJ/cm², $\Delta x=0.064$ cm, $x=0.90$ cm, and $t_{VS}=1.70$ μ s. (b) shows the transmission function of the velocity selection process for these conditions. The error bars represent the estimated ± 1 σ limits.

atoms [$T_{Al}(4\text{ eV})\sim 80\%$] as well as strong rejection of the unwanted velocity components throughout the rest of the 1–20 eV range.

Figure 4 shows a subsequent attempt to produce a beam with a narrower KED by placing a thinner wire mask farther away from the ablated target surface. Indeed, the KED of the transmitted Al atoms, again peaked at 4 eV, has sharpened to $\Delta KE=0.65$ eV. The data also show one of the limitations of our experimental setup: Attempts to produce narrow KEDs by placing the mask too far from the target surface can be accompanied by an increase in the transmission of the fastest Al atoms. This is due to the relatively short overall length of our VS region, only 2 cm, so that metal atoms with velocities in excess of $v\sim(2\text{ cm})/t_{VS}$ escape the effects of the VS laser and continue through the magnetic field and beam defining aperture. This puts an upper limit on the range of useful delays between ablation and VS laser pulses; i.e., ensuring that Al atoms with KEs up to ~ 30 eV are rejected in our apparatus requires maintaining $t_{VS}\leq 1.4$ μ s. Thus tuning of the desired KE of the transmission peak can be accomplished either by scanning t_{VS} , within the allowable limits, or by mechanically moving the opaque mask to change x .

We performed a series of Al film deposition rate measurements using a quartz-crystal microbalance (QCM) in an attempt to estimate the order of magnitude of the absolute fluxes of the velocity selected Al atoms. First, we removed the deflection magnets and beam defining aperture, and

placed the QCM at a working distance of $x=8.0$ cm from the ablation target. Assuming the formation of a bulk Al deposit, and a KE independent Al sticking coefficient of unity, we estimate a total incident Al flux of $\Phi(I_{abl}=7\times 10^7\text{ W/cm}^2, x=8\text{ cm})\sim 1.2\times 10^{12}$ atoms/(cm² pulse). The ratio of the Al deposition rates obtained with this geometry at $I_{abl}=7\times 10^7$ – 5×10^7 W/cm² was $R\sim 1.8$, in fair agreement with the corresponding ratio of total Al atom fluxes previously measured using the EEA/TOFMS system (i.e., $R\sim 1.6$; see Ref. 12, Fig. 3). Second, we replaced the deflection magnets and beam defining aperture, moved the QCM back to a working distance of $x'=18.0$ cm, and confirmed that the Al deposition rates scaled roughly as $(x/x')^2$, e.g., $\Phi(I_{abl}=7\times 10^7\text{ W/cm}^2, x=18\text{ cm, no VS})\sim 2.1\times 10^{11}$ atoms/(cm² pulse). Finally, we measured the Al deposition rates at $x=18$ cm, while employing VS by TASSPI under conditions similar to those used in the original experiment depicted in Fig. 3, and obtained $\Phi(I_{abl}=7\times 10^7\text{ W/cm}^2, x=18\text{ cm, } \Delta KE\sim 3\text{ eV})\sim 1.2\times 10^{11}$ atoms/(cm² pulse). The ratio of selected to unselected deposition rates at $x=18$ cm is $R\sim 0.5$, about twice the ratio of selected to unselected total Al atoms fluxes in the KEDs shown in Fig. 3, an appropriate reminder of the rough nature of these comparisons. From these measurements, we estimate that this source delivers velocity selected Al atom fluxes of $\Phi\sim 10^{11}$ atoms/(cm² eV pulse) at a working distance of 10 cm.

We have also demonstrated VS of Al atoms to produce KEDs peaked at 2 and 8 eV, and are still in the process of optimizing the source operating parameters. We have produced Al atom KEDs peaked at 2 eV with widths as narrow as $\Delta KE\sim 0.2$ eV [with $x=1.1$ cm, $\Delta x=0.06$ cm, $t_{VS}=2.9$ μ s, $T(KE=2\text{ eV})=50\%$, $T(KE>6\text{ eV})=100\%$]. We have noticed that the magnitude of the transmission function maximum decreases as we use progressively thinner wire masks, indicating that diffraction of the VS laser beam by the mask is significant in our current setup. We hope to overcome this problem by adopting laser lithographic techniques and imaging the mask onto the atomic beam axis.

Our plans for the immediate future include attempts at VS of laser ablated Ga and In atoms, which also have large PI cross sections at 193 nm.¹⁴

¹M. E. Fajardo, J. Chem. Phys. **98**, 110 (1993).

²S. Tam and M. E. Fajardo, J. Chem. Phys. **99**, 854 (1993).

³Atomic and Molecular Beam Methods, edited by G. Scoles, D. Bassi, U. Buck, and D. Laine (Oxford, New York, 1988), Vol. 1.

⁴M. Hollstein and H. Pauly, Z. Phys. **196**, 353 (1966).

⁵S. Kita, H. Hubner, W. Kracht, and R. Duren, Rev. Sci. Instrum. **52**, 684 (1981).

⁶R. K. B. Helbing and E. W. Rothe, Rev. Sci. Instrum. **39**, 1948 (1968).

⁷H. U. Hostettler and R. B. Bernstein, Rev. Sci. Instrum. **31**, 872 (1960).

⁸L. T. Crowley, M. A. D. Fluendy, and K. P. Lawley, Rev. Sci. Instrum. **41**, 666 (1970).

⁹G. O. Este, B. Hilko, D. Sawyer, and G. Scoles, Rev. Sci. Instrum. **46**, 223 (1975).

¹⁰J. F. Fritchenicht, Rev. Sci. Instrum. **45**, 51 (1974).

¹¹H. Kang and J. L. Beauchamp, J. Phys. Chem. **89**, 3364 (1985).

¹²M. MacIer and M. E. Fajardo, Appl. Phys. Lett. **65**, 159 (1994).

¹³M. J. Shea, R. N. Compton, and R. L. Hettich, Phys. Rev. A **42**, 3579 (1990).

¹⁴R. D. Hudson and L. J. Kieffer, At. Data **2**, 205 (1971).

APPENDIX D

VELOCITY SELECTION OF LASER ABLATED METAL ATOMS BY A NOVEL NON-MECHANICAL TECHNIQUE

MARIO E. FAJARDO AND MICHEL MACLER*

Emerging Technologies Branch, Propulsion Directorate, Phillips Laboratory,
OLAC PL/RKFE, 10 E. Saturn Blvd., Edwards Air Force Base, CA 93524-7680.

*AFMC PL/NRC Post-doctoral Research Associate.

ABSTRACT

We present the results of experiments on velocity selection of fast laser ablated Al, Ga, and In atoms by a novel, non-mechanical, technique. Pulses of atoms with broad velocity distributions are produced by laser ablation of a single component pure metal target in vacuum. After a delay of $\sim 1 \mu\text{s}$, there exists a strong one-to-one correlation between atomic velocity and distance traveled from the ablated surface. Thus, a second pulsed laser, delayed by $\sim 1 \mu\text{s}$ and crossed at a right angle to the atomic beam, can be used to photoionize only those atoms with unwanted velocities, *i.e.*: atoms moving too fast or too slow to be hidden behind an opaque mask placed $\sim 1 \text{ cm}$ from the ablated surface. The photoions, and any ions surviving from the ablation event, are subsequently deflected from the beam by a static magnetic field. By a fortunate coincidence, Al, Ga, and In atoms all have very large single photon photoionization cross sections at 193 nm, the output wavelength of the ArF excimer laser; thus, well over 95% of the unwanted atoms can be easily photoionized and rejected. We have demonstrated velocity selected Al, Ga, and In atom fluxes equivalent to $\Phi \sim 10^{11} \text{ atoms}/(\text{cm}^2\text{-eV-pulse})$ at a working distance of 10 cm.

INTRODUCTION

Pulsed laser ablation of solid targets is an increasingly popular technique for the deposition of a wide variety of thin film materials [1]. There are many fundamental and applied studies underway of *e.g.*: laser/surface interactions, plume plasma hydrodynamics, plume composition *vis-à-vis* ions/neutrals/clusters/particulates, internal and kinetic energy content of ablated species, *etc.*, and of how all these factors ultimately affect the processes of thin film deposition and growth. Unfortunately, progress towards this ultimate goal is hampered by the bewildering complexity of the phenomena involved, a predicament that has been likened to studying "a tornado in a garbage can." We believe that any modification of "standard" laser ablation techniques which result in a simplification of this situation, and/or in improved parametric control over deposition conditions, will prove to be highly valuable to the thin film deposition community.

As a case in point: we have been employing pulsed laser ablation of metal targets as a source of metal atoms for matrix isolation spectroscopy (MIS) studies for several years now [2-6]. We prepare our MIS samples by codepositing the products of a laser ablated plume along with a large excess of an inert matrix host gas onto a cryogenically

cooled substrate. These experiments have lead us to hypothesize that the incident kinetic energy (KE) of the ablated metal atoms plays a key role in determining the atomic isolation efficiency of the matrix deposition process, and in the formation of novel metal atom trapping site structures.

However, this hypothesis is largely speculation, as we have not measured *in situ* (in our MIS apparatus) the actual composition of these laser ablated plumes, or the kinetic energy distributions (KEDs) of the ablated atoms. Furthermore, the laser ablation process can produce a mixture of metal atoms, clusters, and ions with rather broad KEDs, in some cases with KEs tailing out to several tens of electron volts. Thus, we undertook an effort to better characterize the chemical identity and KEDs of the laser ablated species produced under our experimental conditions, and to find out if we could gain improved control over these properties [7,8]. This effort culminated last year in our demonstration of velocity selection of fast laser ablated Al atoms by Temporally And Spatially Specific Photoionization (TASSPI) [9]; a novel, non-mechanical technique which provides a clean, stable, compact, intense, and tunable source of fast monoenergetic metal atoms for MIS experiments in particular, and thin film depositions in general.

In this manuscript, we briefly describe the TASSPI technique, and present the highlights of our recent results on velocity selection of Ga and In atoms; the interested reader is directed to ref. 9 for details of our Al atom work. A more detailed presentation of all our TASSPI related work is currently in preparation [10].

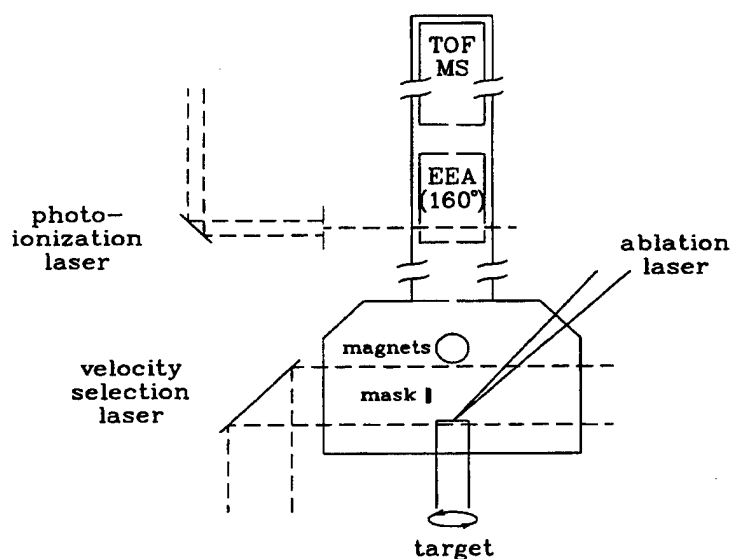


Fig. 1: TASSPI Experimental Diagram.

EXPERIMENTAL

Fig. 1 shows a schematic of our experimental setup, as configured for velocity selection by TASSPI. The metal ablation targets are mounted on a rotatable rod within a vacuum chamber pumped directly by a small turbomolecular pump to $\sim 10^{-6}$ Torr. The ablated plumes are generated by an excimer laser beam (XeCl, $\lambda=308$ nm) incident at an angle of 45° from the surface normal, and focused to a ≈ 0.003 cm² spot so as to cut a circular track on the rotating target. The laser ablated plume products pass through a magnetic field region ($|B| = 2.8$ kG), located 2.5 cm from the ablation target surface, which deflects ionic species (e.g.: Ga⁺ and In⁺ ions with KE ≤ 15 eV) from the atomic beam axis. The beam axis is defined by the ablation spot on the target and a 0.2 cm diameter isolation aperture located ≈ 6 cm from the target surface, from which we estimate the final beam divergence as ≈ 40 mrad.

We characterize the chemical composition and KEDs of the species emerging through the isolation aperture with an electrostatic energy analyzer/time-of-flight mass spectrometer (EEA/TOFMS) system, using pulsed photoionization (ArF, $\lambda=193$ nm) of neutrals [8,9]. As we have discussed before [8,9], the apparent redundancy of this detection scheme (which requires that the time of flight of neutrals from the ablation target surface to the photoionization region be appropriate to the photoion pass energy selected by the EEA) allows us to detect the presence of non-atomic M⁺ ion precursors in the atomic beam. The photoions which transit the EEA are accelerated to 2.0 keV, separated by mass in a 1 m TOF tube, and detected by a low gain microchannel plate detector.

Velocity selection by TASSPI entails photoionizing those metal atoms with unwanted velocities using another ArF excimer laser ("velocity selection laser" in fig. 1) and rejection of the resulting photoions by the magnetic deflection field. We have previously reported measurements of Al atom KEDs made close to and far from the ablated target surface which demonstrate that, under our mild ablation conditions, the Al atom KEDs are established on a sub 100 ns timescale [7,8]. Thus, after a delay of ~ 1 μ s, there exists a strong one-to-one correlation between atomic velocity and distance traveled from the ablated surface (*i.e.* the atoms have sorted themselves out with the faster atoms traveling farther from the surface). A simple opaque mask of width Δx , placed at a distance x from the target surface, serves to protect those metal atoms hidden behind it at the arrival time of the velocity selection laser (t_{VS}). These metal atoms, with mean velocity $v = x/t_{VS}$, will not be photoionized, and hence will not be deflected from the atomic beam by the magnetic rejection field. The mean velocity can thus be set by adjusting x , and/or by adjusting t_{VS} , within limits set by the requirement that the fastest metal atoms to be rejected still be in the velocity selection region at t_{VS} . The surviving metal atoms have a spread of velocities, Δv (full width at half maximum, FWHM), and a corresponding spread of kinetic energies, ΔKE , all related by:

$$\frac{\Delta KE}{KE} \approx 2 \frac{\Delta v}{v} \approx 2 \left[\left(\frac{\Delta x}{x} \right)^2 + \left(\frac{\Delta t_{VS}}{t_{VS}} \right)^2 \right]^{1/2}$$

in which Δt_{VS} is taken as the sum of the duration of the velocity selection laser pulse and the jitter between the ablation and velocity selection pulses ($\Delta t_{VS} \approx 50$ to 100 ns).

RESULTS AND DISCUSSION

We have previously shown in our Al experiments that maintaining the ablation laser intensity (I_{abl}) below $\approx 1 \times 10^8$ W/cm² greatly reduces the number of metal clusters and particles formed in the ablation process [8,9]. For Ga and In targets, we achieved the same results by keeping I_{abl} below $\approx 4 \times 10^7$ W/cm².

By varying the fluence of the ArF photoionization laser up to about 500 mJ/cm² we were able to saturate the intensities of both Ga⁺ and In⁺ signals. By fitting these saturation curves we can estimate the atomic photoionization cross sections at 193 nm as $\sigma_{PI}(Ga) = 2.7(\pm 0.6) \times 10^{-17}$ cm² and $\sigma_{PI}(In) = 1.7(\pm 0.6) \times 10^{-17}$ cm², in good agreement with previously published values [11]. These measurements confirm the velocity selection laser fluences, F_{VS} , required for efficient implementation of the TASSPI process.

Fig. 2 shows the results of a velocity selection experiment on laser ablated Ga

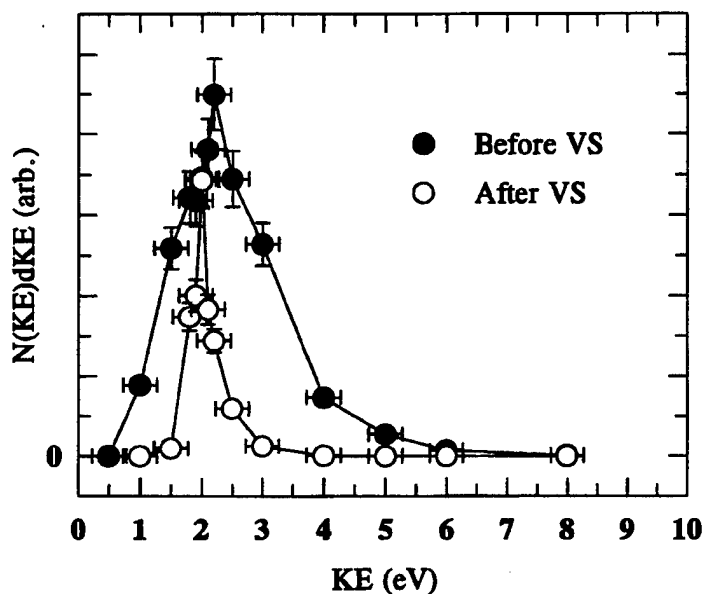


Fig. 2: Velocity Selection of Ga Atoms by TASSPI. The closed circles show the nascent Ga atom KED, the open circles show the TASSPI effect. The error bars represent the estimated $\pm 1 \sigma$ limits. The experimental conditions were: $I_{abl} = 3.4 \times 10^7$ W/cm², $F_{VS} = 500$ mJ/cm², $x = 0.90$ cm, $\Delta x = 0.16$ cm, $t_{VS} = 3.8$ μ s.

atoms. The nascent Ga atom KED peaks near 2.2 eV and shows a FWHM of ≈ 1.8 eV. The velocity selected Ga atom KED peaks at 2.0 eV with a FWHM of 0.5 eV. The transmission of the velocity selector at the 2 eV peak is very nearly 100%, and the integrated transmission is ≈ 20 % of the original laser ablated flux. Quartz crystal microbalance (QCM) measurements indicate a velocity selected Ga atom flux of $\Phi_{\text{Ga}} \approx 8 \times 10^{10}$ atoms/(cm² eV pulse) at a distance of 10 cm from the ablation target surface.

Fig. 3 shows the results of a velocity selection experiment on laser ablated In atoms. The nascent KED peaks near 2.8 eV and shows a FWHM of ≈ 2.4 eV. The velocity selected KED peaks near 3 eV with a FWHM of 0.9 eV. The transmission at the 3 eV peak is very nearly 100%, and the integrated transmission is ≈ 20 % of the original atomic flux. QCM measurements yield a velocity selected In atom flux of $\Phi_{\text{In}} \approx 6 \times 10^{10}$ atoms/(cm² eV pulse) at a working distance of 10 cm.

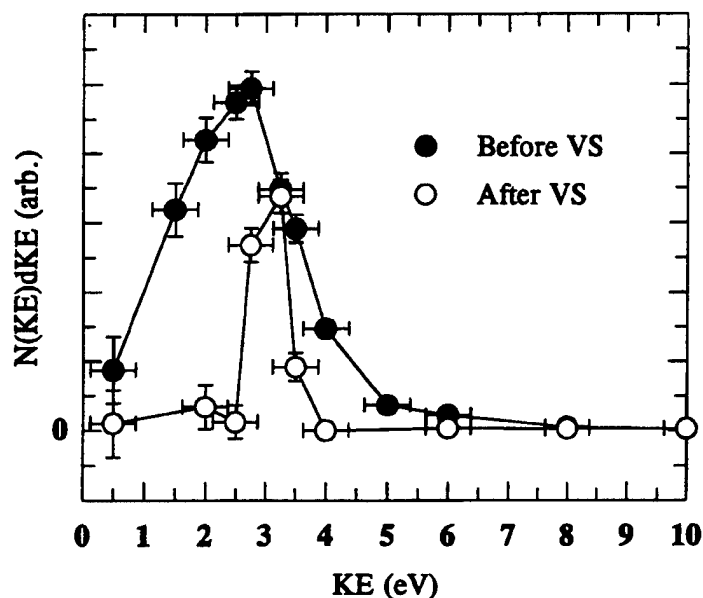


Fig. 3: Velocity Selection of In Atoms by TASSPI. The closed circles show the nascent In atom KED, the open circles show the TASSPI effect. The error bars represent the estimated $\pm 1 \sigma$ limits. The experimental conditions were: $I_{\text{abl}} = 3.4 \times 10^7$ W/cm², $F_{\text{VS}} = 530$ mJ/cm², $x = 0.90$ cm, $\Delta x = 0.16$ cm, $t_{\text{VS}} = 4.0$ μ s.

CONCLUSIONS AND FUTURE DIRECTIONS

We have demonstrated a new, non-mechanical technique for performing velocity selection of fast laser ablated Al, Ga, and In atoms. Actually, the relatively low velocities of the heavy Ga and In atoms allow the use of conventional velocity selection schemes, but we found switching between group IIIB metals very convenient with the TASSPI method.

We are currently pursuing velocity selection of lighter species such as fast Li and B atoms. Unfortunately, the single photon photoionization cross section for Li is smaller than that for Al by over two-orders of magnitude [11], and the ionization potential for B atoms is almost 6.7 eV [12], corresponding to a presently inconvenient photon wavelength of 185 nm. It may be that the implementation of TASSPI in these systems will require the use of multi-photon ionization techniques, perhaps involving tunable pulsed lasers able to effect resonance enhancement via intermediate states [12].

We hope to ultimately apply a TASSPI source to help answer some of the questions arising from our MIS work mentioned above. We will begin with co-depositions of fast Al atoms and molecular hydrogen at 2 K, examining the KE dependence of the atomic isolation efficiency and the formation of Al_xH_y reaction products [6].

We also hope that the TASSPI technique will find its way into other thin film deposition experiments, at least as a research tool. Three simultaneous modifications: increasing the ablation laser spot size while maintaining I_{ab} constant, increasing the diameter of the beam defining aperture, and increasing the magnetic rejection field strength, should allow for pure atomic fluxes of over 10^{12} atoms/(cm² eV pulse) at a 10 cm working distance. Excimer lasers operating at ~ 1 KHz repetition rates would then provide ~ 10^{15} atoms/(cm² eV s). Ultimately, TASSPI may help elucidate the roles of incident atomic KE, beam composition, *etc.* in the formation of mixed semiconductors, nonlinear optical materials, and other thin films produced by laser ablation techniques.

REFERENCES

1. Laser Ablation in Materials Processing: Fundamentals and Applications, B. Braren, J.J. Dubowski, and D.P. Norton, eds. (Mater. Res. Soc. Proc. 285, Boston, MA, 1993).
2. M.E. Fajardo, P.G. Carrick, J.W. Kenney III, J. Chem. Phys. **94**, 5812 (1991).
3. M.E. Fajardo, J. Chem. Phys. **98**, 110 (1993).
4. S. Tam and M.E. Fajardo, J. Chem. Phys. **99**, 854 (1993).
5. R.A. Corbin and M.E. Fajardo, J. Chem. Phys. **101**, 2678 (1994).
6. M.E. Fajardo, S. Tam, T.L. Thompson, and M.E. Cordonnier, Chem. Phys. **189**, 351 (1994).
7. M. MacIer and M.E. Fajardo, pp. 105-110 in ref. 1.
8. M. MacIer and M.E. Fajardo, Appl. Phys. Lett. **65**, 159 (1994).
9. M. MacIer and M.E. Fajardo, Appl. Phys. Lett. **65**, 2275 (1994).
10. M. MacIer and M.E. Fajardo, manuscript in preparation.
11. R.D. Hudson and L.J. Kieffer, Atomic Data **2**, 205 (1971).
12. V.S. Letokhov, Laser Photoionization Spectroscopy, (Academic, Orlando, FL 1987).

APPENDIX E

United States Patent [19]
Fajardo et al.

[11] **Patent Number:** 5,567,935
[45] **Date of Patent:** Oct. 22, 1996

[54] **VELOCITY SELECTED LASER ABLATION
METAL ATOM SOURCE**

[75] **Inventors:** Mario E. Fajardo; Michel Macler,
both of Lancaster, Calif.

[73] **Assignee:** The United States of America as
represented by the Secretary of the
Air Force, Washington, D.C.

5,019,705 5/1991 Compton 250/251
5,115,439 5/1992 Howard 372/37
5,268,921 12/1993 McLellan 372/87
5,295,009 3/1994 Bamik et al. 359/65

Primary Examiner—Jack I. Berman
Assistant Examiner—Kiet T. Nguyen
Attorney, Agent, or Firm—Robert L. Nathans

[57] **ABSTRACT**

A pulsed plume of laser ablated photo-ionizable material is emitted from a target in a vacuum, and a pulsed beam of light thereafter produces ionization of two plume sections straddling a central nonionized plume portion. A mask is provided, intermediate the plume and the laser generating the ionizing pulsed beam of light, to shield the central plume portion to prevent ionization thereof. The ionized portions of the plume are swept away from the vicinity of the non-ionized plume portion by a magnetic field, and the remaining nonionized portion passes through an aperture in a retrieval mask to produce the output of the atomic source.

[21] **Appl. No.:** 458,518

[22] **Filed:** Jun. 2, 1995

[51] **Int. Cl.⁶** H01J 3/04

[52] **U.S. Cl.** 250/251; 250/423 P

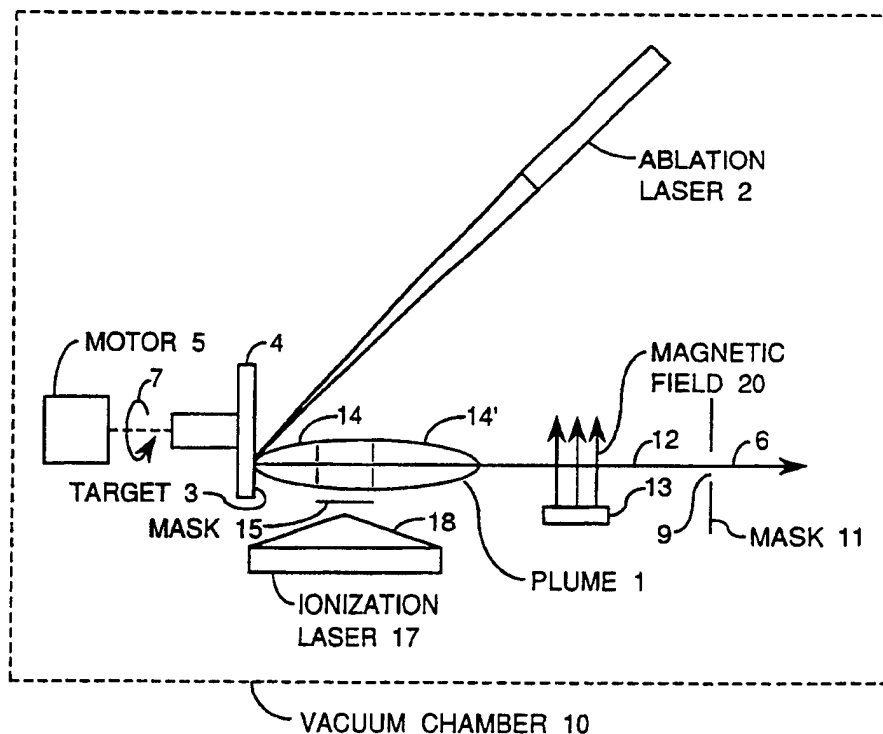
[58] **Field of Search** 250/251, 423 P,
250/288, 288 A

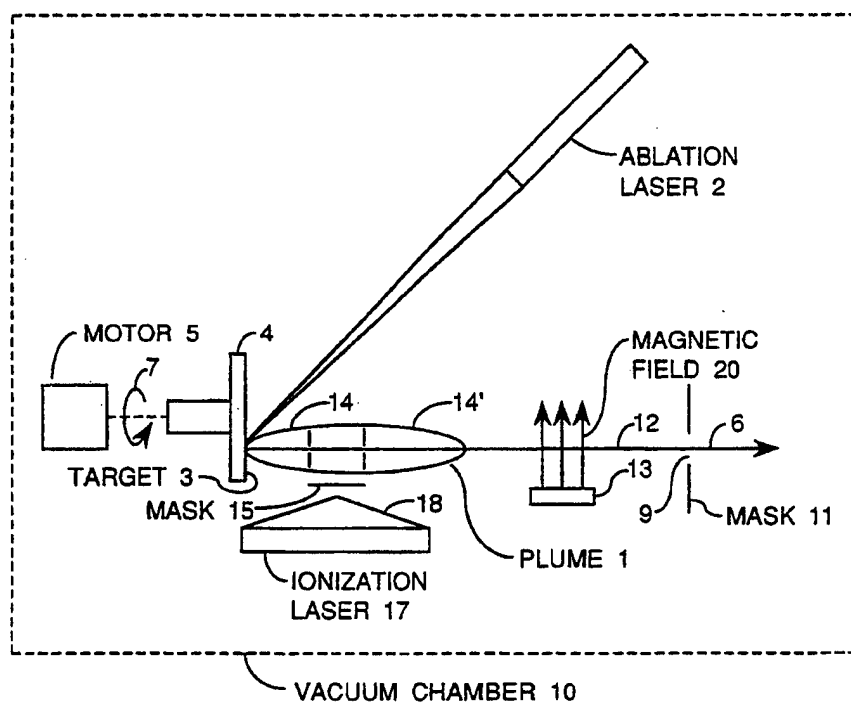
[56] **References Cited**

U.S. PATENT DOCUMENTS

4,105,921 8/1978 Bartlett et al. 250/423 P
4,740,692 4/1988 Yamamoto et al. 250/423 P

20 Claims, 1 Drawing Sheet





1

VELOCITY SELECTED LASER ABLATION METAL ATOM SOURCE

STATEMENT OF GOVERNMENT INTEREST

The invention described herein may be manufactured and used by or for the Government for governmental purposes without the payment of any royalty thereon.

BACKGROUND OF THE INVENTION

Traditional methods of producing beams of velocity selected neutral atomic or molecular species do not work well throughout the 1 to 20 eV kinetic energy range, for which atomic velocities can exceed one million cm/sec. Standard mechanical velocity selection techniques are limited to maximum transmitted velocities of about 100,000 cm/sec, or they require very long atomic flight distances of about 100 cm. Beams of nearly monoenergetic very fast neutral species can be produced routinely by charge exchange neutralization of a beam of suitable parent ions. However, this technique fails for kinetic energies below about 10 eV due to space charge limitations on the intensity of the parent ion beam.

The laser ablation into vacuum process provides a compact source of intense beams of neutral and ionic species throughout the desired kinetic energy range, but with very broad kinetic energy distributions.

SUMMARY OF A PREFERRED EMBODIMENT OF THE INVENTION

The present invention combines the best features of the laser ablation process with a non-mechanical velocity selection arrangement capable of operating in the desired kinetic energy range. Kinetic energy is of course proportional to the velocity squared. In accordance with a preferred embodiment of the invention, a target is positioned in a vacuum chamber, which target comprises a material which can be photo-ionized. A pulsed plume of ablated photo-ionizable particulate material, emerging from the target, is projected along a projection axis within the vacuum chamber, and a pulsed beam of light, capable of ionizing the plume, intersects selected portions of the plume to create two ionized portions, separated by a non-ionized portion therebetween. A magnetic field then sweeps the ionized plume portions away from the projection axis and the non-ionized portion is retrieved by an apertured mask having its aperture positioned on the projection axis.

BRIEF DESCRIPTION OF THE DRAWING

Other features of the invention will become apparent upon study of the following detailed description of preferred embodiments of the invention, taken in conjunction with the sole FIGURE schematically illustrating an embodiment of the invention.

DETAILED DESCRIPTION

In the sole FIGURE, and within vacuum chamber 10, a pulsed plume 1 of metal atoms, ions, molecules, clusters and metal particles can be produced by focussing the output of a pulsed ablation laser 2 upon the surface 4 of a rotating target 3 held in a vacuum chamber. The atomic beam 6, which is the output product of the atomic source, passes through an aperture 9 of retrieval mask 11 positioned upon the plume projection axis 12. Motor 5 produces rotation of target 3 as indicated by 7. Typically, the kinetic energies and

2

total flux of the constituents of the beam can be increased by increasing the incident fluence, (power/area), of the ablation laser 2.

For the purposes of the present invention, the metal ions, molecules, clusters, and particles are unwanted contaminants in the atomic beam and can be reduced by restricting the incident fluence of the ablation laser 2 to values within a few times the threshold for producing visible emissions from the plume, or by using very short picosecond ablation pulses; see F. Mueller et al., Proc. SPIE-Int. Soc. Opt. Eng. vol. 1858, pp. 464-475 (1993). This consideration requires the selection of a compromise value of the ablation laser fluence, with beam energy and flux being traded off for beam purity. The ions which survive the plume expansion are deflected upwardly by magnetic field 20, are swept away from projection axis 12, and thus fail to pass through aperture 9 of beam retrieval mask means 11.

Operating the beam source as described, provides a beam composed predominantly of metal atoms with kinetic energies in the 1-20 eV range, with however, a very broad distribution of kinetic energies which is reduced by our novel method of velocity selection. The method is based upon the spatial separation of the different velocity components of the plume following a short delay after the arrival of the ablation laser pulse, that is, the faster metal atoms move farther away from the metal target surface 4 than do the slow ones in the same amount of time. Thus, only those metal atoms having the proper velocities to be retrieved to form the output beam, are hidden behind opaque mask 15, and thus avoid being ionized when the pulse 18 from the ionization laser 17 intercepts the photo-ionizable plume 1. This action creates a pair of photo-ionized plume sections 14 and 14' to the right and left of the mask 15, which ionized plume sections are swept away from axis 12 by magnetic field 20, produced by magnetization means 13. The result of this action is that only those nonionized atoms behind the mask 15 will remain on the projection axis 12 to pass through aperture 9 of the retrieval mask 11 to be outputted from the device with the desired pass velocity. The peak of the velocity distribution of these unaffected nonionized atoms behind mask 15 is related to the distance d between the target surface 4 and the center of the mask, and the time delay between the production of the laser ablation pulse and the ionization laser pulse. The pass velocity will be equal to the distance d divided by this time delay. The width of the velocity distribution of the velocity selected metal atoms decreases as the mask is made narrower, down to a limit imposed by the finite duration of the ablation laser pulses and the initial plume formation process, and the finite duration of the ionization laser pulses together with diffraction limitations on imaging the masked ionization laser pulse onto the plume.

Some operating parameters of our first demonstration experiment were as follows: pulses from a xenon-chloride excimer ablation laser: pulse energy 10 milli-joule, 308 nm wavelength, were focused upon a high purity A1 target. The ablation laser beam was focused down to a spot of 0.05x0.10 cm and had a duration of 0.03 microseconds. The magnetic field had a magnetic field strength of 2.8 kilo-Gauss. Aperture 9 had a diameter of 0.2 cm, formed in a 0.05 cm thick steel sheet, placed 6 cm from the target surface. An ArF ionization laser was employed and the photoionization process was very efficient, such that about 98% of the unwanted aluminum atoms was readily ionized and rejected. Photoionization mask 15 consisted of a 0.15 cm wire placed 0.5 cm from the target surface and photoionization was accomplished by unfocused 100 mJ pulses of 0.25 microsecond

3

duration, delayed by 0.94 microseconds from the ablation laser pulse. These conditions resulted in a pass velocity of 500,000 cm/sec and a peak pass energy of 4 eV.

For additional examples of demonstrated operating conditions for Al atoms, see M. Macler and M. E. Fajardo, *Appl. Phys. Lett.*, vol. 65, pages 2275-2277, (31 Oct., 1994). For information concerning our recent demonstration of the temporally and spatially specific photoionization (TASSPI) effect for gallium and indium atoms, see M. E. Fajardo and M. Macler, *Material Research Society, Symposium Proceedings*, vol. 388, (1995).

Variations on the aforesaid components and parameters will occur to skilled workers in the art and thus the scope of the invention is to be restricted only by the terms of the following claims and art recognized equivalents thereof.

What is claimed is:

1. An atom source comprising:

- (a) a target of a material which can be photoionized, positioned within a vacuum chamber;
- (b) ablation means for projecting a pulsed plume of ablated photo-ionizable material from said target along a projection axis positioned within said vacuum chamber;
- (c) an ionization laser for directing a pulsed light beam capable of ionizing said plume of ablated ionizable material, toward said projection axis;
- (d) retrieval means positioned along said projection axis for retrieving only selected material particles from said plume;
- (e) light beam control means for causing only selected portions of said pulsed light beam generated by said ionization laser to intersect said plume to produce ionized plume portions; and
- (f) means for producing a magnetic field for sweeping said ionized plume portions away from said projection axis to prevent retrieval of said ionized plume portions by said retrieval means.

2. The source of claim 1 wherein said ablation means comprises an ablation laser.

3. The source of claim 2 wherein said beam control means comprises masking means for shielding a selected plume portion from the pulsed light beam generated by said ionization laser.

4. The source of claim 3 wherein said retrieval means comprises an apertured mask for permitting a nonionized plume portions to pass therethrough.

5. The source of claim 4 further including means for rotating said target during operation of said ablation means.

6. The source of claim 3 further including means for rotating said target during operation of said ablation means.

7. The source of claim 2 wherein said retrieval means comprises an apertured mask for permitting a nonionized plume portion to pass therethrough.

8. The source of claim 2 further including means for rotating said target during operation of said ablation means.

9. The source of claim 1 wherein said beam control means comprises masking means for shielding a selected plume portion from the pulsed light beam generated by said ionization laser.

10. The source of claim 9 wherein said retrieval means comprises an apertured mask for permitting a nonionized plume portion to pass therethrough.

4

11. The source of claim 9 further including means for rotating said target during operation of said ablation means.

12. The source of claim 1 wherein said retrieval means comprises an apertured mask for permitting a nonionized plume portion to pass therethrough.

13. Atomic source apparatus comprising:

- (a) a target of a material which can be ionized, positioned within a vacuum chamber;
- (b) means for directing a pulsed plume of ablated ionizable material from said target toward a first portion of said apparatus;
- (c) pulsed ionization means for ionizing selected portions of said plume to create ionized plume portions and a nonionized plume portion;
- (d) magnetizing means for causing a magnetic field to sweep said ionized plume portions away from said first portion of said apparatus; and
- (e) retrieval means, positioned at the first portion of said apparatus, for retrieving said nonionized plume portion.

14. The source of claim 13 further including means for rotating said target.

15. The source of claim 13 wherein said retrieval means comprises an apertured mask.

16. The source of claim 15 wherein said pulsed ionization means includes a mask for preventing ionization of a portion of said plume positioned between the selected portions of said plume being ionized.

17. The source of claim 13 wherein said pulsed ionization means includes a mask for preventing ionization of a portion of said plume positioned between said selected portions of said plume being ionized.

18. A method of generating an atomic beam comprising the steps of:

- (a) providing a target of a material which can be photoionized, positioned within a vacuum;
- (b) generating a pulsed plume of ablated ionizable material from said target and projecting said pulsed beam of ablated ionizable material along a projection axis positioned within said vacuum;
- (c) directing pulsed beams of light, capable of ionizing said plume of ablated ionizable material, through selected portions of said plume to create ionized plume portions;
- (d) causing a magnetic field to sweep said ionized plume portions away from said projection axis; and
- (e) retrieving a nonionized plume portion positioned along said projection axis.

19. A method of generating an atomic beam comprising the steps of:

- (a) ionizing portions of a plume of ionizable material to form ionized plume portions;
- (b) causing a magnetic field to drive said ionized plume portions in a direction away from a predetermined area; and
- (c) retrieving a nonionized plume portion within said predetermined area.

20. The method of claim 19 wherein the steps thereof are carried out in a vacuum.

* * * * *